Mini-channel heat exchangers for industrial distillation processes

Dennis Marijn van de BOR

Mini-channel heat exchangers for industrial distillation processes

Proefschrift

Ter verkrijging van de graad van doctor
aan de Technische Universiteit Delft
op gezag van de Rector Magnificus prof. Ir. K.C.A.M. Luyben
voorzitter van het College voor Promoties,
in het openbaar te verdedigen op 03 maart 2014 om 10:00 uur

door

Dennis Marijn van de BOR

Ingenieur Mechanical Engineering

Geboren te Den Helder, Nederland

Dit proefschrift is goedgekeurd door de promotor:

Prof. Dr. Ir. T.J.H. Vlugt

Copromotor:

Dr. Ir. C.A. Infante Ferreira

Samenstelling promotiecommissie

Rector Magnificus,	Voorzitter
Prof. Dr. Ir. T.J.H. Vlugt	Technische Universiteit Delft, promotor
Dr. Ir. C.A. Infante Ferreira	Technische Universiteit Delft, co-promotor
Prof. Dr. Piero Colonna	Technische Universiteit Delft
Prof. Dr. Ir. J. Westerweel	Technische Universiteit Delft
Prof. Dr. J. Fernandez-Seara	Universidade de Vigo
Prof. Dr. A. Coronas	Universitat Rovira I Virgili, Tarragona
Dr. Ir. A. A. Kiss	AkzoNobel - Research, Development & Innovation, Deventer

Cover design by D.M. van de Bor

CONTENTS

1 INTRODUCTION

Heat pumps are systems which can add heat to a given process in an efficient manner. Where a conventional heating system converts chemical energy into hot gases before heating the process generating the full amount of heat, heat pumps are able to upgrade the heat coming from such processes to the desired temperatures only using a fraction of the energy conventional heating systems would require.

Since the efficiency of a heat pump is largely dependent on the difference between the temperature of the source of the heat and the desired process temperature, finding a source with an already high temperature is important. A source can be the ground, surrounding air, solar energy, the sewer, but each one of them has its drawbacks: for instance, low temperature, or uncertain availability. In process separations like distillation, another heat source is available continuously at relatively high temperature and in large amounts: waste heat. These processes also require heat in large amounts, at a slightly higher temperature level and therefore are a good candidate for the application of heat pumps.

In distillation, two or more components are separated based on their difference in boiling point. A mixture is boiled up in the (re)boiler of a column, stripping off most of the light component and a part of the heavy component. The remaining flow leaves the column as product stream. The vapor created is relatively rich in low boiling component and moves toward the condenser in the top of the column. Here the overhead vapors are condensed and leave the system as product, or flow back into the column as reflux. In between the reboiler and condenser there are a few to many trays to increase the separation efficiency. Again starting at the reboiler the vapor moves up each tray, loses some of the heavier component, therefore becoming richer in the light component. The liquid flowing downward becomes richer in the heavy component. The temperature gradually decreases from the bottom of the column to the top of the column. For further background information on distillation, see refs. [16, 32, 38, 92].

The theoretical efficiency (Carnot COP) of a heat pump is defined by temperature lift, which is the difference in temperature between the heat source and the heat sink, and the absolute temperature of either source or sink. Since the efficiency of heat pumps decreases at higher temperature lifts, heat pumps become less feasible at high lifts. The efficiency can be increased by reducing temperature driving forces, increasing compressor efficiency or reducing throttling losses. Alternatively, one might look into a solution which can make use of the temperature glide (temperature difference between in- and outlet) available in many process installations. The average temperature lift of the heat pump is reduced by benefitting from such a temperature glide, increasing the efficiency of the system. Making use of such a glide requires a multi-component working fluid. This is exactly what a compression-resorption heat pump does: the ammonia-water mixture used in such a heat pump allows for a temperature glide in both heat exchangers of the heat pump.

a

b
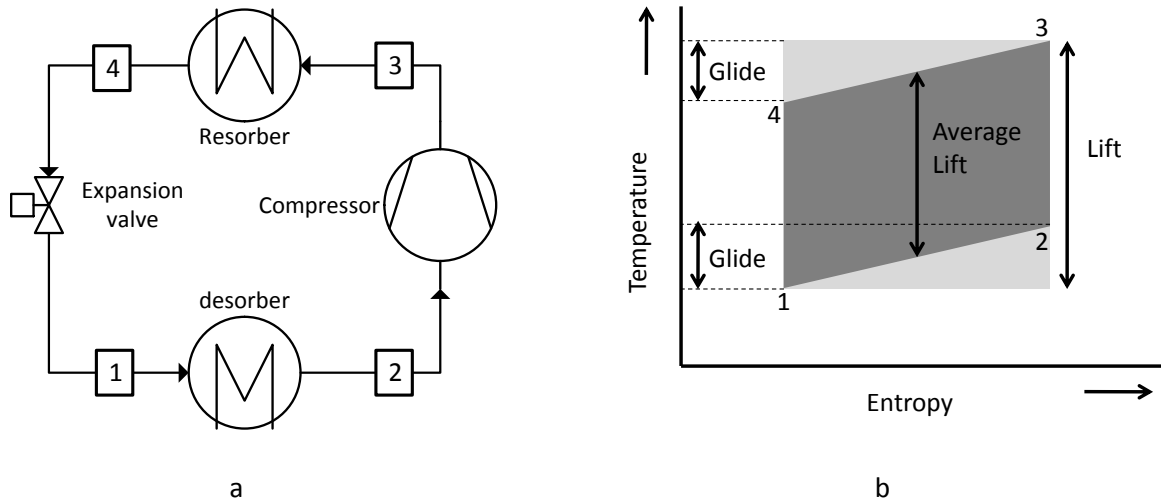
Fig. 1.1. a. Lay-out of a compression-resorption heat pump using wet compression. In the desorber a liquid vapor mixture is heated up and thereby further desorbed until it reaches the compressor inlet. The mixture is compressed and the vapor is absorbed in the resorber thereby releasing heat at high temperature b. The compression-resorption heat pump process (dark grey) in a temperature-entropy diagram. State points are identical to a. The reduction on average lift is clearly demonstrated by comparing to a conventional heat pump working with a pure fluid (light grey).
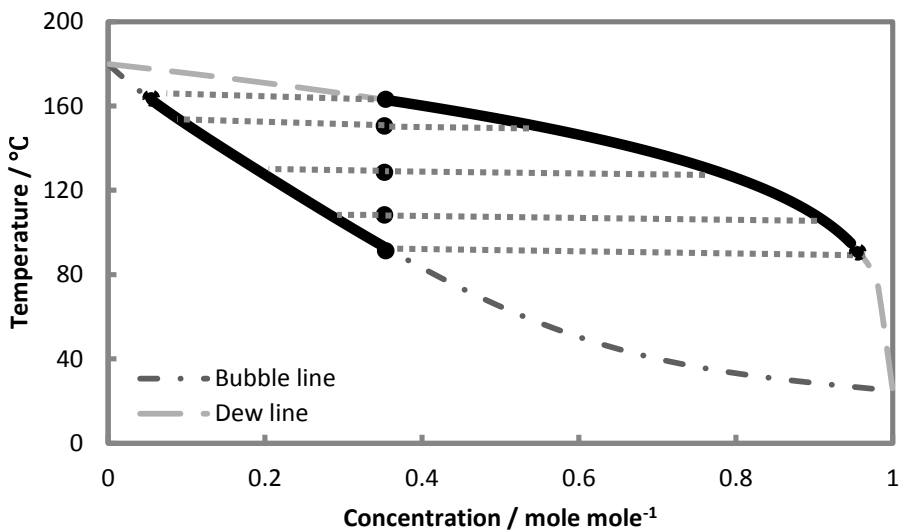
Fig. 1.2. Phase change of a two component ammonia-water mixture illustrated in a temperature-concentration diagram. In this example the mixture concentration is 35% and the pressure is 10 bar. As soon as the first liquid forms, the concentration of the vapor increases because initially mainly the heavy component exists in the liquid. As temperature decreases, the vapor concentration further increases. Finally all vapor is absorbed in the liquid, which has now the same concentration as the vapor at the start of the process.
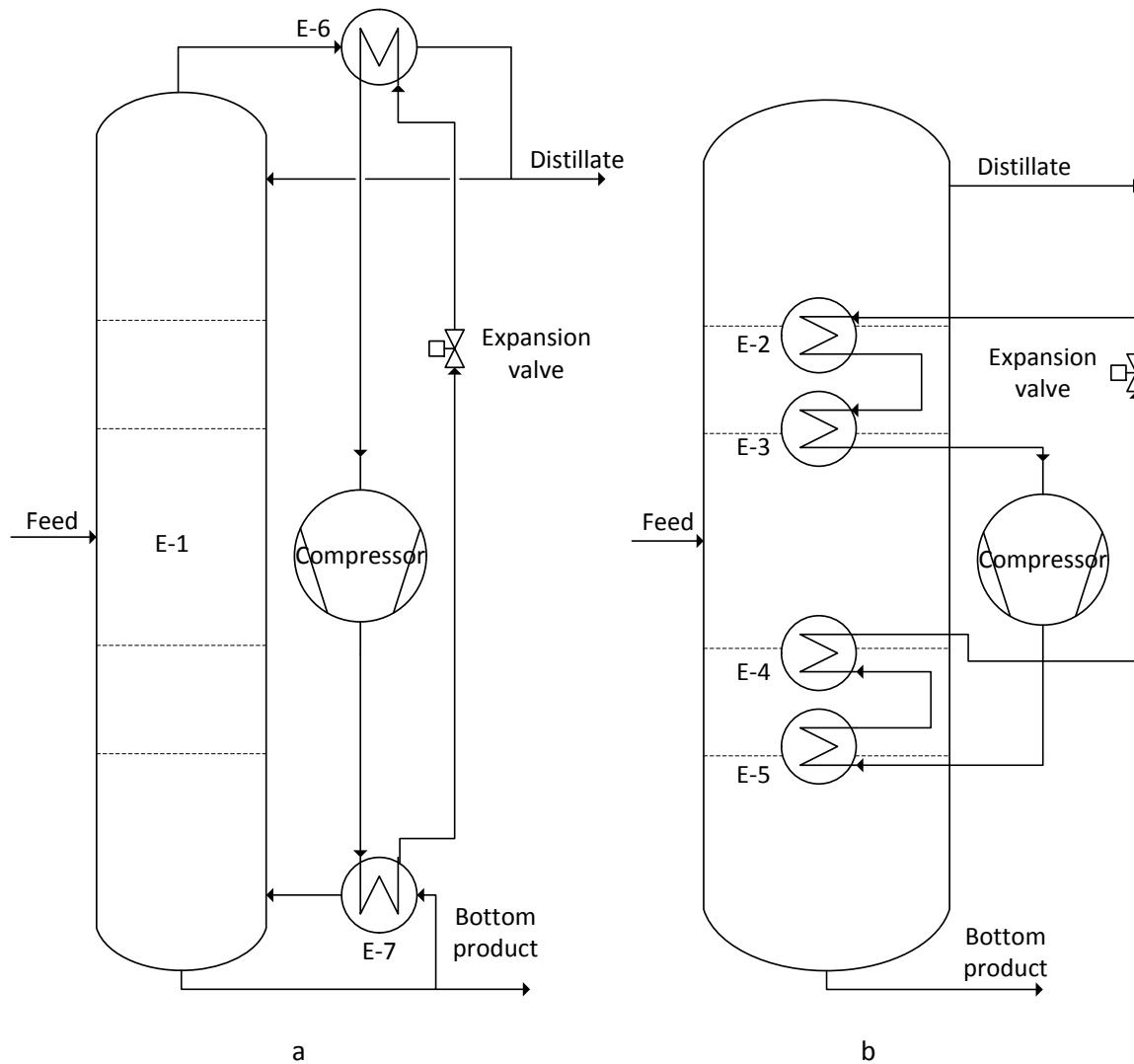
Fig. 1.3 a Compression resorption heat pump applied externally to a distillation column. b. Compression-resorption heat pump applied internally to a distillation column.

Compression-resorption heat pumps typically consist of a compressor, two heat exchangers (desorber and resorber) and an expansion valve. In the desorber a liquid-vapor ammonia-water mixture is heated up and thereby further desorbed until it reaches the compressor inlet.

The mixture is compressed and the vapor is absorbed in the liquid in the resorber, thereby releasing heat at elevated temperature. The basic lay-out of a compression-resorption heat pump is presented in Fig. 1.1. More information on compression-resorption heat pumps and wet compression can be obtained from [44, 116]. Two phase heat transfer for mixtures differs from condensation of a pure fluid because the phase change is not isothermal, gas and liquid phase have different concentrations, and the concentration of both phases changes during the phase transition [112]. The temperature and concentration changes during phase transition are presented in the temperature-concentration diagram in Fig. 1.2.
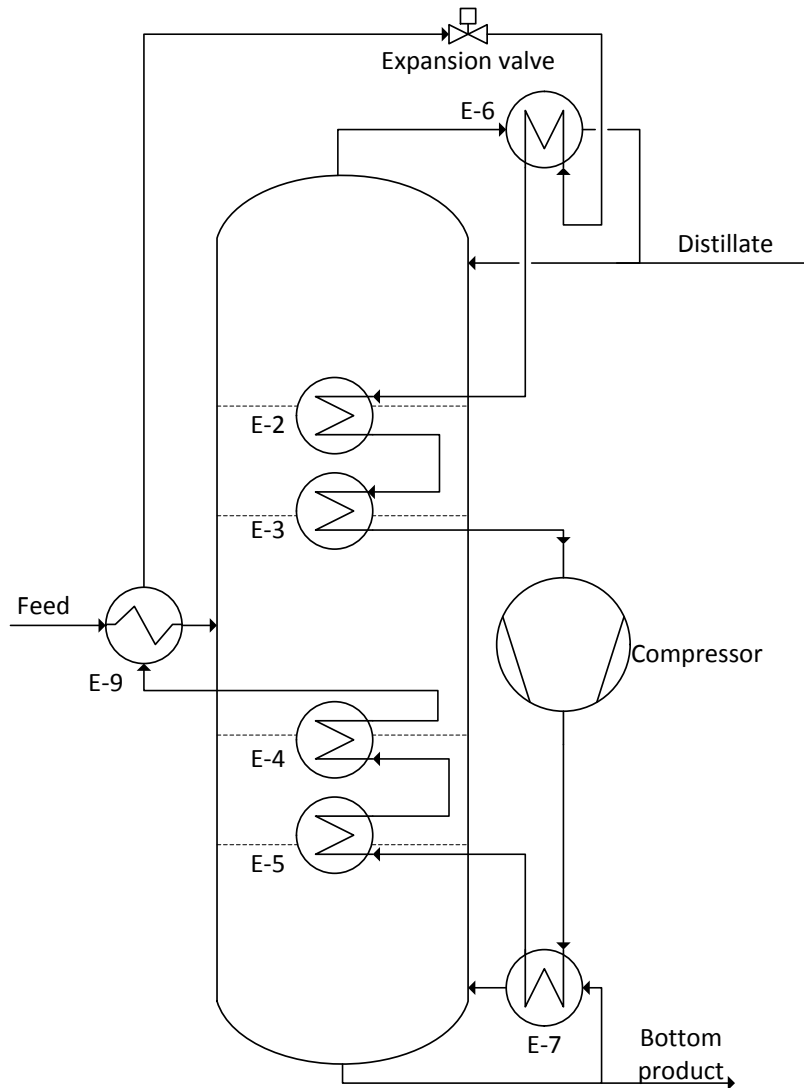
Fig. 1.4. Compression resorption heat pump integrated into a distillation column. Placing (part of) the desorber, E-2 and E-3, and resorber (E-4 and E-5) on the trays allows the heat pump to make use of a larger available temperature glide, thereby increasing its efficiency.

A compression-resorption heat pump can be added to distillation columns in multiple ways:

1. Externally, the column condenser and reboiler are integrated with the heat pump heat exchangers. The distillation column operates under adiabatic conditions, see Fig. 1.3a
2. Internally, the heat exchangers of the heat pumps are placed on the trays of the columns. The distillation column operates under diabatic conditions, see Fig. 1.3b
3. Combination of both, see Fig. 1.4.
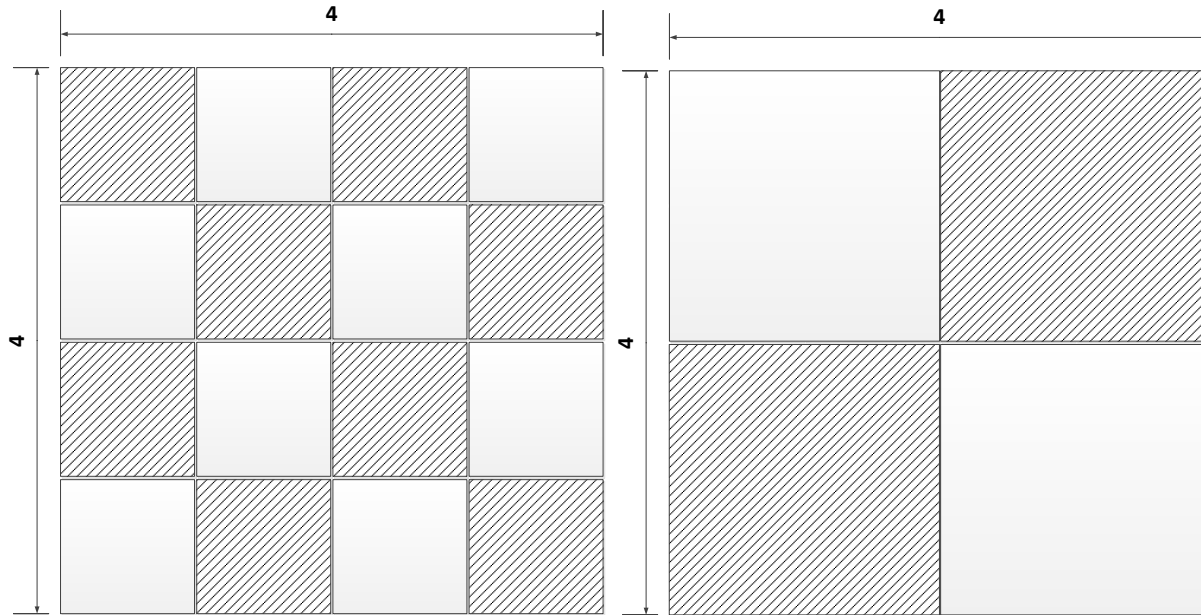
Fig. 1.5. Cross-sectional view of a heat exchanger comprised of small (left) and large (right) tubes. Both heat exchangers have the same overall dimensions of 4 x 4 lengths. Halving the hydraulic diameter doubles the heat exchanger surface area, the edges of each square, assuming equal tube lengths.

The first option is often used with conventional heat pumps, since the process fluids are relatively pure at the condenser and reboiler, showing only a very small temperature glide. The refrigerants used in conventional heat pumps are usually pure also, matching the glide and making them ideal to place externally. Downside of this option is that the heat exchangers are located at the temperature extremes of the process; there where the required temperature lift is highest.

Since the compression-resorption heat pump allows for a temperature glide, it can match the temperature changes over the trays of the column. Fig. 1.4 presents a compression-resorption heat pump integrated into a distillation column using option 3, where the desorber and resorber are integrated with the condenser and reboiler, respectively, and on the trays of the column for maximum system efficiency. For more details on coupling heat pumps to distillation columns the reader is referred to refs. [8, 19, 58, 87, 88, 97].

1.1 Heat exchanger area

One of the major problems for the acceptance of heat pumps in the process industry is their capital cost. Low temperature driving forces to boost the efficiency of the heat pump can be attained either by large amounts of heat exchanger surface area, a large heat transfer coefficient, or preferably, both. One type of heat exchanger featuring large surface area to volume ratio and high heat transfer coefficient values is the so-called mini channel heat exchanger.

The large surface to volume area ratio is a consequence of the small tubes. This can be best explained with the help of Fig. 1.5. It is shown that halving the tube diameter increases the number of tubes by a factor of four. Since the perimeter of the tubes is only half the perimeter of the larger tubes, the total perimeter is doubled. When assuming equal tube lengths this results in a doubling of surface area.

For single phase flows it can be shown that the heat transfer coefficient increases with decreasing diameter, given the same flow conditions expressed in terms of Reynolds and Prandtl numbers. Halving the diameter simply halves the normal distance from the inside tube to the wall. The Nusselt number *Nu* is a dimensionless heat transfer coefficient which is, in single phase flow, only dependent on the shape of the channel and the flow conditions. The heat transfer coefficient obtained from the Nusselt number is given by

$$hc = \frac{Nu\lambda}{d_H} \tag{1.1}$$

For the volume of the heat exchanger applies:

$$\text{Volume} \sim d_H^2 \tag{1.2}$$

At the same flow conditions, the heat transfer coefficient thus increases linearly with the inverse of the hydraulic diameter. Since both the heat transfer coefficient and the surface area per volume increase linearly with the inverse of the hydraulic diameter, the total heat transferred in the same volume increases quadratically with the inverse of the hydraulic diameter. Mini-channel heat exchangers lead to significantly more compact heat exchangers.

1.2 Research objective

The main objective of this research is to improve the performance and reduce the investment costs of compression-resorption heat pumps for utilization in the process industry. To gain better insight in the capabilities of conventional systems, the technical and economic performance of conventional industrial heat pumps is first explored. Then the benefits of the application of compression-resorption heat pumps to real distillation processes are studied in more detail.

Ways to improve the performance of compression-resorption heat pumps are improvement in the heat exchangers, compressor and expansion equipment. Usually by improving such components, the investment costs rise. Mini-channel heat exchangers offer the possibility to increase the performance and lower the costs of the heat exchanger system because less material is required. The actual performance of a coaxial tube mini-channel is experimentally investigated.

In case many channels need to be applied, distributing the flow equally over the channels becomes more difficult. The distribution performance of the fluid distributors in a shell and tube heat exchanger with 116 tubes is investigated in order to gain insights in the distribution performance. In a second step, ammonia-water vapor-liquid mixtures have been used to gain knowledge of the heat transfer performance of such heat exchangers under conditions similar to the conditions in a compression-resorption heat pump.

1.3 Outline of this thesis

This thesis is organized as follows.

In chapter 2, a simplified model for the performance evaluation of different types of heat pumps is proposed. More complex heat pump cycle calculations are avoided. In the same chapter a cost model proposed by Guthrie [34] and updated for current economic conditions is presented. Combining such models allows for a quick selection of the most appropriate heat pump types and determines the feasibility of the implementation.

Chapter 3 presents a more detailed model specific for compression-resorption heat pumps. This model is used to accurately determine the efficiency of heat pumps if integrated into a set of industrial separation processes. Furthermore the influence of the concentration of ammonia in the ammonia-water mixture is analyzed. The efficiency model described in chapter 2 is compared against the model presented in this chapter in order to determine the accuracy of the former model when applied to compression-resorption heat pumps.

Since increased heat transfer area and larger heat transfer coefficients in the heat exchanger of heat pumps can result in smaller and more cost efficient heat pumps, single tube experiments using a mixture of ammonia and water as working fluid have been performed. Chapter 4 focusses on a study of the absorption process in the annular side of this heat exchanger.

After the description of an experimental investigation on the annular side of the heat exchanger in chapter 4, Chapter 5 continues with the discussion of experiments performed on the tube side of the heat exchanger. Instead of using water in the tube, an ammonia-water mixture was used and the setup was operated in the two-phase region under desorption conditions.

Although a small sized heat pump can be realized using the heat exchangers discussed in chapters 4 and 5, process industry demands for larger heat duties. Chapter 6 presents both experimental and numerical results for the flow distribution and heat transfer in a heat exchanger comprised of 116 tubes. Distributing the flow evenly to several tubes is a major problem in heat exchanger design. Chapter 7 treats the heat transfer and pressure drop performance of this heat exchanger under absorption and desorption conditions.

The final chapter includes the main conclusions and recommendations of this study.

This thesis is the result of work performed within the framework of project "BC-00-02 Heat pumps in bulk separation processes" from the Institute for Sustainable Process Technology (ISPT). The project has received financial support from the partners of the ISPT, which is a cooperation between industry, universities and knowledge institutes. The aim of the ISPT is to increase the competitiveness of the Dutch process industry by speeding up innovation processes and making them more efficient.

The goal of the BC-00-02 project is to identify novel heat pump concepts and further develop the most promising solutions, which were determined to be the thermo-acoustic heat pump researched by ECN and the compression-resorption heat pump researched by the Delft University of Technology – Process and Energy Department.

The industrial parties and academic partners involved in this project are in alphabetical order AkzoNobel, Bronswerk Heat Transfer BV, DSM, ECN, Huntsman, LyondellBasell, TU Delft – Process and Energy Department. The work presented in this thesis summarizes the contribution of the Delft University of Technology – Process and Energy Department.

2 HOW TO QUICKLY SELECT INDUSTRIAL HEAT PUMP TYPES INCLUDING THE IMPACT OF THERMODYNAMIC LOSSES

Making a rough performance estimate for conventional vapor compression and vapor recompression heat pumps is straightforward: Dividing the Carnot efficiency by 2 results in a reasonable estimate. Still, actual performance of heat pumps could easily vary to a large extent.

With new and innovative heat pumps the discrepancies between the rough estimate and actual performance might be even larger as the Carnot efficiency is not the upper limit anymore due to the occurrence of temperature glides. The definition of a proper index of performance is required. Lack of a simple method to determine the approximate performance of a heat pump can hinder the implementation of these novel types in industry.

In this chapter a performance map is presented and it is shown that, for mechanical heat pumps, making use of the available temperature glide increases the energy conversion performance and reduces the payback period. Heat driven absorption heat pumps and vapor (re)compression heat pumps have the smallest pay back times when the process is characterized by low temperature glides. Mechanical heat pumps capable to work with large temperature glides in the heat exchangers are more effective at higher temperature lifts when such temperature glides are available. Due to improved performance, these mechanical heat pumps are able to achieve better economical results over their technical life time although they require higher initial investment.

This chapter is for a large part based on:

D.M. van de Bor, C.A. Infante Ferreira, *Quick selection of industrial heat pump types including the impact of thermodynamic losses*, Energy, Volume 53, 2013, 312-322.

2.1 Introduction

Heat pumps generally have a significant efficiency effect on the energetic performance of processes in industry. Heat pumps are becoming more and more interesting for industry due to increasing energy cost and limitations on CO_2 emissions. With newly developed heat pump types it is not always straightforward to select a certain type of heat pump for a specific industrial process application.

Although the proposed method is more widely applicable, this chapter focusses on the application of heat pumps at one of the large energy users of the process industry [56, 83]: distillation columns [16]. Distillation columns are process installations, where a mixture of two or more components is separated on the basis of difference in volatility. The columns generally require a large heat input in the boiler and release a similar amount of heat in the condenser, most often to environment.

Several studies about the selection of heat pumps have been published. Omideyi et al. [84] developed an early selection scheme for vapor compression heat pumps applied to distillation systems. Fonyo and Mizsey [26] simplified the selection method and included vapor recompression as well as absorption heat pump schemes. Both publications give limited detail of the heat pump and focus more on the column properties.

Aiming at the prediction of the performance of reversed heat pumps, namely chillers, Allen and Hamilton [3] created a steady state model for reciprocating water chillers to evaluate performance at full and part load. Hamilton and Miller [36] developed a model capable of predicting heat pump efficiency by applying equation-fitting methods to manufacturers catalog data of individual heat pump components along with thermodynamic relationships for the working fluid. It requires internal refrigerant pressures and temperatures. Angelino and Invernizzi [4] investigated different refrigerants and showed that the efficiency depends on the complexity of the molecular structure, reduced temperature at which evaporation occurs and the temperature lift. McLinden [72] performed a similar research and actually came to the same conclusions. Högberg et al. [40] used three methods for comparing heat pump cycle performance for heat pumps working with pure fluids as well as non-azeotropic mixtures. They assume, as far as the heat exchangers are concerned, equal minimum temperature approaches, equal mean temperature differences and equal heat exchange area. They concluded that by assuming equal mean temperature differences the COP can be estimated with the same accuracy for pure fluids as well as for mixtures. Ait-Ali [1] investigated the performance of irreversible cooling and heating cycles. He defined a single irreversibility factor which transforms the Clausius inequality into an equality to simplify the model. Yilmaz [115] analyzed the performance of heat pumps using non-azeotropic mixtures and suggested a simplified relation to determine the COP for systems with a temperature glide. More recently, Kiss et al. [56] created a selection scheme for selecting energy saving distillation processes and heat pumps based on practical considerations.

Heat pumps have been the topic of a large amount of papers in relation to industrial applications. Some of these publications are related to the topic of this chapter and are shortly discussed here. Wall [106] discussed the application of thermoeconomics, which includes both the exergy concept and price of utilities, for optimization of single-stage vapor compression heat pump cycles. Neelis et al. [78] prepared energy and carbon balances for a large number of bulk chemical processes. These authors quantified the

process energy use in relation to the heat effects of chemical reactions and so the energy inputs that do not end up in the useful products. Heat pumps can convert a significant part of these losses into useful process heat. The integration of absorption heat pumps in industrial processes has been discussed by Costa et al. [18] and Bakhtiari et al. [6]. These studies include economic evaluations of the integration of heat pumps in specific industries.

Several technical options to upgrade low temperature heat have been proposed and economically evaluated by Smolen and Budnik-Rodz [93]. The comparison includes vapor compression and absorption heat pumps. Ajah et al. [2] investigated the upgrading of industrial low temperature heat making use of chemical and vapor compression heat pumps. These authors extended the economic analysis with reliability and safety aspects. More recently Little and Garimella [64] compared a number of alternatives to upgrade low temperature heat including absorption heat pumps.

This chapter considers heat pump performance independent of refrigerant properties by starting from the fairly simple Carnot relation. This relation is modified to include temperature glides, temperature differences between process and heat pump and isentropic efficiency of the compressor.

Final goal of this investigation is to present an economic performance map from which heat pumps can be directly selected under given process conditions, with the focus on compressor driven heat pumps. The map is constructed by integrating heat pump efficiency relations with economic data for compressors and heat exchangers and defining economic selection criteria.

A comparison is made between vapor compression/recompression, compression-resorption and transcritical heat pumps. Absorption heat pumps and conventional boilers are included as references. In combination with the aforementioned selection scheme by Kiss et al. [56] process engineers can save tremendous time by narrowing down the number of technology alternatives and obtain the economic performance of these alternatives, making selection simpler.

2.2 Heat pump classification

Heat pumps can be divided into 3 types: mechanically driven, heat driven and heat transformers. The main difference between the types is the way they are powered: The mechanically driven heat pumps add energy to the system with high quality: electricity or mechanical energy. Heat driven heat pumps are powered by high quality heat, while heat transformers are driven by the same low quality heat stream that should be upgraded [23, 73].

2.2.1 Mechanically driven heat pumps

Mechanically driven heat pumps are briefly described in the following subsections. The following types are discussed:
- (Subcritical) vapor compression heat pump
- Vapor recompression heat pump
- Transcritical vapor compression heat pump
- Compression-resorption heat pump
- HIDiC
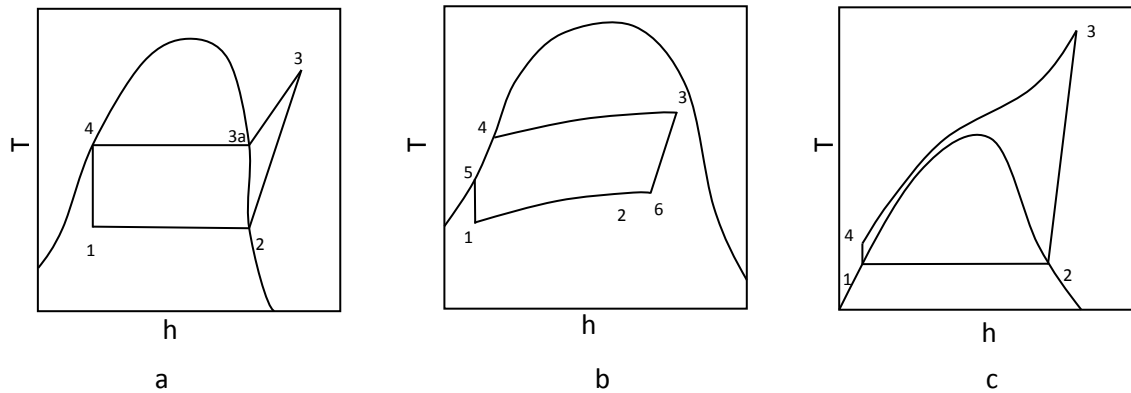- Thermoacoustic heat pump (linear motor driven)

Fig. 2.1. Typical temperature-enthalpy diagrams for (a) subcritical vapor compression, (b) compression-resorption and (c) transcritical vapor compression heat pumps. Pos 1 indicates the process conditions after the expansion valve, 2 indicates the conditions after the evaporator (a,c) or desorber (b), 3 indicates the conditions at the outlet of the compressor and 4 indicates the conditions at the outlet of the condenser (a), resorber (b) or gas cooler (c). In case an internal heat exchanger is present in a compression-resorption heat pump, the liquid from the resorber outlet at condition 4 is subcooled to the conditions at state point 5, while using the heat to extend the desorption process from state point 2 to 6.

2.2.1.1 *Vapor compression heat pump, VCHP*

A vapor compression heat pump consists of 4 main components: evaporator, compressor, condenser and expansion valve. For subcritical vapor compression heat pumps working with pure working fluids there is no temperature glide present in both the condenser and evaporator. Superheat is required at state point 2 (see Fig. 2.1a) to protect the compressor from getting damaged by liquid droplets. Best application is in areas where a low temperature lift is required and where the temperature glide of the heat source and heat sink is (almost) 0 K. This is usually the case in the reboiler and condenser at a distillation process of close boiling mixtures with very pure top and bottom products. Higher temperature lifts can be achieved when using multistage heat pump systems, however it should be noted that nonetheless efficiency decreases with increasing temperature lift.

2.2.1.2 *Vapor Recompression Heat Pump, VRHP*

Vapor recompression heat pumps are open loop heat pumps. They are generally applied with an (almost) pure fluid; therefore the temperature glide over the condenser is almost 0 K. The overhead vapors are generally compressed and then condensed while heating the reboiler. In some cases the bottom flow is flashed, heat is picked up in the column condenser and then compressed to the pressure of the bottom stream of the column (bottom flash) [26].

2.2.1.3 *Compression-Resorption Heat Pump, CRHP*

Compression-resorption heat pumps work with a binary mixture; most often ammonia/water [46]. As a mixture generally has a boiling trajectory, there will always be a temperature glide over desorber (statepoints 1 to 2 in Fig. 2.1b) and resorber (statepoints 3 to 4 in Fig. 2.1b). Using specially designed compressors it is possible to compress liquid/vapor mixtures [43]. Usually a vapor/liquid separator is placed at the end of the desorber; thus saturated vapor is compressed and liquid is pumped up to higher pressure.

2.2.1.4   Transcritical Vapor Compression Heat Pump, TCHP

A transcritical vapor compression heat pump consists at least of an evaporator, compressor, gas heat exchanger and expansion valve. A temperature profile exists over the gas heat exchanger; however, due to the supercritical nature of the heat pump working fluid in this part of the heat pump, no phase change takes place. The evaporator, where the fluid is subcritical, has zero temperature glide and the fluid undergoes a phase change. Transcritical vapor compression heat pumps can achieve relatively high lifts with reasonable efficiency as long as temperature glides match the glides of the source and sink. Transcritical CO_2 heat pumps are commonly applied for space heating and hot water generation, as the critical pressure and temperature (31 °C) of CO_2 make the heat pump suitable for this application. For the application in distillation systems, where the minimum source temperature is 90 °C or more, a fluid with a higher critical temperature has to be identified as the source temperature is limited by the critical temperature of the fluid. Sarkar et al. [90] investigated some alternatives to CO_2 as refrigerant in transcritical cycles. The cycle is depicted in the temperature-enthalpy diagram in Fig. 2.1c.

2.2.1.5   Heat Integrated Distillation Column, HIDiC

In certain cases it is possible to split the process into two parts. An example is a distillation column where the rectifier and stripping section can be split from each other and exchange heat. In order to exchange heat, and thereby make use of heat integration [27, 71, 77], the rectification section has to work at higher temperature and therefore higher pressure than the stripping section. This is reached by placing a compressor at the top of the stripping section and an expansion valve at the bottom of the rectification section. Possible advantage compared to compression-resorption heat pumps is the lack of one temperature driving force. The operating principle of a HIDiC is shown in Fig. 2.2.

2.2.1.6   Linear Motor Driven Thermo Acoustic Heat Pump, TAHP

Thermo acoustic heat pumps are currently in the development stage. Since 2001, ECN is working on its development in the Netherlands [95]. Except for the linear motor, the thermo acoustic heat pump has no moving parts and therefore it is expected that this type of heat pump will have lower maintenance costs compared to other mechanically driven heat pumps.

In a TAHP heat is gained from a low temperature heat sink and delivered to a regenerator by means of sound waves. These sound waves create pressure pulsations, such that there are regions where compression and heating takes place, and other regions where expansion and cooling takes place. This pulsating behavior allows transfer of heat from a cold heat exchanger through a regenerator to a hot heat exchanger.
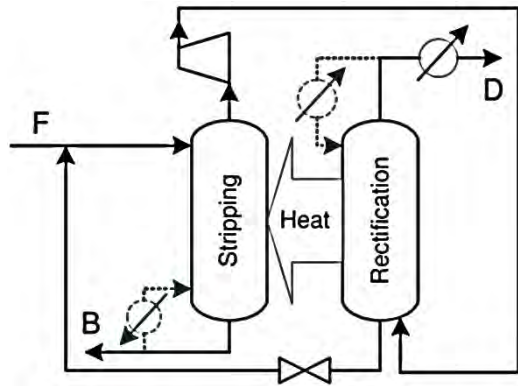
Fig. 2.2. HIDiC working principle (Olujic et al.[83]). The column is split into two sections whereby the rectification section is operating at higher temperature and pressure, which allows transfer of heat from the rectification to the stripping section.

2.2.2 Thermally driven heat pumps

Among thermally driven heat pumps the absorption heat pump (AHP) is often applied. This type of heat pump is able to reduce energy costs at high temperature lifts, but is less favorable than mechanically driven heat pumps. The heat driven heat pumps are characterized by a lower COP than mechanically driven heat pumps, but they don't require large amounts of electric or mechanical energy to drive a compressor, thereby making use of the lower prices for heat or fuel. High quality heat is delivered at a generator where desorption takes place. The vapor is then condensed in the condenser close to the desired process temperature. After the condensation process the liquid is expanded, allowing heat to be picked up from a low temperature source, for instance the condenser of a distillation column. The refrigerant can then finally be absorbed in the absorber, exchanging heat at temperatures close to the process temperature. It has been shown [18, 111] that absorption heat pumps are a feasible option in different industries.

2.3 Comparison of the performance of different cycles

The sections above indicate globally the best heat pump under certain process conditions, but it speaks in relative terms, i.e. low/high temperate lift, a certain amount of glide. The goal of this section is to provide a map of where to apply a certain heat pump. This will be done on the basis of energy efficiency and on the basis of expected costs. Although this map will give a picture as good as possible, it is based on general assumptions and should only be used as a guideline.

All heat pumps perform best when working with low temperature lifts. The most simple and most developed heat pump types are vapor compression and vapor recompression heat pumps. Although they are the most developed, the temperature lifts that can be reached by these types of heat pumps are limited. Like vapor compression and vapor recompression heat pumps, HIDiCs and compression resorption heat pumps reach their highest efficiency at low temperature lifts. However, their relative advantages compared to the more conventional vapor compression and vapor recompression heat pumps become larger when temperature lift increases.

2.3.1 Comparison of advanced heat pump cycles with vapor compression heat pumps

Heat driven heat pumps can become energetically advantageous when the COP of a compressor driven heat pump is small.

$$COP_H > COP_E \frac{\eta_E}{\eta_H}$$

(2.1)

Where η_E, η_H, COP_E and COP_H are the grid efficiency, boiler efficiency, COP of mechanical/electric driven heat pumps and COP for heat driven heat pumps, respectively. The electrical COP_E can be defined as

$$COP_E = \eta_{\mathrm{Carnot}} COP_{\mathrm{Carnot}}$$

(2.2)

Where η_{Carnot} is the efficiency relative to the Carnot COP.

2.3.1.1 Vapor (Re)compression Heat Pumps

When there is no temperature glide, i.e. for vapor compression heat pumps, COP_{Carnot} is given by

$$COP_{\mathrm{Carnot}} = \frac{T_h}{T_h - T_l}$$

(2.3)

With T_h and T_l the sink and source temperatures.

2.3.1.2 Compression-Resorption Heat Pump

The COP_{Carnot} for a compression resorption cycle is similar to the COP of the Lorentz cycle [46], which can be used in case of the occurrence of a temperature glide over phase transition. Following the definitions for source and sink temperatures,

$$COP_{\mathrm{Lorentz}} = \frac{\dfrac{\Delta T_{h,\mathrm{glide}}}{ln\left(\dfrac{T_h}{T_h - \Delta T_{h,\mathrm{glide}}}\right)}}{\dfrac{\Delta T_{h,\mathrm{glide}}}{ln\left(\dfrac{T_h}{T_h - \Delta T_{h,\mathrm{glide}}}\right)} - \dfrac{\Delta T_{l,\mathrm{glide}}}{ln\left(\dfrac{T_l + \Delta T_{l,\mathrm{glide}}}{T_l}\right)}}$$

(2.4)

With $\Delta T_{l,glide}$ and $\Delta T_{h,glide}$ the available glides in source and sink temperatures. Instead of using the definition above, Yilmaz [115] suggests to use an approximate equation

$$COP_{\mathrm{Lorentz}} = \frac{2T_h - \Delta T_{h,\mathrm{glide}}}{2T_h - \Delta T_{h,\mathrm{glide}} - 2T_l - \Delta T_{l,\mathrm{glide}}}$$

(2.5)
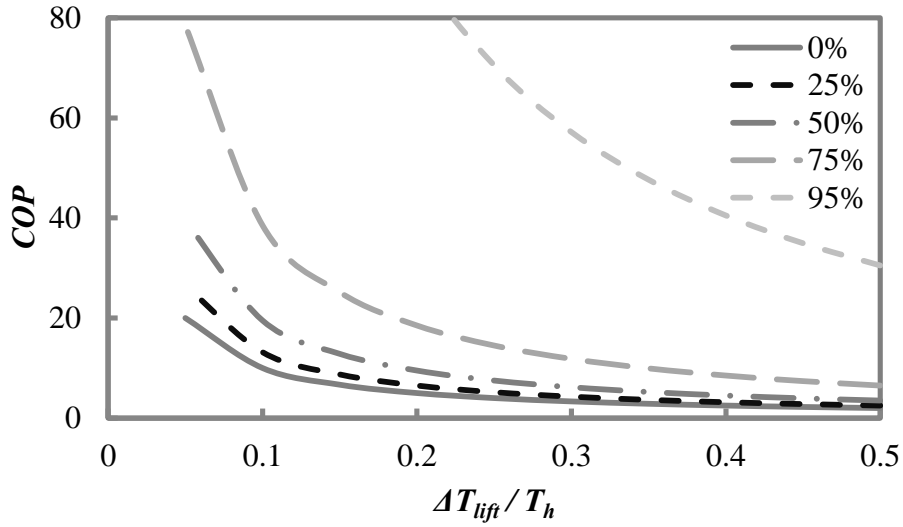
(a)
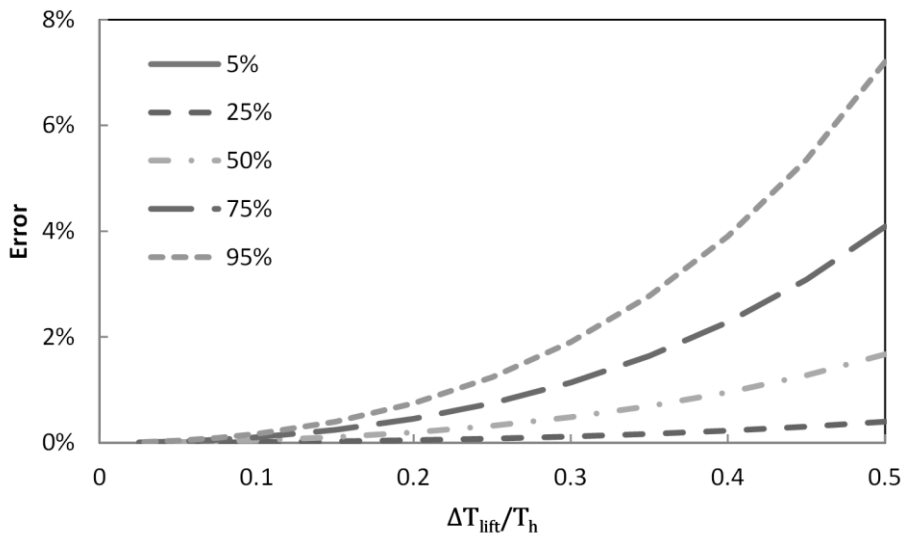
(b)

Fig. 2.3. (a) COP as function of dimensionless lift and dimensionless glide and (b) error made by implementation of Yilmaz [115] method for determining Lorentz COPs. The lines indicate the ΔT_{glide} to ΔT_{lift} ratio in percent.
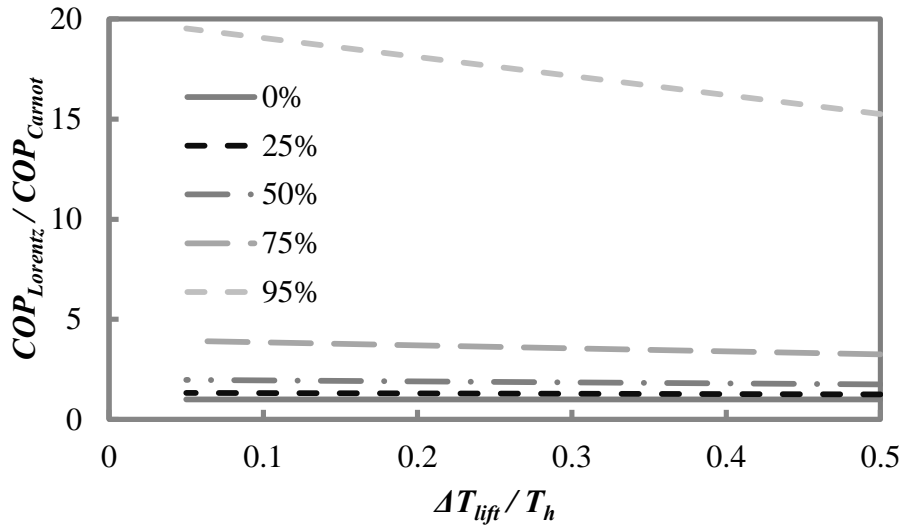
(a)
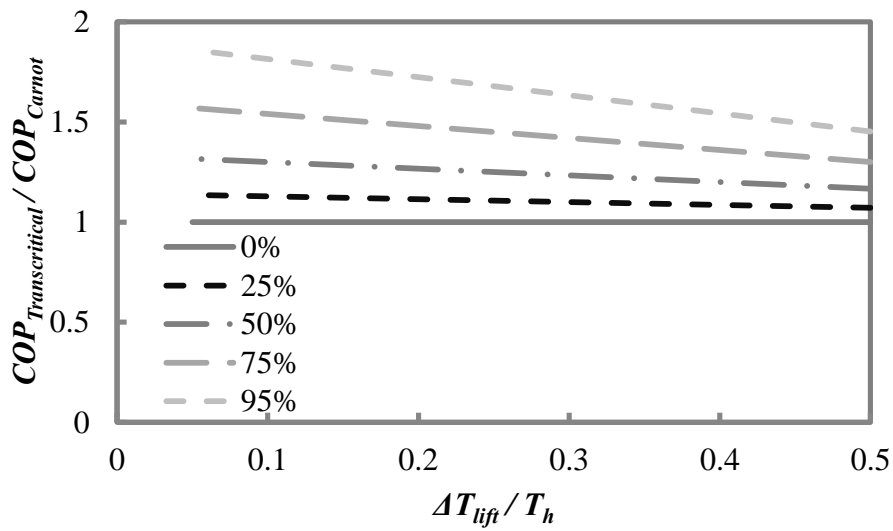
(b)

Fig. 2.4. (a) Ratio of Lorentz COP and Carnot COP and (b) Ratio of Transcritical COP and Carnot COP, both as a function of dimensionless temperature lift with the ΔT_{glide} to ΔT_{lift} ratio (in percent) as parameter.

Simplifying this equation by taking equal glides for both the low and high temperature side results in

$$COP_{Lorentz} = \frac{2T_h - \Delta T_{\text{glide}}}{2\Delta T_{\text{lift}} - 2\Delta T_{\text{glide}}}$$

(2.6)

With

$$\Delta T_{lift} = T_h - T_l$$

(2.7)

The Carnot and Lorentz COP's for different glides result in the graph shown in Fig. 2.3.

The approximation introduced when eq. (2.6) is used instead of the exact formulation, eq. (2.4), is dependent on the inverse of Carnot and glide to lift ratio and is illustrated in the bottom of Fig. 2.3. The deviation between the approximation of Yilmaz [115] and eq. (2.4) varies between 0 % (at 0 % glide and/or 0 % lift) and 7 % (at 95 % glide and 50 % lift). Although not 100 % accurate, the simplification by Yilmaz allows obtaining relatively simple relations between efficiencies due to the absence of the natural logarithm. Division of Eq. (2.6) by Eq. (2.3) simplifies to

$$\frac{COP_{\text{Lorentz}}}{COP_{\text{Carnot}}} = \left(1 - \frac{1}{2}\frac{\Delta T_{\text{lift}}}{T_h}\frac{\Delta T_{\text{glide}}}{\Delta T_{\text{lift}}}\right)\frac{1}{1 - \frac{\Delta T_{\text{glide}}}{\Delta T_{\text{lift}}}}$$

(2.8)

The results for different lift-to-sink temperature ratios are given in Fig. 2.4a, illustrating that heat pumps that can make use of glides may lead to significant improvements in comparison to conventional heat pumps.

2.3.1.3 Transcritical Heat Pumps

For a transcritical heat pump the evaporator temperature is constant, while for the gas heat exchanger operating in the supercritical region the temperature changes along the heat exchanger. Equations (2.6) and (2.8) are replaced by eqs. (2.9) and (2.10). The behavior of eq. (2.10) is shown in Fig. 2.4b.

$$COP_{transcritical} = \frac{2T_h - \Delta T_{h,\text{glide}}}{2T_h - \Delta T_{h,\text{glide}} - 2T_l} = \frac{2T_h - \Delta T_{\text{glide}}}{2\Delta T_{lift} - \Delta T_{\text{glide}}}$$

(2.9)

$$\frac{COP_{transcritical}}{COP_{Carnot}} = \left(1 - \frac{1}{2}\frac{\Delta T_{\text{lift}}}{T_h}\frac{\Delta T_{\text{glide}}}{\Delta T_{\text{lift}}}\right)\frac{1}{1 - \frac{\Delta T_{\text{glide}}}{2\Delta T_{\text{lift}}}}$$

(2.10)

Comparing Fig. 2.4a and Fig. 2.4b also shows that the potential of transcritical heat pumps is significantly lower than the potential of compression-resorption heat pumps.

2.3.1.4 Absorption heat pumps

To determine the ideal performance of absorption chillers, Kaushik et al. [50] suggest

$$COP_{cooling} = \left(\frac{T_{gen} - T_{abs}}{T_{gen}}\right)\left(\frac{T_{evap}}{T_{con} - T_{evap}}\right)$$

(2.11)

The difference in COP for cooling and heating applications is given by eq. (2.12),

$$COP_{heating} = COP_{cooling} + 1$$

(2.12)

For industrial heat pumps it can be assumed that the temperatures for the absorber and condenser are equal (= T_h) as they both deliver heat to the process and the evaporator temperature is the source temperature (T_l), then the COP for an absorption heat pump is given by eq. (2.13).

$$COP_{ahp} = \left(\frac{T_{gen} - T_h}{T_{gen}}\right)\left(\frac{T_l}{T_h - T_l}\right) + 1$$

(2.13)

2.4 Loss mechanisms

In heat pumps, there are several sources of efficiency losses which are shortly explained in the following subsections:

- Temperature driving forces
- Compressor inefficiency
- Pressure drop
- Superheating
- Throttling losses
- Non-equal process fluid and heat pump fluid temperature glide

In this section an attempt is made to quantify the losses due to temperature driving forces and compressor efficiency. Mismatches between process fluid temperature glide and heat pump fluid temperature glide are not included as they should always be avoided. Pressure drop, superheating and throttling losses have not been included since their values are strongly related to the working fluids.

2.4.1 Temperature driving forces

Heat transfer does not occur without a difference in temperature between a cold and warm stream. This temperature driving force doesn't allow a heat exchanger design to be 100 % effective. For instance, a hot stream entering a heat exchanger with temperature T_4 is being cooled down by a second flow with a temperature of T_1. While the hot stream will never reach T_1, the cold stream will never reach T_4, unless the heat exchanger is infinitely large, see Fig. 2.5.

T_1 T_2

$\dot{Q}$

T_3 T_4
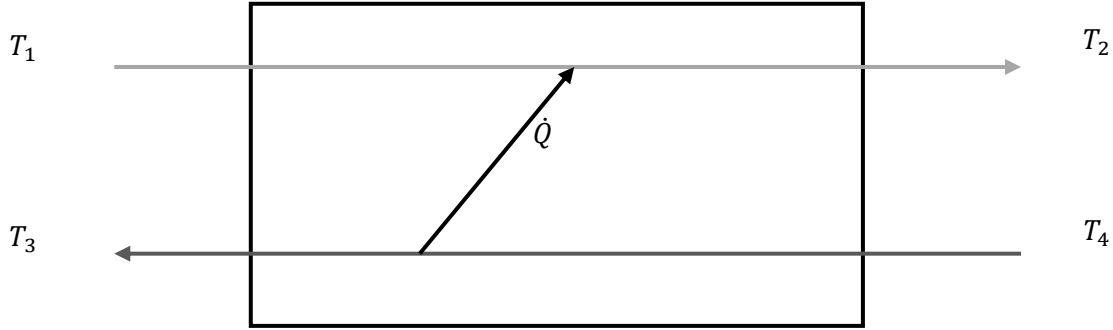
Fig. 2.5. Temperature driving forces in heat exchangers. Increasing the driving forces increases the irreversible losses and therefore decreases the efficiency of the heat pump.

2.4.1.1 Vapor compression cycles

The temperature driving forces (TDF) affect the total efficiency of the heat pump. In eq. (2.14) the TDF are included in the COP.

$$COP_{TDF} = \frac{T_h + \Delta T_{h,\text{driving}}}{\left(T_h + \Delta T_{h,\text{driving}}\right) - \left(T_l - \Delta T_{l,\text{driving}}\right)} = \frac{1}{1 - \dfrac{T_l - \Delta T_{l,\text{driving}}}{T_h + \Delta T_{h,\text{driving}}}} \tag{2.14}$$

The efficiency loss due to the temperature driving forces can be determined. The equation gets simpler by assuming the driving forces for source and sink to be equal.

$$\eta_{\text{Carnot}}^{TDF} = \frac{COP_{TDF}}{COP_{\text{Carnot}}} = \frac{\dfrac{T_h + \Delta T_{\text{driving}}}{T_h + \Delta T_{\text{driving}} - T_l + \Delta T_{\text{driving}}}}{\dfrac{T_h}{T_h - T_l}} \tag{2.15}$$

Then rewriting, simplifying and back-substituting the Carnot COP results in eq. (2.16).

$$\eta_{\text{Carnot}}^{TDF} = \frac{COP_{\text{Carnot}} + \dfrac{\Delta T_{\text{driving}}}{\Delta T_{\text{lift}}}}{COP_{\text{Carnot}}\left(1 + \dfrac{2\Delta T_{\text{driving}}}{\Delta T_{\text{lift}}}\right)} \tag{2.16}$$

2.4.1.2 Vapor recompression cycles

The main difference between vapor compression and vapor recompression heat pumps is that the last mentioned has only one temperature driving force; usually on the high temperature side.

$$COP_{TDF} = \frac{T_h + \Delta T_{h,\text{driving}}}{\left(T_h + \Delta T_{h,\text{driving}}\right) - T_l} \tag{2.17}$$

With

$$\Delta T_{\text{driving}} = \Delta T_{h,\text{driving}} \tag{2.18}$$

Rewriting, simplifying and back-substituting the Carnot COP results in eq. (2.19)

$$\eta_{\text{Carnot}}^{TDF} = \frac{COP_{\text{Carnot}} + \dfrac{\Delta T_{\text{driving}}}{\Delta T_{\text{lift}}}}{COP_{\text{Carnot}}\left(1 + \dfrac{\Delta T_{\text{driving}}}{\Delta T_{\text{lift}}}\right)} \tag{2.19}$$

2.4.1.3 Compression-resorption cycles

In a similar fashion for the Lorentz efficiency,

$$COP_{TDF} = \frac{2T_h - \Delta T_{h,\text{glide}} + 2\Delta T_{h,\text{driving}}}{2T_h - \Delta T_{h,\text{glide}} + 2\Delta T_{h,\text{driving}} - 2T_l - \Delta T_{l,\text{glide}} + 2\Delta T_{l,\text{driving}}} \tag{2.20}$$

Again simplifying by assuming equal glide and driving forces for source and sink,

$$\eta_{\text{Lorentz}}^{TDF} = \frac{COP_{TDF}}{COP_{\text{Lorentz}}} = \frac{COP_{\text{Lorentz}} + \dfrac{2\Delta T_{\text{driving}}}{2\Delta T_{lift} - 2\Delta T_{\text{glide}}}}{COP_{\text{Lorentz}}\left(1 + \dfrac{4\Delta T_{\text{driving}}}{2\Delta T_{lift} - 2\Delta T_{\text{glide}}}\right)} \tag{2.21}$$

Notice that this equation reduces to the Carnot efficiency for $\Delta T_{\text{glide}} = 0$.

2.4.1.4 Absorption heat pump cycles

Performance of the absorption heat pump when temperature driving forces are considered is given by

$$COP_{ahp} = \left(\frac{T_{gen} - T_h - 2\Delta T_{\text{driving}}}{T_{gen} - \Delta T_{\text{driving}}}\right)\left(\frac{T_l - \Delta T_{\text{driving}}}{T_h - T_l + 2\Delta T_{\text{driving}}}\right) + 1 \tag{2.22}$$

The absorption heat pump is driven by heating the generator with high temperature heat. It is assumed that this heat is delivered by burning natural gas, which has an adiabatic flame temperature of
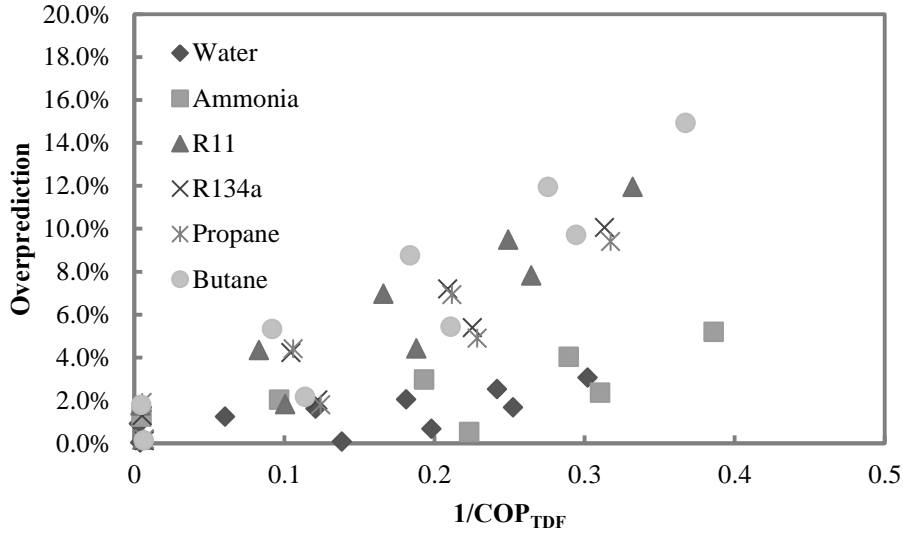
Fig. 2.6. Overprediction of COP by eq. (2.25) compared to simulated vapor compression heat pumps with the compressor operating under wet conditions with an isentropic efficiency of 0.7 and isenthalpic expansion for selected refrigerants. The data points have been obtained in the range 0.55 < T/T_{crit} < 0.75.

approximately 1950 °C. The thermal efficiency of cooling down the gas to the temperature of the generator is given by

$$\eta_{heating} = 1 - \frac{T_{gen}}{T_{ad}}$$

$$(2.23)$$

Then the total efficiency of an absorption heat pump is given by

$$COP_{ahp,\text{burner}} = \left(1 - \frac{T_{gen}}{T_{ad}}\right)\left[\left(\frac{T_{gen} - T_h - 2\Delta T_{\text{driving}}}{T_{gen} - \Delta T_{\text{driving}}}\right)\left(\frac{T_l - \Delta T_{\text{driving}}}{T_h - T_l + 2\Delta T_{\text{driving}}}\right) + 1\right]$$

$$(2.24)$$

2.4.2 Isentropic losses

Carnot COP assumes isentropic work. The efficiency of the system is linearly dependent on the efficiency of the compressor,

$$COP_{\text{non-isentropic}} = \frac{\dot{Q}}{\dot{W}},$$

$$(2.25)$$

$$\dot{W} = \frac{\dot{W}_{is}}{\eta_{is}} \rightarrow COP_{\text{non-isentropic}} = \frac{\eta_{is}\dot{Q}}{\dot{W}_{is}} = \eta_{is} COP_{TDF}$$

The accuracy of eq. (2.25) is compared against a simulated vapor compression cycle with the compressor operating under "wet" conditions (liquid-vapor mixture flowing into the compressor; saturated

conditions at the outlet) for different working fluids where the heat pump works in the range of 0.55 < T/T_{crit} < 0.75 for both evaporator and condenser. By moving the condenser temperature up to the critical point, eq. (2.25) can over predict the COP up to approximately 100%.

Fig. 2.6 illustrates the relative deviation of the COP from eq. (2.25) for a few real fluids. There is a clear distinction between refrigerants with simple molecular structure like water and ammonia, and more complex ones as propane, butane, R-11 and R-134a. This dependency on molecular structure was also indicated by Angelino and lnvernizzi [4] and McLinden [72].

2.5 Economic calculation

For the economic calculation, cost equations by Guthrie [34] have been used. In this section the equations by Guthrie have been modified to European conditions by changing to SI units and to euro as currency. Cost estimates have been made based on a Marshall & Swift (M&S) index of 1597.7 and a Dollar to Euro conversion rate of 0.81553 € / $ [113]. Prices of € 65 / MWh for electricity and € 31.65 / MWh for gas are suggested by the project partners. To illustrate the approach, an economic evaluation has been performed for a fixed highest sink temperature of 150 °C. The investment is determined at fixed sink temperature as the equipment has to be sized and temperature driving forces will be implemented as a function of lift, which in turn is taken relative to the sink temperature. Performance data were obtained in the same range as the economic evaluation has been made for, but the equations are valid for any given sink temperature.

The following assumptions apply

- Heat pump temperature driving forces 5 % of ΔT_{lift}, 10 % of ΔT_{lift}, and 25 % of ΔT_{lift}.
- Compressor isentropic efficiency 60-80 %
- Boiler efficiency η_H = 85 %
- Grid efficiency η_E = 43 %
- Dry compression
- Equal temperature glide, ΔT_{glide}, in hot and cold heat exchanger for CRHP
- Direct fired single effect absorption heat pump
- Internal heat exchanger of the absorption heat pump has 1.5 times the surface area of the absorber
- Shell and tube heat exchangers with U-tubes, design pressure is 27 bar. For absorption heat pumps and compression-resorption heat pumps stainless steel is chosen as construction material as it offers better resistance against corrosion when used with lithium bromide and water or ammonia/water mixtures. This includes the generator which is cylindrical and has a design pressure up to 34 bar. The other heat pump heat exchangers are built from carbon steel.
- Heat transfer coefficient for pure components and mixtures: 1200 W m^{-2} K^{-1}
- Electrical motor driven, centrifugal type gas compressor
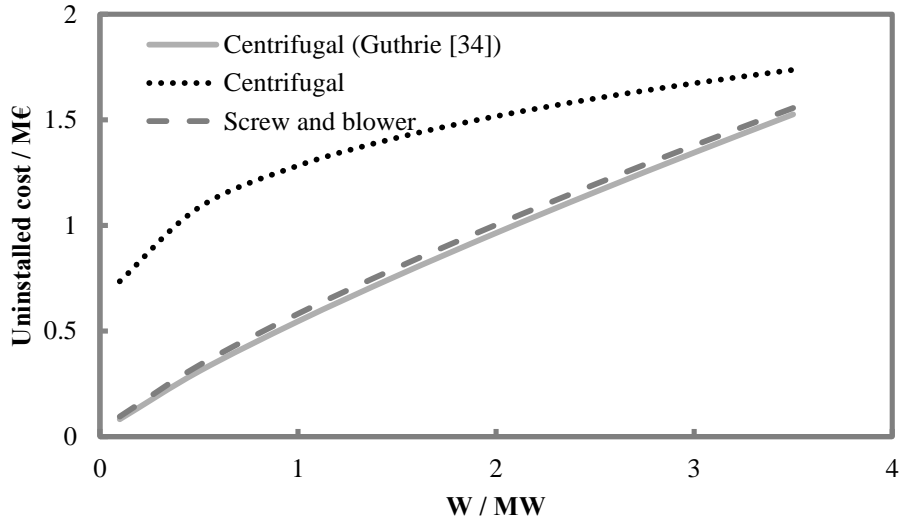- 8000 h/year of operation (92 % availability)

Fig. 2.7. Uninstalled compressor cost comparison between the model by Guthrie [34] and quotations where blowers are assumed to be similar to screw compressors. Compressor prices are set out against shaft power.

For a direct fired boiler the installed cost is given by

$$C_{\text{Installed,directfired boiler}} = 515.4 \dot{Q}^{0.85} \tag{2.26}$$

for heat loads in the range of 600 kW to 18 MW. For shell and tube heat exchangers built of carbon steel for the mechanical heat pumps,

$$C_{\text{Installed,CS shell\&tube heat exchanger}} = 7151.8 A^{0.65} \tag{2.27}$$

for surface areas between 20 and 500 m^2.

For shell and tube heat exchangers built of stainless steel for the absorption heat pumps,

$$C_{\text{Installed,SS shell\&tube heat exchanger}} = 10947.4 A^{0.65} \tag{2.28}$$

for the same size range as the carbon steel heat exchangers. It is expected that the range of validity can be extended with only a slight loss in accuracy.

Based on several quotations for process gas compressors correlations (2.29) and (2.30) were derived for the uninstalled cost of a compressor. The quotations include three different compressor types from four companies. The trend of the data is presented in Fig. 2.7 where they are compared against the equation proposed by Guthrie [34] with a current (M&S) equipment cost index. To go from uninstalled compressor cost to installed compressor cost, an installation factor of 2.11 as proposed by Guthrie [34] was chosen; thereby the installed cost of a compressor becomes 3.11 times the uninstalled cost. An updated equation can be proposed for the investment costs of large industrial compressors in the power range of

0.15 to 3.5 MW for 2012 in Western Europe. From the figure it can clearly be seen that the compressor cost obtained from different quotations is generally higher than predicted by Guthrie [34]. The difference is most significant in the smaller size range because the frame costs become relatively high in the smaller size range. It must be noted that selecting a vendor who uses a different construction might provide a lower cost alternative. However, the equation by Guthrie for predicting the cost of centrifugal compressors does predict the cost for a screw compressor quite accurately, see Fig. 2.7.

The cost for heat pump equipment has to be estimated without fluid property specification, therefore investment costs should not be a function of volume flow. Based on the power input required, the following equations for the uninstalled cost for screw and centrifugal compressors in the range between 0.15 and 3.5 MW are proposed:

$$C_{\text{screwcompressor/blower,uninstalled}}, \text{€} = 2517 \dot{W}^{0.7849} \tag{2.29}$$

$$C_{\text{centrifugal compressor,uninstalled}}, \text{€} = 2.417 \cdot 10^6 \dot{W}^{0.2416} \tag{2.30}$$

The value of the correlation coefficient is 0.9898 for the screw compressor cost and only 0.3645 for the centrifugal compressor cost. Due to the limited fit of Eq. (2.30) it is not recommended to use this equation outside the range of 150 kW to 2.9 MW for which the data are obtained. The data for Eq. (2.29) were obtained in the range from 150 kW to 3.5 MW. Eq. (2.29) has a similar power as proposed by Guthrie [34] corrected with the M&S equipment index. Fig. 2.7 shows that the equation follows the predicted cost for a centrifugal compressor as suggested by Guthrie. Therefore the authors expect that the range of this equation can be extended up to 7 MW.

It can be clearly seen that the cost of centrifugal compressors is not so strongly dependent on the compressor power as suggested by Guthrie [34], meaning larger installations benefit from relatively lower uninstalled compressor cost. The energy cost savings for mechanical and heat driven heat pumps are given by:

$$\text{savings per MWh for Mech HP} = \left(-\frac{C_{Gas}}{\eta_H} + \frac{C_E}{COP_{hp}} \right) \tag{2.31}$$

$$\text{savings per MWh for Heat driven HP} = \left(-\frac{C_{Gas}}{\eta_H} + \frac{C_{Gas}}{COP_{ahp}} \right) \tag{2.32}$$

The amount that can be invested per kW heating duty can be determined by selecting a simple pay-back time. The possible investment per kW heat duty increases rapidly with increasing COP up to a COP of 5. Increasing the COP further (by a factor of 4) only increases the possible investment by less than 40 %, as is shown in Fig. 2.8a. Comparing against the possible investment cost per kW of installed compressor power, the increase is almost linear, even at high COP. This is shown in Fig. 2.8b.
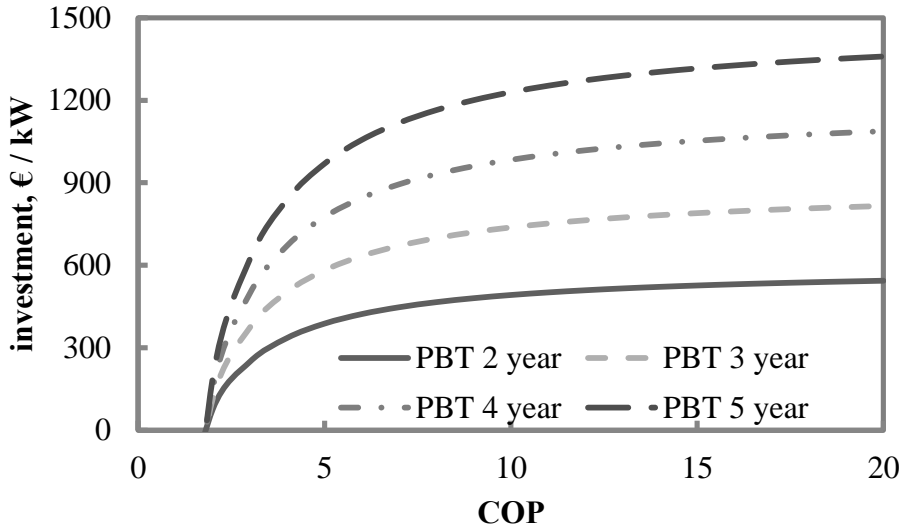
(a)
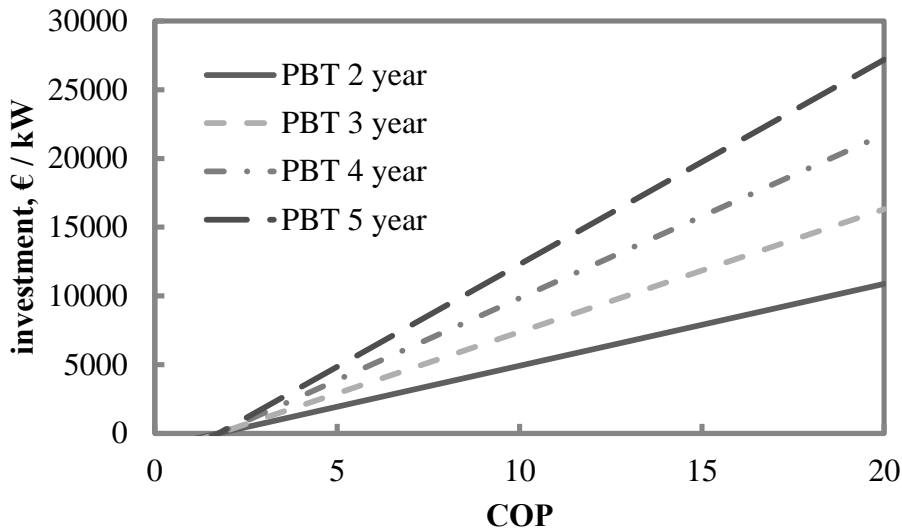
(b)

Fig. 2.8. (a). Maximum possible investment for mechanical heat pumps per kW of heating power as a function of COP. Payback time is shown as a parameter (b). Maximum possible investment for mechanical heat pumps per kW of compressor power as function of COP. Payback time is shown as a parameter.

In Fig. 2.9 the payback times for heat pumps for small and medium sized distillation columns with heat loads of 2.8 MW and 10 MW are presented as a function of lift-to-sink temperature ratio and available temperature glide. For instance CRHP-50 % glide indicates that on both reboiler and condenser there is a temperature difference between in- and outlet of 50 % of the ΔT_{lift} as defined in eq. (2.7). Fig. 2.10 also gives values for payback periods; however, compared to Fig. 2.9, details such as temperature driving

(a)

VCHP   **CRHP-25% glide**   **CRHP-50% glide**

CRHP-75% glide   **CRHP-95% glide**   **AHP-10% TDF**
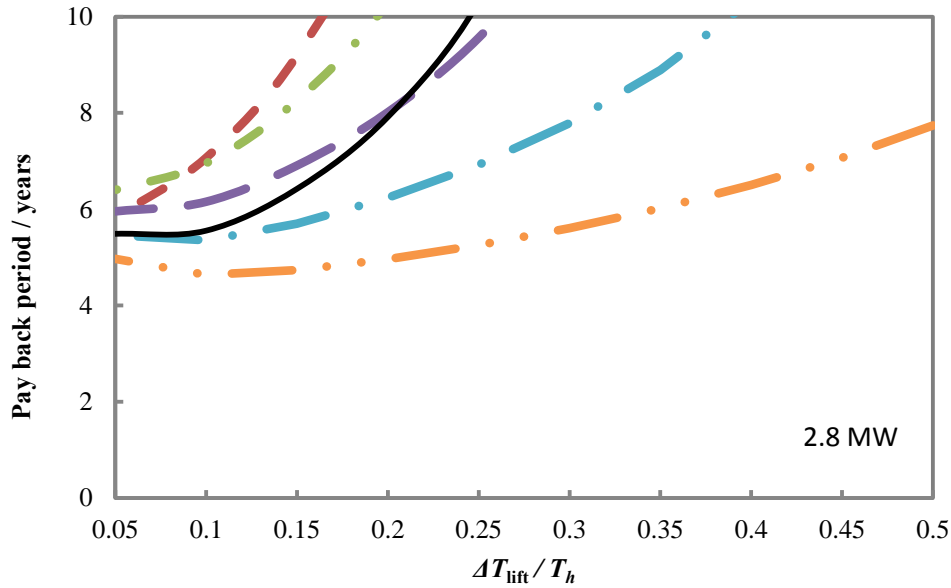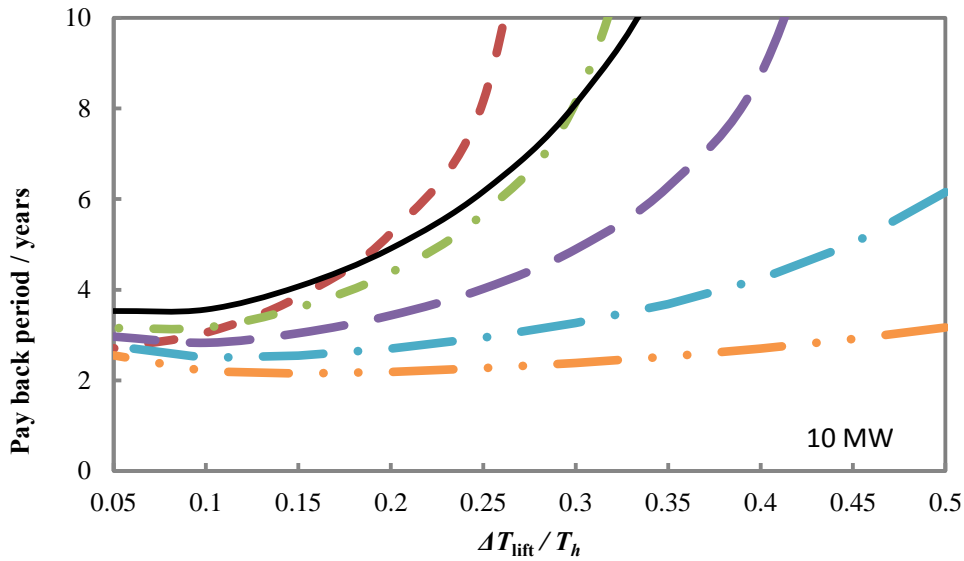
(b)

Fig. 2.9. Payback period as function of dimensionless lift for different heat pump systems. The influence of temperature glide as percentage of the lift is clearly demonstrated. Isentropic compressor efficiency is 70% and temperature driving forces are 10% of the temperature lift. The effect of size is clearly demonstrated by comparing (a, $\dot{Q}$=2.8 MW) and (b, $\dot{Q}$ =10 MW). In some cases, heat pumps with a glide of 50% can achieve about 50% higher lifts compared to a similar vapor compression system when keeping the payback period constant.
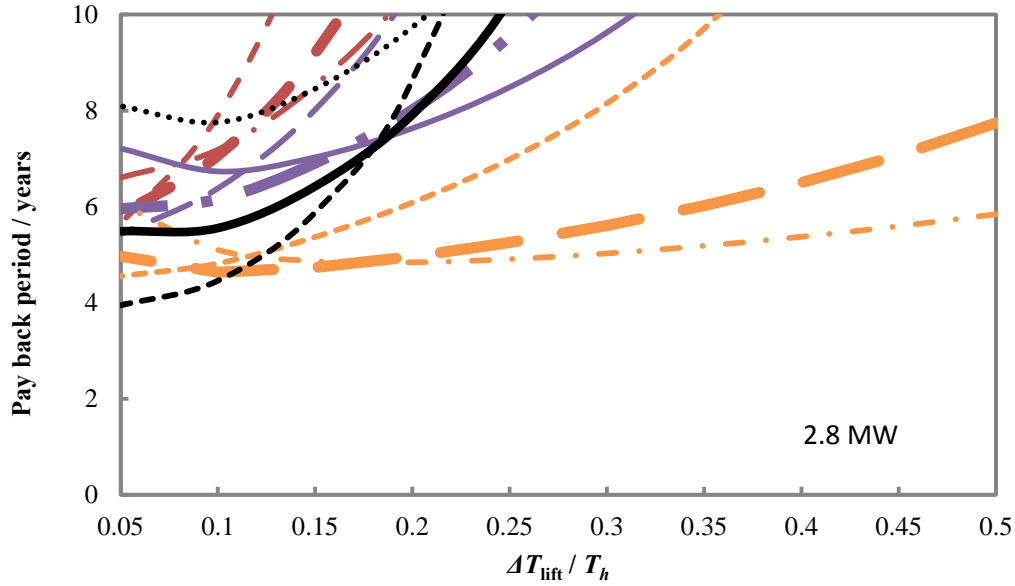
(a)
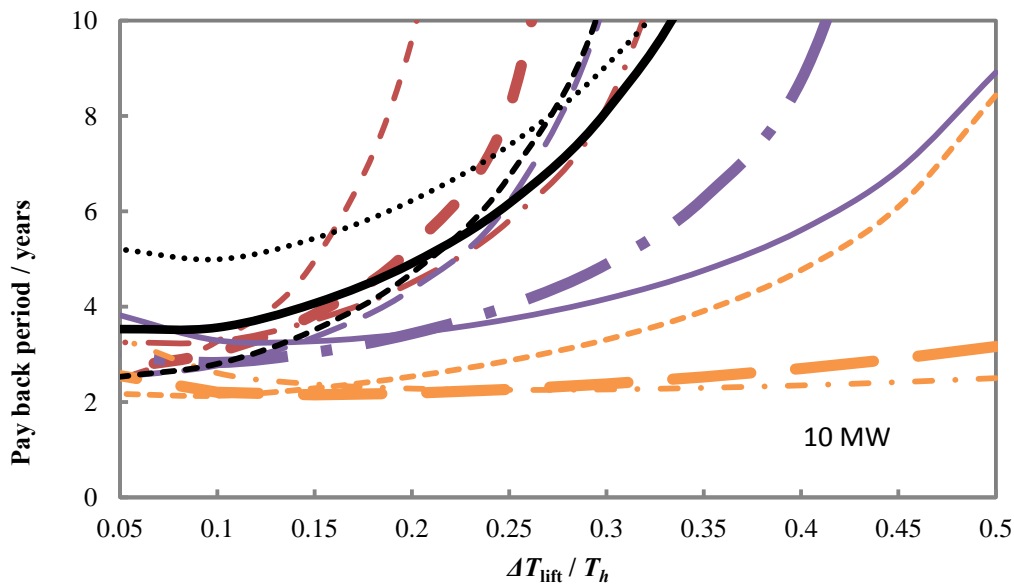
(b)

Fig. 2.10. Payback period as function of dimensionless lift for different heat pump systems. The bandwidth included by adding 60% isentropic compressor efficiency with 20% temperature driving force and 80% isentropic compressor efficiency with 5% temperature driving force cases to Fig. 2.9. On the x-axis the ratio between temperature lift and sink temperature for the process fluid can be found, on the y-axis the simple payback time. The effect of size is clearly demonstrated by comparing (a, $\dot{Q}$=2.8 MW) and (b, $\dot{Q}$=10 MW).
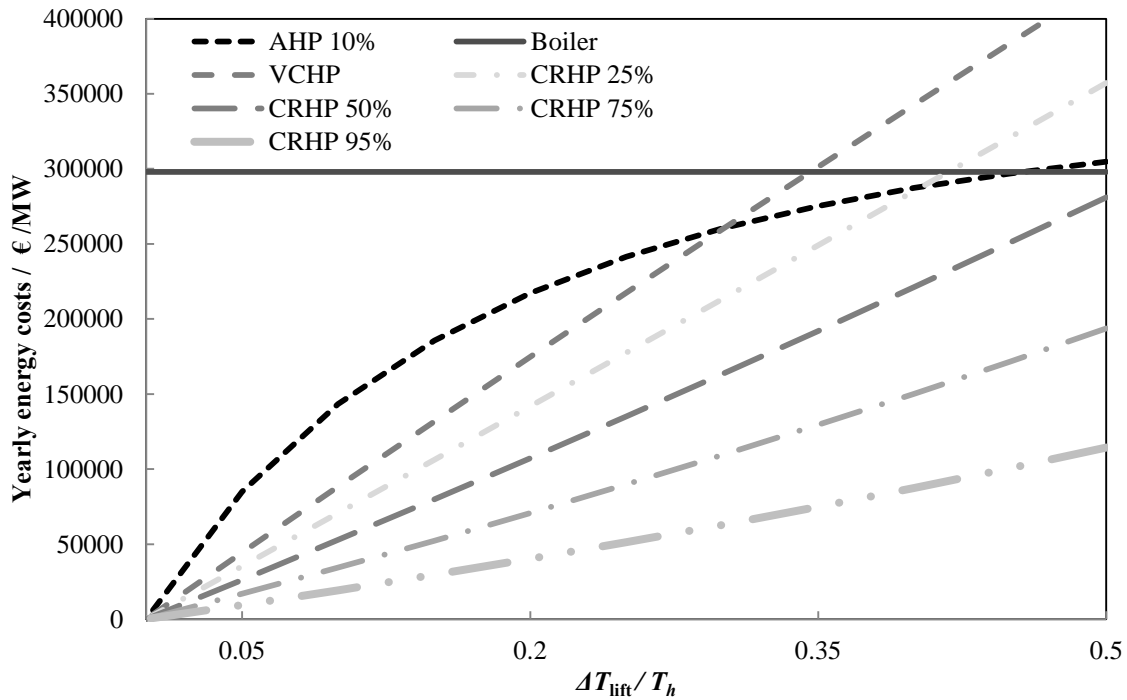
Fig. 2.11. Annual energy costs per MW boiler capacity as function of dimensionless lift for different heat pump systems. An isentropic compressor efficiency of 70% and temperature driving forces equal to 10% of the temperature lift have been assumed. Four compression-resorption heat pumps with glide-to-lift ratios of 25, 50, 75 and 95% have been included. The energy costs are based on 8000 operating hours per year.

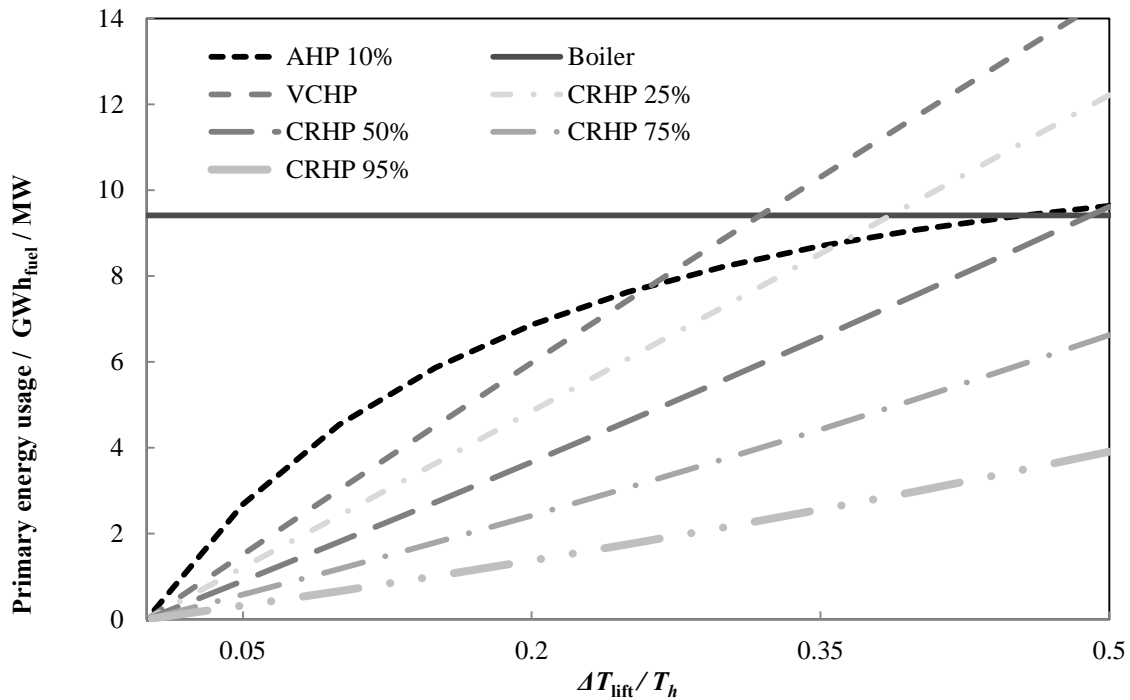**Fig. 2.12. Primary energy usage as function of dimensionless lift for different heat pump systems. An isentropic compressor efficiency of 70% and temperature driving forces equal to 10% of the temperature lift have been assumed. Four compression-resorption heat pumps with glide-to-lift ratios of 25, 50, 75 and 95% have been included. The energy used is based on 8000 operating hours per year.**

forces and compressor isentropic efficiency are now included to determine the approximate bandwidth for such systems. For instance AHP-5% TDF indicates that the temperature driving force is 5 % of ΔT_{lift} as defined in eq. (2.7). CHRP 50% 60% - 20% TDF indicates a compression resorption heat pump with a temperature glide equal to 50% of the temperature lift, 60% isentropic compressor efficiency and driving forces 20% of the temperature lift.

Fig. 2.11 shows the operating (energy) costs for different systems as function of lift-to-sink temperature ratio. To determine the cost-effectiveness of applying a heat pump to a certain process, the dimensionless lift-to-sink temperature ratio should be determined as well as the available glide in the process divided by the temperature lift of the process. The dimensionless lift-to-sink temperature ratio and available temperature glide should then be plotted in Fig. 2.9 and Fig. 2.10 to obtain the payback period. To obtain the energy costs savings for heat pumps with temperature driving forces of 10% of the lift and an isentropic efficiency of 70% for the compressor Fig. 2.11 should be applied. Fig. 2.12 can be used to compare the primary energy usage for the different systems. These two figures show a similar shape as the ratio between the boiler efficiency and the grid efficiency is similar to the ratio between electricity price and gas price.

From Fig. 2.9 it can be concluded that having a temperature glide available is advantageous for lift-to-sink temperature ratios of more than 0.1 for both small and large installations. Fig. 2.10 illustrates that high temperature driving forces have a large impact for low temperature lifts as this keeps the cost for heat exchangers low. This can be seen most clearly on the far left of the figure. Although an inefficient compressor, resulting in high compressor power and thus larger investment cost for the compressor, is used, the high temperature driving forces keep the size of the heat exchangers small and therefore the total investment cost low.

The vapor recompression heat pump is best applied in low temperature lift applications, as here the relative advantage of having only one temperature driving force compared to the two temperature driving forces in the vapor compression heat pump is the largest. In vapor compression heat pumps the refrigerant can be chosen in such a way that the vapor density at compressor inlet and the latent heat are large, therefore the required compressor size can be smaller and thus have lower cost. As the compressor in the vapor recompression heat pump is larger and more expensive, to come to an acceptable payback period the performance has to be significantly higher in terms of lower energy use.

At very low temperature lifts, the compression-resorption heat pump system can have an advantage over the vapor recompression heat pump as long as the temperature glide over both heat exchangers is larger than the temperature driving force of one of the heat exchangers. However, here the compression-resorption heat pump is also competing with the HIDiC, which has a glide over the heat exchanger as well. On the other hand, heat pumps like HIDiC have a temperature glide in such a way that the isobars are not close to being parallel, as opposed to compression resorption heat pumps. As a consequence, in practice, the HIDiC will have larger losses due to temperature driving forces. In wide boiling mixtures (high temperature lifts), where this non-parallelism is more pronounced, it might be better to apply a compression-resorption heat pump. Transcritical heat pumps are not yet preferred as these heat pumps do not match most industrial process conditions. Most research on transcritical heat

pumps is on CO_2 as refrigerant, but a different fluid with higher possible evaporation temperature is required for industrial applications. Under the assumption that such a fluid is identified, the best use may be there where the feed to a column is relatively pure already, but needs to be further separated. In such a column, the temperature glide above the feed is small compared to the available glide below the feed.

Comparing the heat pump systems with mechanical compressor against heat driven heat pumps like absorption heat pumps, it can be seen that absorption heat pumps are less sensitive to temperature lifts. While at lower temperature lifts, compressor driven heat pumps have the advantage, for larger temperature lifts the opposite is true. Heat driven heat pumps are advantageous compared to conventional boilers until lift-to-sink ratios of ca. 0.4.

The equations proposed in this work can be used to predict the technical heat pump performance for condensation temperatures far away from the critical point of the refrigerant. The equations for Lorentz cycles can be applied to compression-resorption heat pumps using ammonia/water mixtures. Predictions can be refined by including fluid specific information as well as pressure and mismatch losses. Pressure losses can be designed for and mismatch losses can be mainly avoided by selecting proper refrigerants and refrigerant mixture concentrations. Using the cost equations proposed in this work a rough estimate of the investment cost for compressors and heat exchangers can be made. Volume flow rates, operating pressures and heat transfer properties should be included to predict investment and payback time more accurately, but this requires knowledge about the heat pump fluid to be used, as well as more and more accurate cost data.

Although the model is able to predict performance and cost to a certain extent, it assumes the heat pump is technically possible. The technical feasibility should always be verified. A similar heat transfer coefficient has been assumed for both pure components and mixtures. It can be expected that mixtures have lower heat transfer performance compared to pure refrigerants [91], requiring larger heat exchangers.

2.6 Conclusions

In this chapter an approach to predict the economic performance of different types of heat pumps has been introduced. Efficiencies were used in combination with simple equations to determine the investment cost and cost savings to create a heat pump selection map. The proposed heat pump selection map should be used as follows:

1. Determine the lift-to-sink temperature ratio for the process fluids
2. Check for the available temperature glide and divide it over the lift
3. Put these data in Fig. 2.9, Fig. 2.11 and Fig. 2.12 to determine the possible economic performance of the different heat pump configurations.

New equations have been proposed for the uninstalled compressor cost on the western European market, showing that centrifugal compressors are relatively cost-insensitive to size in terms of power,

while screw compressors and blowers are more sensitive but offer a lower cost solution for smaller size installations. For this reason, small sized installations with a thermal duty of 5 MW or lower could best be built around a blower or screw compressor. Heat pumps with a temperature glide of 50% of the lift can in some cases offer about 50% higher lift at the same payback period in both small and large size ranges. Heat driven heat pumps are especially competitive in smaller sized installations as well as in applications with high temperature lifts as long as relatively large temperature driving forces are selected.

3 ON THE OPTIMAL PERFORMANCE OF COMPRESSION RESORPTION HEAT PUMP SYSTEMS

A short payback time is required by the chemical process industry for any investments in energy efficient systems, such as heat pumps to compete with alternative investments. Consequently, the operating conditions for implementing compression-resorption heat pumps should be chosen such that the energetic performance is maximal at minimum investment costs. Basically, this should result in a small compressor power, which has a double benefit: low investment in the compressor (one of the main components) and reduced operating costs – therefore also shorter payback times.

The performance of compression-resorption heat pumps has been numerically investigated for 50 specific industrial cases, by using an equilibrium model for a compression-resorption heat pump (CRHP) with ammonia-water as working fluid. The average concentration of ammonia was varied, while the temperature driving forces between process and heat pump, at the heat exchanger inlets and outlets were kept constant. Temperature lifts up to 124 K can be attained with both economic and energetic advantages. The results for the efficiency of the heat pumps obtained from this numerical investigation are compared against the model reported in chapter 2 that uses the Carnot efficiency as starting point to estimate the performance under similar assumptions.

The results of the simulation show that optimal performance is obtained when the ammonia concentration is chosen such that vapor quality is exactly 100% at the inlet of the resorber. This leads to the lowest compressor power, and consequently to reduced investment and operating costs – resulting in shorter payback times as well as more efficient use of resources, and ultimately to increased industrial acceptance of compression-resorption heat pumps.

This chapter is for a large part based on:

3.1 Introduction

In spite of its many well-known benefits and the widespread use, distillation has one major drawback – namely the large energy requirements, since distillation can generate half of the operating costs of a plant. Distillation has a low exergetic efficiency (e.g. about 12% for crude distillation), requiring the input of high quality energy in the reboiler while rejecting a similar amount of heat in the condenser, at lower temperature. Heat pump (HP) systems can be used to upgrade the low quality energy in the condenser in order to drive the reboiler of the column and thus reduce the consumption of valuable utilities.

Neelis et al. [78] made an inventory of 68 key processes in the petrochemical industry and investigated their energy use in relation to the thermodynamic requirements of the processes. Most processes appear to have very low exergetic efficiency, since distillation was used as the separation method of choice in nearly all of these processes. As discussed by Kiss et al. [56], an effective method to improve the efficiency of distillation processes is by making use of heat pumps to upgrade the condenser heat to reboiler temperature level. In chapter 2 a simplified method was described to predict the payback time of several heat pump types if applied to specific distillation processes.

Tufano [104] has investigated the potential energy savings in distillation processes by the integration of absorption heat upgrading systems of different configurations. Tufano [104] concluded that the heat load of the absorption cycle should match with the heat loads of the distillation column to minimize the consumption of primary energy. Sabir and Eames [89] have theoretically compared absorption and resorption cycles and concluded that the resorption cycle is more efficient than the absorption cycle. Moreover, Bourouis et al. [9] investigated the use of a compression-resorption cycle to upgrade thermal waste heat from 80 to 120°C. A pressure ratio was identified, for which the operation of the cycle was most efficient.

The integration of heat pumps with distillation columns has been recently discussed by Dièz et al. [22], who investigated the potential energy savings by coupling models of several heat pump types to distillation process data of close boiling mixtures. According to Hewitt et al. [39] short payback times can be achieved by increasing the performance of heat pumps. In order to increase the heat pump performance in high temperature lift cases, they suggested applying a compression-resorption heat pump operating with an ammonia-water mixture. Chan et al. [13] give an overview of thermodynamic cycles for low grade heat utilization including ammonia-water absorption systems, while Keil et al. [52] report about the upgrading of waste heat from 40°C to 82°C by making use of an absorption heat pump.

This brief literature review shows that compression-resorption heat pumps can be applied to distillation columns with high temperature lifts. Typically, the temperature of distillation columns is low at the top and increases towards the lower sections, reaching a maximum in the reboiler. In contrast to conventional types of heat pump systems, the compression-resorption heat pump (CRHP) can use this temperature glide to its advantage, effectively reducing the average temperature lift and thereby increasing the performance of the heat pump. Fig. 3.1 conveniently illustrates this integration between a distillation column and a heat pump, for the case when a CRHP is applied.
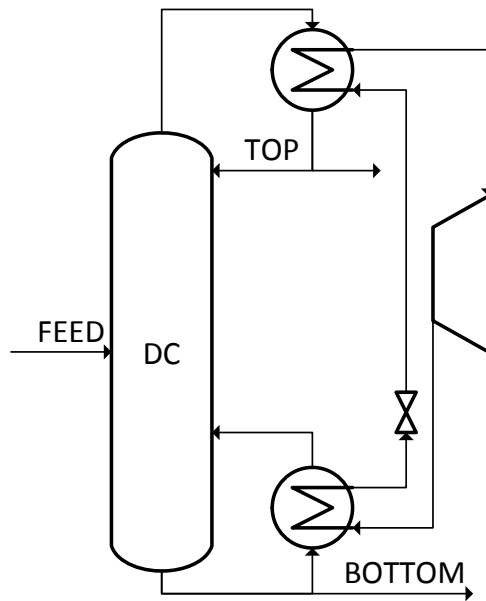
Fig. 3.1. Integration of compression-resorption heat pump (CRHP) with the condenser (desorber) and reboiler (resorber) of a distillation column [56].

The operating conditions of a CRHP should be chosen such that the energetic performance is maximal while the investment costs are minimal. Compared to vapor compression heat pumps working with pure working fluids, the CRHP has an additional degree of freedom to optimize: the concentration of the working fluid. Optimizing the concentration of the working fluid should result in a small compressor power, thus providing a double benefit: low investment in the compressor (one of the main components) as well as reduced operating costs.

In this chapter a large number of frequently used industrial distillation processes (50 distillation columns from the Dutch industry – data provided courtesy of ECN) is investigated where the condenser and reboiler are integrated with a compression resorption cycle, which matches as close as possible the process glides in the condenser and reboiler. Fig. 3.2 presents how the operating conditions of these columns are related to the temperature lift and glides in the condenser and reboiler of the columns. Electrically driven heat pumps start to deliver an economic and energetic advantage in comparison to conventional reboilers when the COP is larger than 2.0, see chapter 2. A dedicated thermodynamic model was used to investigate the cycle performance when the average concentration of ammonia in the ammonia-water solution is varied from 0 to 100%.

The driving force is assumed to be 5 K at both resorber outlet and desorber inlet, while the vapor quality at the resorber inlet is varied. If the temperature driving force at the resorber inlet is lower than the required 5 K, the result is not included. In addition, the temperature profile in the desorber is determined. By investigating the 50 different industrial cases, the cases with economic and/or energetic advantage when a compression-resorption heat pump is used are identified. Further it is shown that the best overall performance for these cycles is obtained when the vapor quality at the resorber inlet is approximately 100%. This significantly simplifies the thermodynamic modeling and the optimization of compression-resorption heat pump systems integrated with distillation columns.
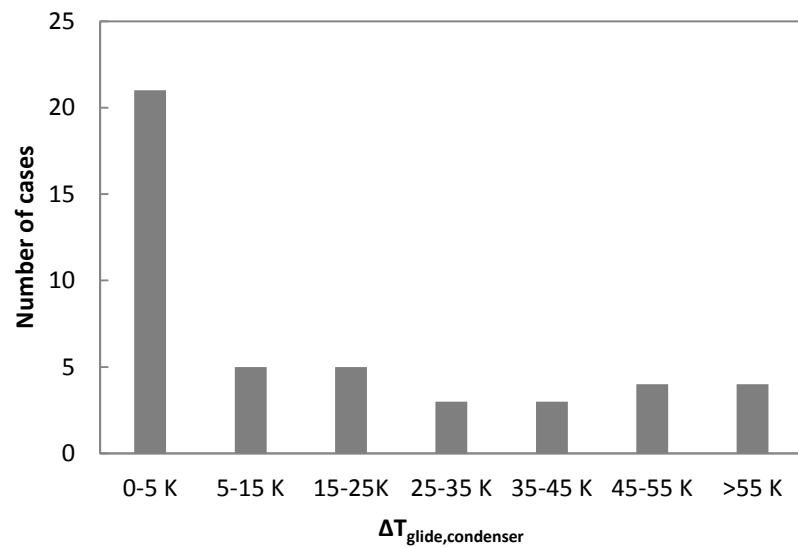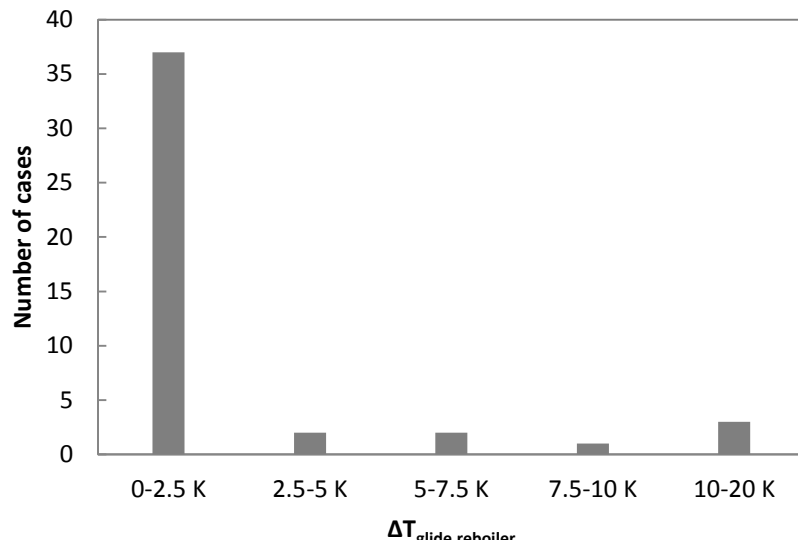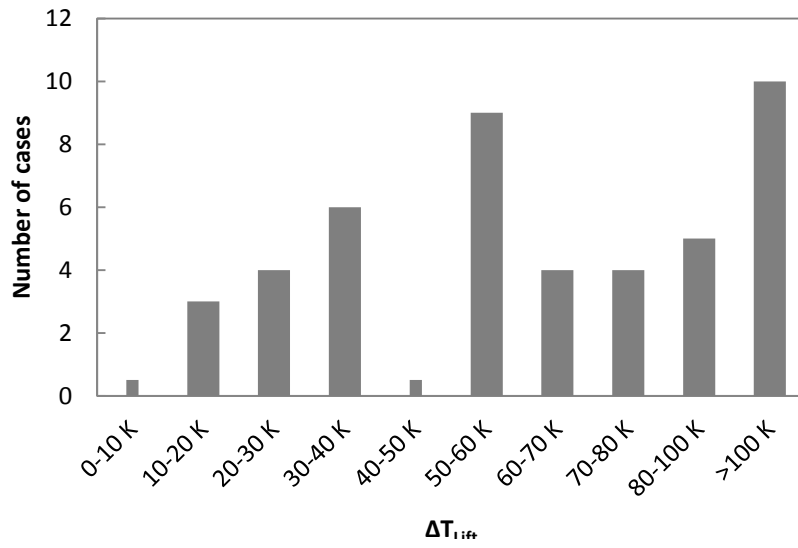
Fig. 3.2. Operating conditions of the columns. Temperature lift, reboiler and condenser glide distribution for the 50 cases. Five cases showing convergence problems with the fluid library have been left out. Most of the cases have a low glide in the reboiler.
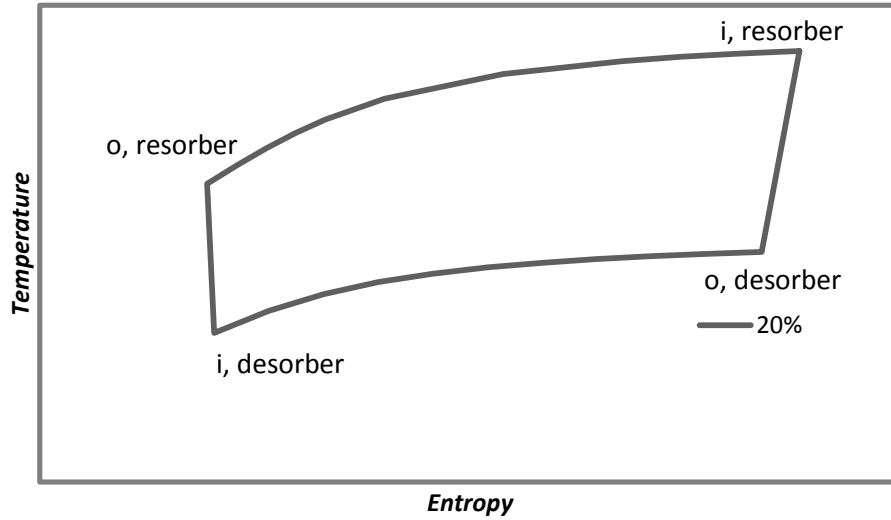
(a)
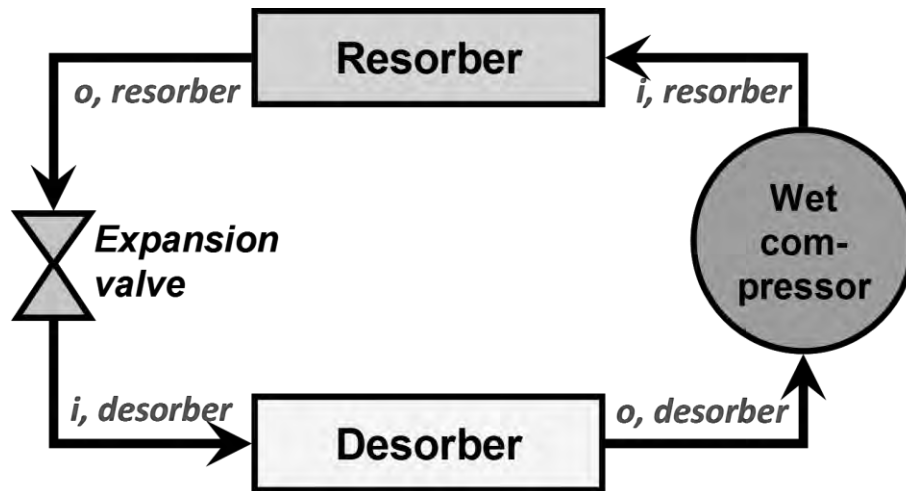
(b)

Fig. 3.3. Example of an ideal compression-resorption heat pump cycle in a temperature-entropy diagram including subscript definitions - the ammonia concentration used in this example is 20% (a). Scheme of a compression-resorption heat pump, with the compressor operating in the wet regime (b).

3.2   Mathematical model

A steady state thermodynamic process model assuming equilibrium states was developed for the compression-resorption heat pump in order to obtain an accurate estimate of the performance of such heat pumps under given conditions. NIST RefProp (Reference Fluid Thermodynamic and Transport Properties Database) v8 [61], with equations proposed by Tilner-Roth and Friend [102], was used as library for calculating thermodynamic properties of the ammonia-water mixture. Fig. 3.3 shows the compression resorption heat pump cycle for this binary mixture.

3.2.1 Model assumptions

The following assumptions have been made:

- Resorber outlet temperature is 5 K higher than process temperature
- Either desorber inlet temperature is 5 K lower than process outlet temperature and > 5 K lower than process inlet temperature, or vice versa
- No significant pressure loss in both heat exchangers
- Isentropic efficiency of the compressor is 70%
- Electric drive efficiency is 100%
- No heat loss to the surroundings

The vapor quality (q) at the inlet of the resorber was varied over the range of 10-100% with steps of 1%. The ammonia concentration (x) was varied from 0.5 to 99.5% in steps of 0.5%. The step size in ammonia concentration was reduced to 0.01% or even 0.001% in case of low temperature glides in the process, because here the temperature glide in the heat exchangers is very sensitive to the ammonia concentration.

3.2.2 Model equations

Starting with the resorber outlet (assumed to be a saturated liquid) temperature, the resorber pressure and resorber inlet conditions are determined as follows:

$$P_{\text{resorber}} = f(T_{\text{resorber},o}, q = 0, x) \tag{3.1}$$

$$T_{\text{resorber}} = f(P_{\text{resorber}}, q_{\text{resorber},i}, x) \tag{3.2}$$

$$h_{\text{resorber}} = f(P_{\text{resorber}}, q_{\text{resorber},i}, x) \tag{3.3}$$

The process in the expansion valve is modeled as an isenthalpic flash (i.e. no changes in enthalpy). The outlet enthalpy of the resorber is given by:

$$h_{\text{resorber},o} = f(T_{\text{resorber}}, q = 0, x) \tag{3.4}$$

Thus the inlet enthalpy of the desorber equals:

$$h_{\text{desorber},i} = h_{\text{resorber},o} \tag{3.5}$$

From this point further, two calculation procedures can be followed. The first procedure is chosen when the available temperature glide at the process side of the resorber is larger than the available glide in the process side of the desorber. The pressure at the desorber inlet is obtained, and then the enthalpy at the desorber outlet is determined as function of pressure and entropy. The second procedure is used when the available glide for the desorber is larger, determining the desorber pressure as function of desorber outlet temperature and entropy. In both cases the entropy is iterated to obtain the correct conditions for the compressor.

Following the first procedure, the operating pressure of the desorber is given by:

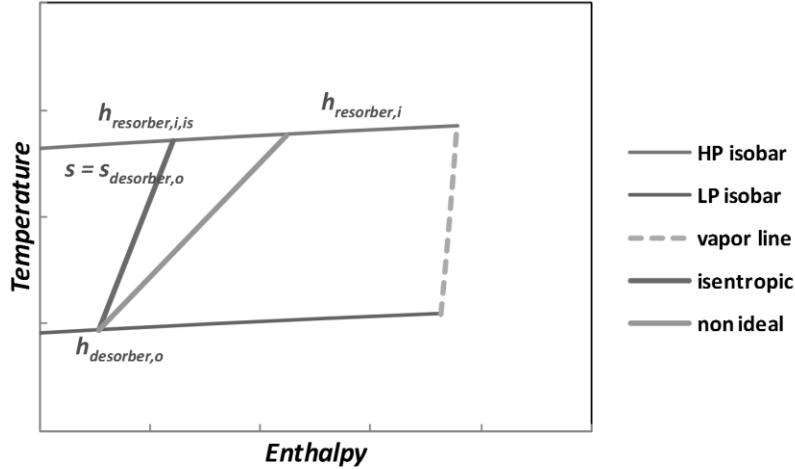$$P_{desorber} = f(T_{desorber,i}, h_{desorber}, x) \tag{3.6}$$

Fig. 3.4. Calculation method for desorber outlet enthalpy. An initial value for the entropy at the desorber outlet is chosen. In the first procedure, the enthalpy is calculated based on the desorber pressure and entropy at the outlet. In the second procedure, the enthalpy is calculated based on the desorber temperature and entropy at the outlet. Assuming an isentropic process, the resorber inlet enthalpy is determined. The value is corrected for isentropic efficiency to determine the resorber inlet enthalpy. The value of the enthalpy at resorber inlet should match the value determined based on the desired vapor quality at the inlet of the resorber. If this is not the case, the enthalpy value at the desorber outlet has to be iterated.

where $T_{desorber,i}$ is taken 5 K lower than the process outlet condition. The conditions at the compressor outlet for the theoretical case of 100% isentropic efficiency should be on the same entropy line as the inlet condition. This is used as a start condition in order to determine the conditions at the desorber outlet.

$$h_{desorber,o,init} = f(P_{desorber}, s_{desorber,o,init}, x) \qquad (3.7)$$

Iterations are carried out until the values for the isentropic enthalpy obtained from the two following calculations are converged:

$$h_{desorber,o} = \frac{h_{resorber,i,is} - \eta_{is} \cdot h_{resorber,i}}{1 - \eta_{is}} \qquad (3.8)$$

$$h_{desorber,o} = f(P_{desorber}, s_{desorber}, x) \qquad (3.9)$$

Fig. 3.4 conveniently illustrates this procedure. Following the iterations, the temperature at the outlet of the desorber can now be obtained:

$$T_{desorber,o} = f(P_{desorber}, h_{desorber,o}, x) \qquad (3.10)$$

In case that this temperature is higher than the process temperature minus the required temperature driving force, the corresponding concentration could be discarded. Alternatively, the temperature driving force at the inlet of the desorber should be increased.
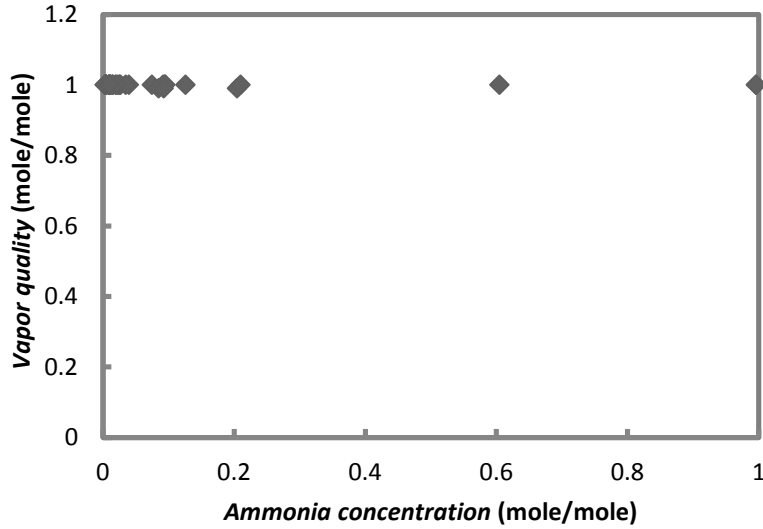
Fig.3.5. Vapor quality at the inlet of the resorber as function of optimal ammonia concentration. Highest efficiency is always attained at 100% vapor quality at the resorber inlet.

The second procedure is selected as optimal calculation procedure if the available process side glide in the desorber is larger than in the resorber. The procedure starts by taking the temperature at the outlet of the desorber equal to the process temperature minus the driving force and by assuming a value for the entropy at the desorber outlet. The entropy is related to the entropy at the resorber inlet as in the ideal case work is isentropic.

$$h_{desorber,o,init} = f\left(T_{desorber,o},\ s_{desorber,o,init},\ x\right)$$ **(3.11)**

The entropy is iterated until the same values are obtained for enthalpy at the desorber outlet condition for eqs. (3.8) and (3.11). The desorber pressure and outlet enthalpy are obtained from:

$$h_{desorber,o} = f\left(T_{desorber,o},\ s_{desorber,o},\ x\right)$$ **(3.12)**

$$P_{desorber} = f\left(T_{desorber,o},\ s_{desorber,o},\ x\right)$$ **(3.13)**

This procedure is also illustrated in Fig. 3.4. The temperature at the inlet of the desorber can now be determined as a function of pressure and enthalpy at inlet conditions.

$$T_{desorber,i} = f\left(P_{desorber},\ h_{desorber,i},\ x\right)$$ **(3.14)**

As described previously, the choice for the final calculation procedure depends on the available glide in the process side of the resorber and desorber.
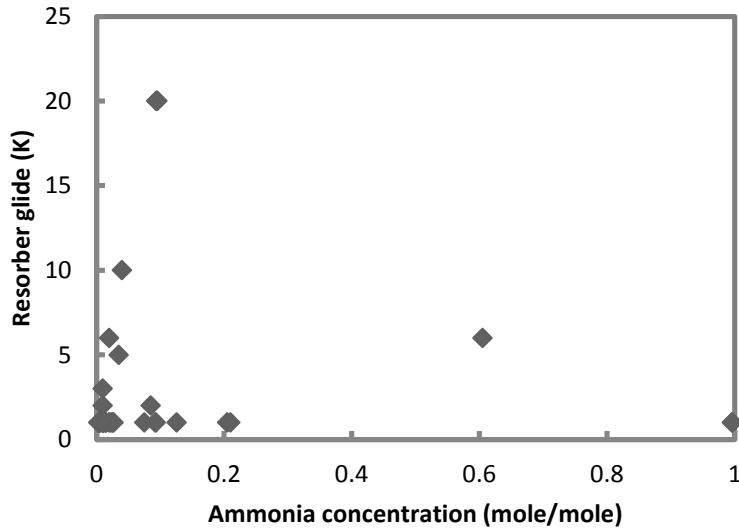
(a)
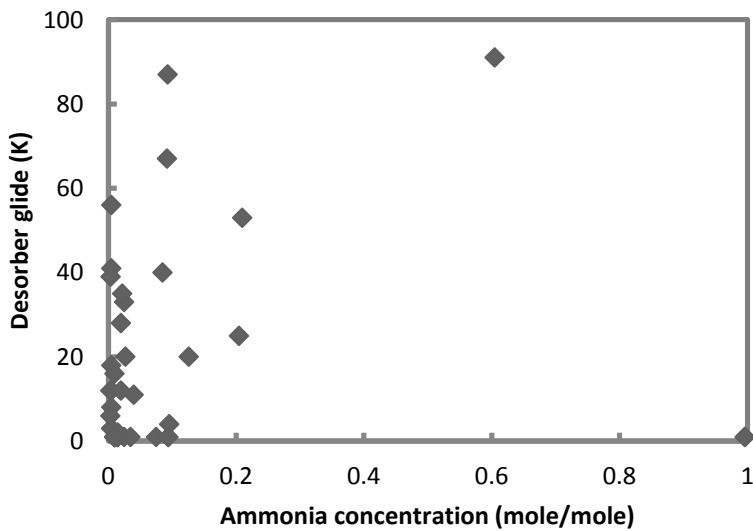
(b)

Fig.3.6. Available resorber glide for the cases under investigation and ammonia concentration for optimal performance (a). Available desorber glide for the cases under investigation and ammonia concentration for optimal performance (b).

3.2.3 Simulation results

The results of the simulations were obtained at step sizes of 0.005 mole / mole for the ammonia concentration (x), and the vapor quality (q) step size was set to 0.01 mole / mole. Minimum vapor quality at the resorber inlet was set to 0.1 mole / mole. The convergence criterion was initially set to 0.1% difference in the energy balance between compressor power, and resorber and desorber heat duties. For cases close to the critical point of the mixture, this had to be revised and set to a higher value (3%) in order to allow for calculation convergence. The isentropic efficiency used in eq. (3.8) has been taken as 0.70 for all cases.
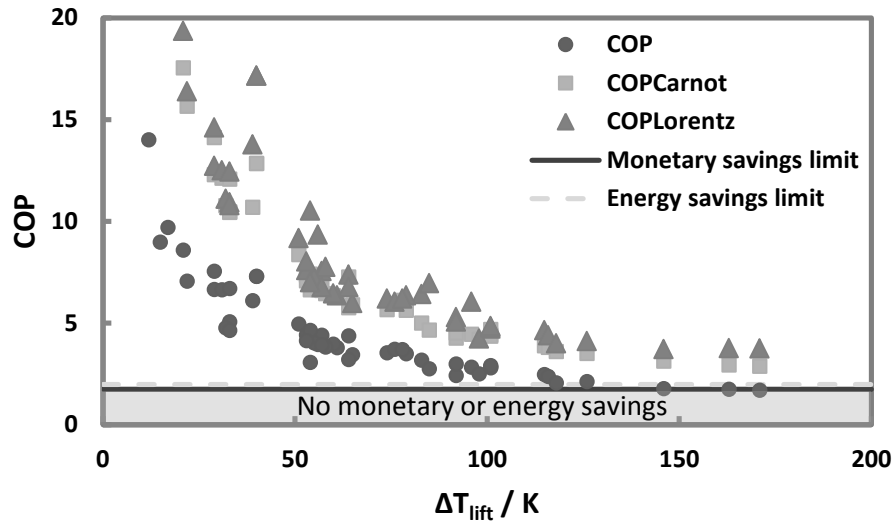
(a)
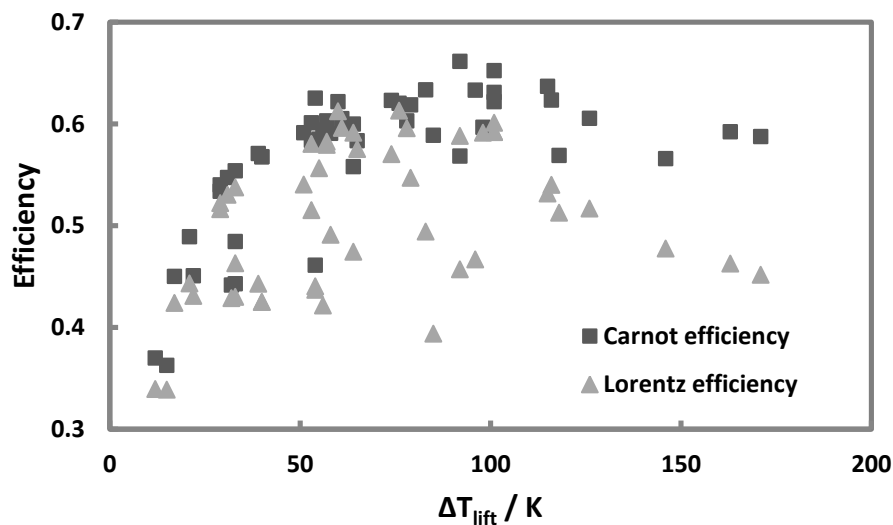
(b)

Fig.3.7. COP, Carnot COP, Lorentz COP (left) as well as Carnot and Lorentz efficiency (right) as function of lift. The COP drops with increasing temperature lift, while the Carnot and Lorentz efficiencies are typically low for low-lift cases which might be attributed to temperature driving forces being relatively large at low temperature lifts. Monetary savings are possible for all cases above the black solid line (up to a temperature lift of 145 K), while energy savings are possible for all presented cases which are above the gray, dashed line directly above the black solid line (up to a temperature lift of 124 K).No energy or monetary savings are possible in the gray area below these lines.

In five cases the fluid property library used to calculate the properties of the water-ammonia mixture failed to converge. These cases have been left out of the figures. Fig.3.5 shows the optimal vapor quality at the resorber inlet, while Fig.3.6 presents the optimal ammonia concentration dependent on the range of glides in the resorber and desorber for the 50 industrial cases considered.
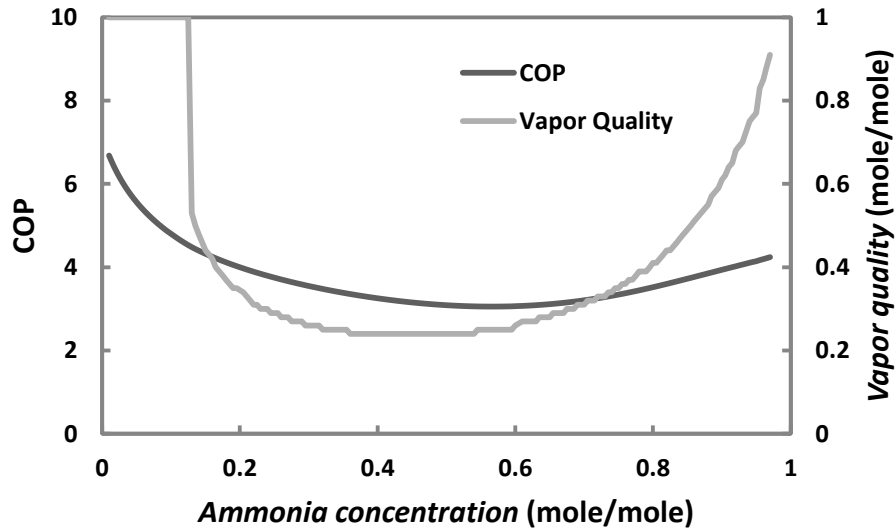
Fig.3.8. COP and vapor quality as function of ammonia concentration for one of the investigated cases. For this specific case the temperature lift is 33 K and the temperature glide in both the condenser and the reboiler is 1 K.

From Fig.3.5 it is clear that a vapor quality of 1.0 at the resorber inlet gives the best performance for all the operating conditions considered. To adjust the glide of the ammonia water mixture to the column temperature profile the ammonia concentration has to be optimized. Fig.3.6 illustrates that for most cases the optimal ammonia concentration is in the range 0-0.20 or 0.95-1.00. Fig.3.7 shows the results of the current model for COP, as well as the Carnot and Lorentz COP for the distillation columns as function of the difference between highest and lowest temperature of the process (ΔT_{lift}). The efficiency calculated by the model – compared to the Carnot and Lorentz COP – is also presented in Fig.3.7. For the economic and energy savings limits, the data proposed in chapter 2 have been used. Only for the cases with extremely high temperature lifts (>150 K) conventional reboilers perform better.

Fig.3.8 illustrates the obtained results for a specific case in which the temperature lift is 33 K and the temperature glide in both the condenser and reboiler is 1 K. COP and vapor quality at the resorber inlet are presented as a function of the selected ammonia-water concentration. In Fig.3.9 the results for the optimized COP of the current model are compared with the results of the model discussed in chapter 2.

As temperature glide, the smallest available glide in either desorber or resorber was chosen as input for the glide in both heat exchangers. The main results are presented in Fig.3.9 where all cases showed their best performance with a resorber inlet quality of q=1. Note that the model presented in chapter 2 over predicts the performance of the cases considered, by about 4.5% on average. An exception can be noticed for case 19, when the model over predicts the performance by 22%. This case is a low temperature lift case, for which the (low) glide is relatively large.
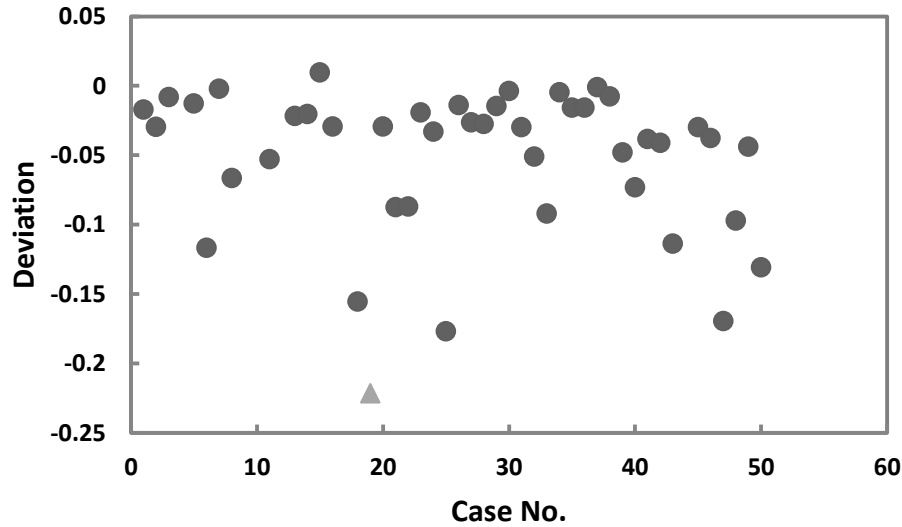
Fig.3.9. Deviation between the earlier model presented in chapter 2 (about 4.5% over prediction) and the results from this work. The triangle indicates case 19 that shows the largest over prediction, in comparison with the result of the current model. One source of deviations are expansion losses; another source is the difference in temperature profile between the linear profile assumed by the model discussed in chapter 2 and the actual temperature profile of the ammonia-water mixture.

3.3 Discussion

The results obtained in this chapter show that the compression-resorption heat pump performs optimal if the inlet vapor quality at the resorber is 100%. Although this exact value was not confirmed earlier, Itard [45] observed that increasing the vapor quality at the resorber inlet increases the COP. By increasing the vapor quality the losses of the cycle caused by non-isentropic compression and expansion are divided over a larger enthalpy change. In case of a superheated outlet of the compressor, the advantage of the increase in enthalpy change during phase change is offset by an increase in temperature driving force.

Finding the optimal ammonia concentration where the vapor quality at the resorber inlet is 100% at the desired temperature driving force requires a small step size on the ammonia concentration. At high ammonia concentrations the step size should be chosen smaller because the temperature increases sharply close to the saturated vapor line. For the example shown in Fig.3.8, the vapor quality is $q=1$ up to 13% ammonia concentration. The results for concentrations lower than 13% are invalid since the outlet of the compressor would be superheated, which is not accounted for in the equations used. At ammonia concentrations larger than 13% the vapor quality decreases because the outlet temperature is limited by the process side. As a consequence, the COP reduces with the increasing of ammonia concentration. Note that the small discontinuities in the figure are caused by the numerical accuracy which results from the vapor quality step size used in the simulations.
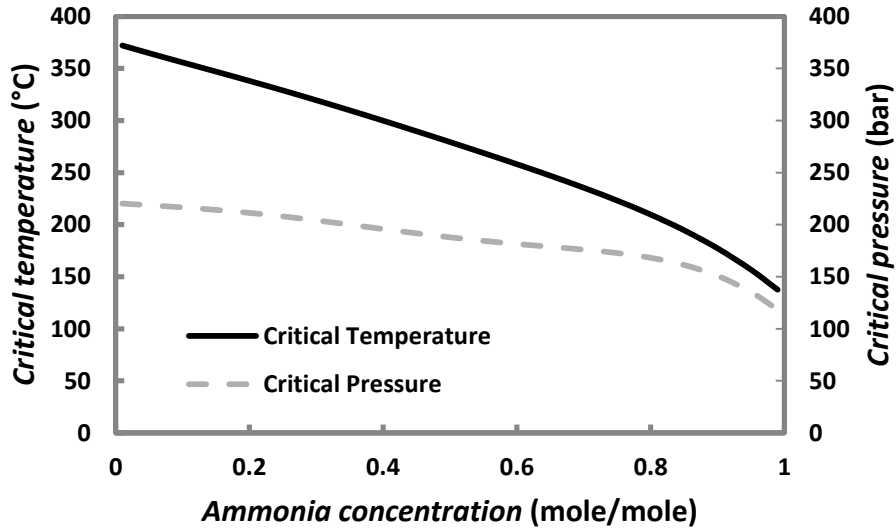
Fig.3.10. Critical temperature and pressure of the ammonia water mixture as function of ammonia concentration.

The latent heat becomes smaller when moving closer to the critical point of the fluid. The critical point at lower concentrations is located at higher temperatures due to the fact that the critical point of water is higher than that of ammonia – see Fig.3.10 for details. Since a heat pump working with ammonia-water mixtures with a large ammonia concentration is always working closer to the critical point compared to the same heat pump operating with a mixture with a low ammonia concentration and ammonia has a smaller latent heat by nature, a lower ammonia concentration is generally preferred. The thermodynamic losses can then be divided over the larger latent heat of the mixture with low ammonia concentration.

Temperature glides in the desorber have a smaller influence on the performance of the heat pump. Therefore, it is especially important to match the resorber temperature glide. Deviations between the model discussed in chapter 2 and the model discussed in this chapter are shown in Fig.3.9 They are caused by expansion losses that have not been included in the model presented in chapter 2. Furthermore, the glide is assumed linear in that model, while the glide in the compression-resorption heat pump is not necessarily linear. Another source for deviations is a system where the process side has exactly an equal glide on both the hot and cold side, whereas the compression-resorption heat pump will have a slightly smaller glide on the low temperature side. This leads to an over prediction by the model presented in chapter 2 where the best example is case 19 (indicated by a triangle in Fig.3.9). The over prediction is large since the difference between the highest and lowest process temperature is quite small, increasing the relative importance of the gliding temperatures. The average over prediction of 4.5% of the model presented in chapter 2 compared to the model presented in this chapter shows that the model of chapter 2 is a good approximation method for the performance, which can be applied when the performance of a large number of cases has to be investigated. The model presented in this chapter includes more details and is best applied to check the performance of a selected case and as a starting point for dimensioning the heat pump system in a practical situation.
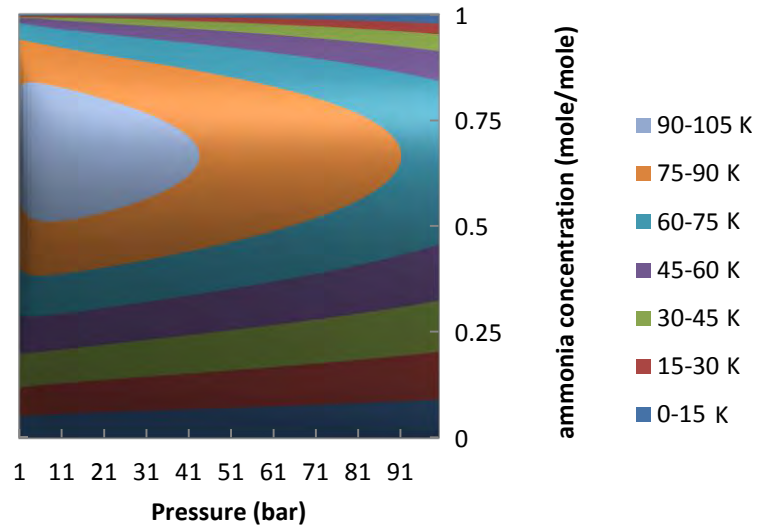
Fig.3.11. Maximum temperature glide as function of ammonia concentration and pressure, when the condition of the mixture is changed from saturated liquid to saturated vapor.

Fig.3.11 illustrates the temperature glide ranges that can be obtained with ammonia-water mixtures. The maximum attainable temperature glide in a resorber working with an ammonia-water mixture is almost 98 K. This glide is obtained with an ammonia concentration of 69 mol% and an operating pressure of about 8 bar. In the range of 1-100 bar, the operating pressure has an influence of up to 40 K in the temperature glide when high ammonia concentrations are selected. This explains the differences in ammonia concentration for similar resorber glides obtained earlier: the operating temperature of the resorbers in different cases is different, thereby changing the resorber operating pressure and thus the required ammonia concentration. At very low concentrations, the operating pressure shows a very limited influence on the temperature glide in the range of 1-100 bar.

It must be noted that only the inlet and outlet temperatures of the process are used to produce the results provided in this chapter. Since the heat duty of these processes is not given the results are not checked for temperature crosses in the heat exchangers. When a CRHP is going to be applied to these processes, care should be taken regarding the heat exchanger design, as a temperature cross might appear in the *Q-T* diagram in some of the cases – then a different ammonia concentration should be chosen. Practically, this can be done by looking at the other end of the spectrum of ammonia concentrations. For instance, if a low concentration is optimal but produces a temperature cross, the high concentration optimal result should be evaluated, and vice versa.
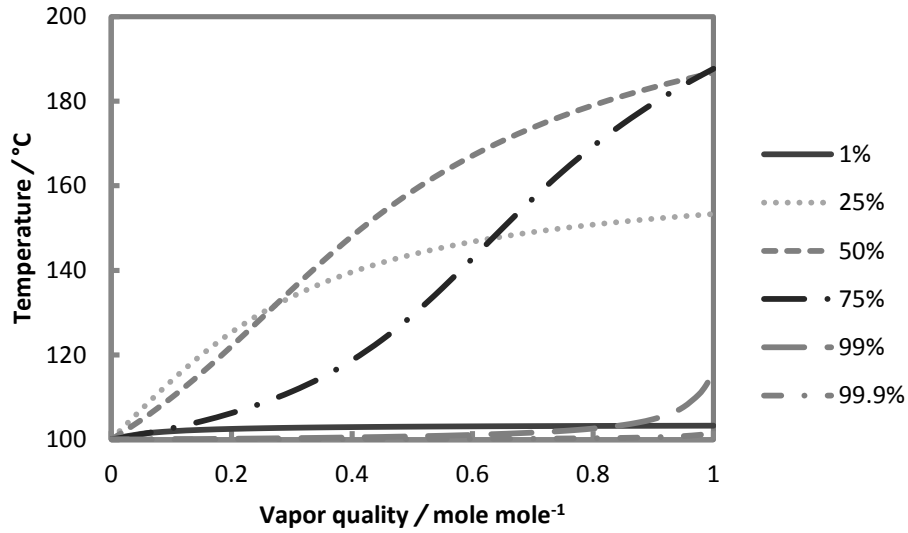
(a)
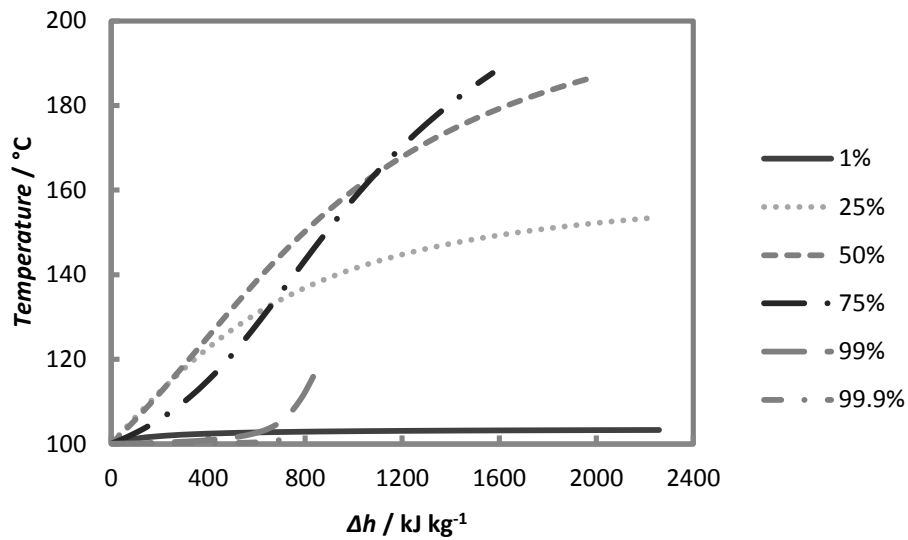
(b)

Fig.3.12. Temperature profiles for different ammonia concentrations at 100°C saturated liquid temperature as function of vapor quality (a) and change in enthalpy from saturated liquid state (b).

Fig.3.12 presents the difference in temperature profile as function of vapor quality (a) and enthalpy (b) in a heat exchanger. As an example, 100°C is taken for the low temperature side to clearly illustrate the differences in the temperature profiles. Note that maximum desorber and minimum resorber temperatures are often found around 100°C when looking to process industry.

Fig.3.12 clearly shows that for low glide applications, it is possible to choose for a high or low ammonia concentration. Note that having 1% of water in ammonia shows a larger glide than having 1% of ammonia in water. There is a sharp peak in temperature when reaching high vapor quality in combination with high concentration ammonia mixtures. When large glides are required then mid-range ammonia concentrations should be selected.

3.4 Conclusions

This chapter proposed a more detailed model for the performance evaluation of compression resorption heat pumps, which was successfully applied to evaluate fifty industrial distillation column cases. The main conclusions are:

- For the majority of the 50 industrial cases considered CRHPs show economic and energetic advantages up to a factor of 7 when compared to conventional reboilers.
- CRHPs deliver economic advantages at feasible temperature lifts up to 124 K.
- In general, the optimum results are obtained when the glide of the process is exactly matched by the resorber temperature glide. Temperature glides in the desorber are of less influence than temperature glides in the resorber. At higher temperatures the dissipated power is larger.
- At higher resorber outlet temperatures low ammonia concentrations are favorable while at low resorber outlet temperatures higher ammonia concentrations are favored.
- For optimal performance, the ideal vapor quality at the resorber inlet is 100% because the compressor and expansion losses are divided over the largest possible enthalpy change without increasing the temperature driving forces.
- The optimum evaluated ammonia concentration for low temperature glides on the order of 1-3 K is either in the range of 0.001-5 % or in the range of 99-100%, for which the condition of 100% vapor quality at the resorber inlet is satisfied.
- There is no single NH_3 concentration suitable for a given resorber glide. The optimal NH_3 concentration is dependent on the operating temperature of the resorber, which influences the operating pressure of the resorber and therefore the temperature glide.
- The dependency of the ammonia concentration on the operating temperature is larger in case of solutions with a high ammonia concentration.
- A small step size on the ammonia concentration is needed in order to find the 100% vapor quality condition at the inlet of the resorber. There is a small amount of water included that increases the temperature sharply, close to the vapor line. This increase in temperature increases the driving forces that increase the losses in efficiency.

Since the optimal performance results are obtained when the inlet of the compressor contains some liquid, it is recommended to investigate the ability of compressors to operate in the wet compression regime. Up to the current date, limited results are available related to this topic [43, 116]. The main conclusion is that the isentropic efficiency of wet compressors is lower as compared to dry compression, but it is expected that the efficiency can still be improved.

4 EXPERIMENTAL INVESTIGATION OF THE ABSORPTION OF AMMONIA-WATER IN A MINI-CHANNEL ANNULUS

The ammonia-water mixture is commonly used in compression-resorption heat pumps. The heat transfer performance of a mini-channel annulus operated with an ammonia-water mixture under absorption conditions has been experimentally investigated. Heat exchangers comprised of annuli can be used in compression-resorption heat pumps. Measurements have been executed in a channel with a hydraulic diameter of 0.4 mm and a length of 0.8 m with an average eccentricity of 0.6. The experiments are used to determine the heat transfer coefficient and pressure drop during absorption for different operating conditions along the channel. The measured heat transfer coefficients vary from 1000 to 10000 W m^{-2} K^{-1}. Results are presented as function of heat load, mass flux and vapor quality in order to investigate the dependency of heat transfer coefficients on the given variables. Mass flux is directly measured; vapor quality is obtained from equations of state with pressure and temperature at in- and outlet of each channel as input, assuming equilibrium conditions. The heat transfer coefficient increases with increasing mass flux, increasing inlet vapor quality and increasing heat load. The heat transfer coefficient increases sharply between mass fluxes of 120 and 175 kg m^{-2} s^{-1} at low inlet vapor qualities and constant heat load. The pressure drop shows an increasing trend with increasing mass flux and vapor inlet quality. The pressure drop measurements have been compared against literature models originally designed for tubes. One of these models is able to predict the measured pressure drop in the current channel within 25% deviation. The heat transfer performance was compared against empirical models from literature, which show very little agreement with experiments. The models are intended to predict condensation heat transfer in tubes, so they cannot fully take the annular geometry and mass transfer resistances into account, causing large discrepancies between predicted and experimental heat transfer coefficients.

This chapter is for a large part based:

D.M. van de Bor, C. Vasilescu, C.A. Infante Ferreira. *Experimental Investigation of the Absorption of Ammonia-Water in a Mini-Channel Annulus,* Submitted to Experimental Thermal and Fluid Sciences, 2014

4.1 Introduction

In previous chapters it is shown that the application of high temperature heat pumps like compression-resorption heat pumps can be an attractive way to improve the efficiency of distillation processes. However, such heat pumps require relatively large heat exchangers. In order to reduce the size and cost of these heat exchangers, the application of mini-channel heat exchangers can be beneficial. Mini-channel heat exchangers have similar or smaller diameters than the capillary constant,

$$d = \sqrt{\frac{2\sigma}{g(\rho_L - \rho_V)}}$$

(4.1)

For mini-channels it has been long known that decreasing the channel size in heat exchangers increases heat and mass transfer performance. Reducing the channel size also results in larger heat transfer area per unit of volume which could possibly lead to cost reductions and lower material use. Experiments have been executed on a diversity of fluids in mini channels of different shapes [25, 37]. However, the heat and mass transfer performance in mini-channel size annuli has not been investigated often. Heat and mass transfer performance data for ammonia-water mixture, a fluid used in absorption and compression-resorption heat pumps, is missing. For single phase flow the use of annuli proved to increase the Nusselt numbers of laminar flows and thus the heat transfer coefficient [105]. Similar advantage is expected when using mini channel annuli in heat pumps.

A significant amount of experimental work has been done on condensation in annuli, although data in open literature is still limited. Honda et al. [41] and Nozu et al. [80] performed experiments in the annulus of a double tube coil heat exchanger with 4 straight lengths and 3 u-bends with surface enhancements on the inner tube using R-11 and R-113 and using the non-azeotropic mixture R-114/R-113 (Nozu et al., [81]). In these experiments the inner tube had an outer diameter of 19.1 mm and the outer tube had an inner diameter of 24.8, 25.0, 27.2 and 29.9 mm. Mass fluxes ranged from 50 to 300 kg m^{-2} s^{-1}. The heat transfer coefficient was shown to be larger at higher vapor qualities and in U-bends, and the variation of the heat transfer coefficient between U-bends and straight sections was shown to be decreasing for lower vapor qualities. The vapor mass transfer coefficient for the mixture showed the same behavior. The local heat transfer coefficient was increased by 2 to 13 times compared to an annular tube without enhancements. In [41] an empirical equation for the local heat transfer coefficient was developed in which surface tension controlled flow models were introduced for flows with low vapor velocities and vapor shear controlled flow models were introduced for high vapor velocity flow regimes.

Wang and Du [107] discuss an analytical model for vapor flowing through horizontal annuli accounting for gravity, vapor shear and surface tension. They concluded that the vapor shear stress and surface tension influenced the condensing flow by influencing the distribution of liquid over the tube. Comparing their model with experiments led to the conclusion that the Nusselt number for most data is predicted within 30% accuracy. Yan and Lin [114] numerically studied natural convection during condensation and evaporation in annuli with both the inner and the outer surfaces heated. Their main conclusion was that the latent heat greatly increased the heat transfer coefficients compared to single phase flows. Wang et

al. [108] analyzed turbulent downward gas/condensing vapor flow inside an annulus using an analytical model developed using available correlations for interfacial shear stress. The model was compared against experimental data for steam-air flows through annuli by Stewart et al. [96] and Kasprzak and Podpora [49]. The obtained heat transfer coefficient proved to be greatly dependent on Reynolds number and ratio between inner and outer diameter. Relatively large tube ratios significantly enhanced condensation rates.

Bandhauer et al. [7] did experiments with R-134a, R-123 and R-12 inside micro-channels with 0.506 < d < 1.524 mm under different operating conditions. The measured heat transfer data showed large differences from the models developed for larger channels mainly because the flow regime and interfacial shear force played a more significant role. Park et al. [85] experimented with R-1234ze inside a multiport extruded tube with a hydraulic diameter of 1.45 mm for each square channel. They found trends of decreasing heat transfer coefficient with decreasing mass flux, vapor quality and increasing saturation temperature. The heat transfer coefficient was unaffected by entrance conditions or condensation heat flux. The condensation of R-152a inside circular 1.152 mm diameter and square 0.952 mm hydraulic diameter mini-channels has been investigated experimentally by Liu et al. [66]. Both pressure drop and heat transfer coefficients were shown to increase with mass flux and vapor quality. Similarly to what is reported by Park et al. [85], the heat transfer coefficient decreased with increasing saturation temperature. For single phase flows the heat transfer coefficient agreed with the correlations proposed by Gnielinksi [31].

Cavallini et al. [11] performed a comprehensive experimental study on the condensation of refrigerants. Different models were applied to the experimental data together with their own model. They suggested that the disagreement between experimental and calculated values are the result of liquid entrainment. Based on this criterion, they recommended a heat transfer model for condensation in mini-channels which takes into account the effect of the entrainment rate of droplets from the liquid film. The agreement between the data for R-134a, R-410A, and R-236ea in a 1.4 mm-inner diameter mini-channel and predictions from their model was within 20%. The general trend was increasing heat transfer coefficient with increasing mass flux and vapor quality.

Koyama et al. [57] indicated that the shear stress plays an important role in determining the heat transfer coefficient. They proposed a correlation that takes into account the effect of both forced and free convection where the forced convection term is calculated based on the frictional pressure drop. Wang et al. [110] showed that at low mass fluxes or vapor quality a stratified flow pattern prevails where the heat transfer is governed by conduction across the film. At higher mass fluxes or quality the pattern changes to annular flow in which forced convection is the dominating heat transfer mode. Their model is able to take flow transitions into account.

Garimella et al. [29] measured two-phase pressure drop in five circular channels ranging in hydraulic diameter from 0.5 mm to 4.91 mm. A pressure drop model was developed for a unit cell in the channel based on the observed slug/bubble flow pattern for these conditions. The unit cell comprised a liquid slug followed by a vapor bubble that is surrounded by a thin, annular liquid film. A correlation for non-dimensional unit-cell length based on slug Reynolds number was used to estimate the total pressure
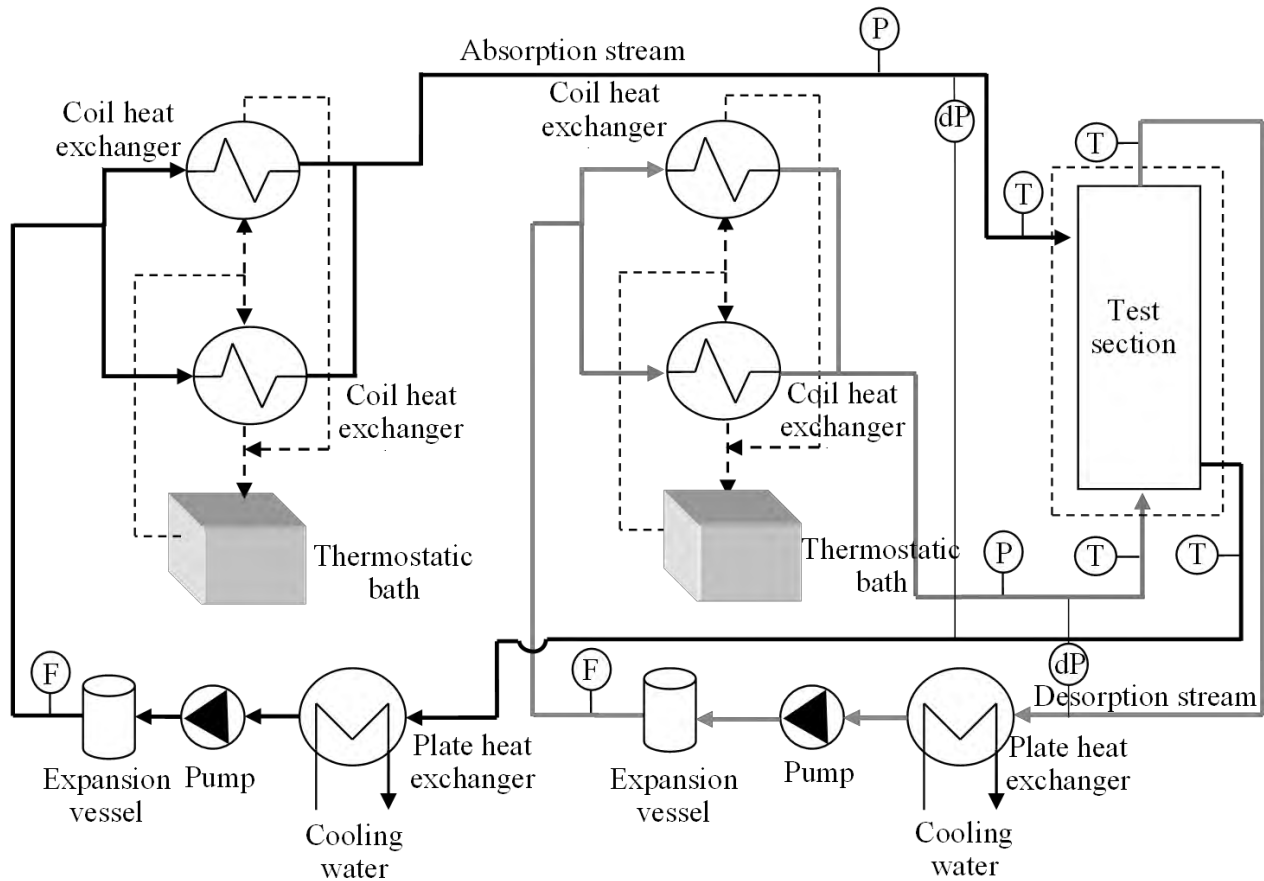
Fig. 4.1. Schematic diagram of the test facility. The test section is depicted on the right hand side of the drawing, the utility section of the absorption stream on the left and the utility section of the desorption stream (water for the reported experiments) in the middle.

drop during condensation. Determan and Garimella [21] conducted experiments with a micro-channel falling film desorber. The main purpose of their research was to capture the effects of the concentrated solution flow rate and the vapor fraction on the desorber heat duty and heat transfer coefficient.

The objective discussed in this chapter is to determine the heat transfer and pressure drop performance of a vertical mini-channel annulus with a hydraulic diameter of 0.4 mm and a length of 80 cm during the absorption of ammonia in an ammonia/water mixture. The heat transfer performance and pressure drop of ammonia water in a mini channel is measured because the ammonia-water mixture is applied in compression-resorption heat pumps as working fluid and mini-channel heat exchangers offer large heat transfer area compared to their volume, while limited amount of experimental data is available [20, 21]. The effect of mass flux, heat flux and vapor inlet quality will be investigated. The experimental data will be compared to prediction methods for pressure drop and condensation heat transfer in mini-channels. Measurements are done close to the industrial operating conditions of the project partners.

Fig. 4.2. Left: Mini-channel cross-sections. Light gray is the flow area; dark grey is the wall. Right: 3D drawing of 1.1x200 mm inside diameter tube including the shell tube with 2.5 mm external diameter. For the annulus under consideration, d_1 = 1.1 mm, d_2 = 1.6 mm, d_3 = 2.0 mm and d_4 = 2.5 mm. The heat exchanger is insulated with heat resistant foam to prevent heat loss to the ambient.
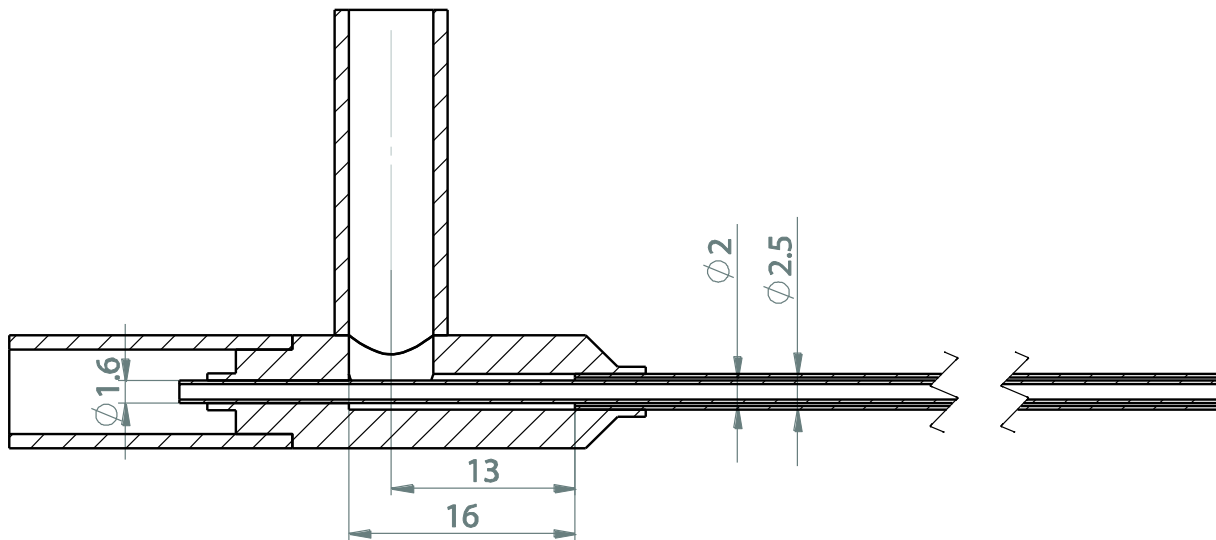
Fig. 4.3. Detail of mini-channel inlet for the mini-channel under consideration.

4.2   Experimental Setup and method

Fig. 4.1 shows the schematic of the test setup which is located in the Delft University of Technology, Process and Energy Laboratory. The test setup can be used for the measurement of the heat transfer coefficients in a set of tubes and annuli with three different tube diameters. This chapter focusses on the 1.1 mm tube with a length of 0.8 m, where the annulus has an inner diameter of 1.6 mm and an outer diameter of 2.0 mm as illustrated in the left side of Fig. 4.2. When using small tube sizes the wall becomes relatively thick. In the inner tube of the test section water can be heated or desorption can take place with the flow in upwards direction while absorption is taking place in counter current flow in the annular space around the tube. The tubes are precision tubes delivered by Unimed S.A. The surface roughness is specified to be between 0.8 and 1.6 µm for the inside of the tube, while the outside of the tube has a roughness of 0.4 µm. The right side of the figure shows a 3D-drawing of a heat exchanger. The design of the inlet section of the heat exchanger is depicted in Fig. 4.3.

Table 4.1. Accuracy of sensors and manufacturing tolerances.

Equipment	Brand	Type	Variable	Max deviation
Tubes	Unimed S.A.	1.1 mm	d_1	± 0.015 mm
			d_2	$+ 0.04$ mm
		1.6 mm	d_3	± 0.015 mm
Pressure transducer	Siemens	Sitrans P DSIII	P	± 0.08 bar
DeltaP transducer	Siemens	Sitrans P DSIII	dP	± 0.008 bar
RTD		PT100 B class	T	± 1.3 K
Flowmeters	Bronkhorst	Mini-Coriflow	$\dot{M}$	± 0.046 kg h^{-1}
Density measurement		M14	ρ	± 5 kg m^{-3}
			T	± 0.5 K

The inlet temperature and pressure conditions of the tube and shell side streams are controlled with a utility section. The utility section is separated into two nearly identical parts: one loop for the tube stream and one loop for the shell stream. Each side consists of a plate heat exchanger, a pump, an expansion vessel and two coil heat exchangers. Two thermostatic baths are used to adjust the inlet temperatures of the absorption, desorption or water streams. The streams are cooled in the plate heat exchangers from which they leave in sub-cooled liquid state. Positive displacement pumps provide circulation and pressurize the streams. The two coil heat exchangers are used for heating the streams to the desired conditions.

The temperature of the fluid can be maintained by the electrical tracing between the thermostatic baths and the entrance of the heat exchanger. The electrical tracing is wrapped around the tubes connecting to the heat exchanging test section to compensate for the heat losses to the surroundings. The tracing is controlled by an external temperature sensor placed to the tube wall and a rKc Rex CB100 temperature controller. Rock wool insulation is wrapped around the test section in order to reduce heat losses to the ambient and all lines are insulated with heat resistant foam. The annular side of the heat exchanging test section is filled with ammonia-water with an ammonia concentration of 0.386 mole per mole. The tube side of the heat exchanging test section is filled with water.

Pressure is measured by two different pressure transducers at the in- and outlets of the heat exchanger, all delivered by Siemens. One is an absolute pressure transmitter while the other measures the pressure drop across the test section. The mass flow meters are made by Bronkhorst (Mini-Coriflow M14). All sensors are connected to a Keithley 2701 data acquisition system. The data acquisition system is connected via a RJ45 connection to a personal computer with Labview 9 installed, which acts as a data logger. All data from the data acquisition system is read in periods of 2 seconds. The flow meters have an additional digital connection to the personal computer via a RS-232 connection. The flow, density and temperature at the flow meter can be read 10 times per second. The accuracy of the sensors as specified by the manufacturer is listed in Table 4.1.

Since the heating of mixtures in the two phase area are characterized by a boiling trajectory or temperature glide, the enthalpy and vapor quality at the in- and outlets can be determined by assuming equilibrium conditions. The B-class PT-100 elements used in the setup were calibrated separately by
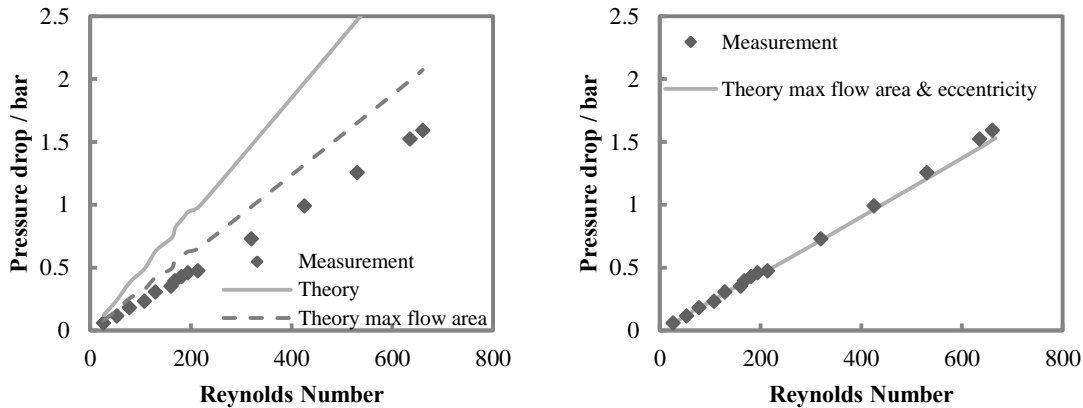
Fig. 4.4. Deviation in measured and theoretical pressure drop in the mini-channel annulus under consideration. Maximum specified tube diameter tolerances are applied in the left hand side. The right hand side illustrates the deviation between the measured pressure drop and theory for the annulus under investigation when both eccentricity and maximum dimensional tolerances are taken into account. The bumps in both measurement and theory are caused by density and viscosity changes due to small deviations in operating temperatures.
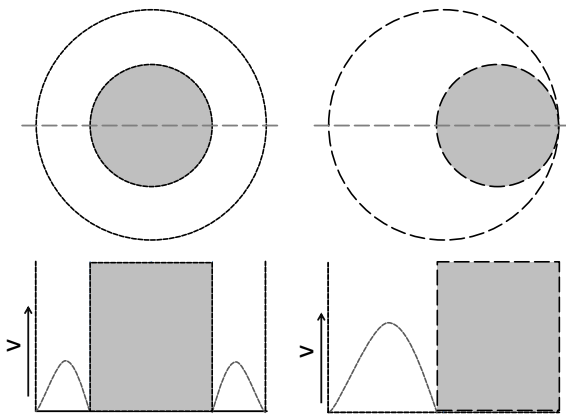
Fig. 4.5. Velocity profile in a concentric and an eccentric annulus at the centerline at equal pressure drop. The area underneath the velocity profile is the volume flow. At equal pressure drop, the volume flow through the eccentric annulus is larger because of the larger distance between the inner and outer wall allows the fluid to reach a higher maximum velocity. Therefore the pressure drop in an eccentric annulus is lower if the volume flow is equal.

using the thermostatic baths filled with silicon oil as references. All four sensors were tested with bath temperatures ranging from 60 to 180 °C in steps of 30 K, covering the entire temperature range of the experiments. These calibration measurements showed a linear profile and the deviations from the thermostatic bath also proved to be linear. After calibration the temperature sensors show an accuracy of 0.1 K for the experimental temperature range of 60 to 180 °C. Experiments are carried out within the range of 100 to 180 °C to match industrial operating conditions. The accuracy of the setup as a whole has also been verified. To calibrate the setup, pressure drop measurements were conducted on the 1.1 x 80 cm tube with corresponding annulus using water as the heat transfer fluid. The left side of Fig. 4.4 illustrates the deviation between measured pressure drop and laminar flow theory for pressure drop in the mini-channel annulus. The tubes themselves have specified production tolerances. Including the tolerances in the calculation for the pressure drop theory, the deviation between experiment and

measurements reduces to approximately 25%. The pressure drop model is based on laminar flow theory, which is an exact solution to the Navier-Stokes equation. Fluid properties have been obtained at measured temperatures by making use of the FluidProp [17] / RefProp [61] fluid property library. Equations for the ammonia-water mixture are based on those by Tillner-Roth and Friend [102]. The explanation for the deviation from theory might be that the tubes are not placed fully concentric along the length of the tube. The heat exchangers are flexible and both Muzychka and Yovanovich [76] and VDI [105] report lower pressure drop when the central tube is placed eccentrically in a tube. Pressure drop in an annulus placed around a fully eccentrically placed tube can be 60% lower compared to full concentric annuli at the same conditions. This is illustrated in Fig. 4.5. At equal pressure drop, the maximum velocity of the fluid in the eccentric annulus is higher. The area underneath the velocity profile (volume flow) is thus larger. Thus at equal volume flow the pressure drop is smaller in an eccentric annulus. Including the eccentricity in the calculation of the pressure drop results in the right side of Fig. 4.4. The non-linearity that is visible in both the experiments and the theory can be fully explained by variation of the operating temperature. Higher pressure drop is obtained at lower temperature.

It can be expected that the eccentricity has also influence on the heat transfer performance. Cheng and Hwang [15] were the first to consider laminar forced convection heat transfer in eccentric annuli. They derived the temperature profile of a fully developed laminar flow in an annulus with the boundary condition of constant heat flux through both walls. Trombetta [103] derived the same temperature profile of a fully developed laminar flow in an annulus, but for different boundary conditions. Manglik and Fang [69] numerically calculated the velocity and temperature profiles for various diameter ratio's and eccentricities of the annulus. They observed that the laminar Nusselt number generally decreases for increasing values of the eccentricity and radius ratio. For an eccentricity of 0.6 and for the ratio of diameters for the tube under consideration, these authors report a value for the Nusselt number that is 3 times lower than for a similar concentric tube.

Experiments have been conducted in the experimental setup described above. The tube side of the setup was filled with softened water, the shell side of the setup was filled with an ammonia water mixture of 38.6 mole% ammonia. At the start of the experiments the flows are set, as well as the temperature of the thermostatic baths and the temperature of the tracing. Operating pressure of the setup could be indirectly controlled by changing the set point of the thermostatic baths. The actual inlet temperature of the heat exchangers is generally slightly lower than the set point of the electrical tracing as there is some distance between the tracing and the inlets.

The overall heat transfer coefficient has been determined from the inlet temperatures and the heat transfer area. The length of the inner tube is 830 mm. The distance between the inlets on the shell side is 800 mm, and the diameter of the shell side in- and outlet is 6 mm. This results in a heated length of 806 mm if axial conduction can be ignored. At a distance of approximately 30 mm from each in- or outlet a thermowell is installed. The thermowells are filled with thermal oil in order to improve heat transfer to the PT100 element installed in the thermowells.
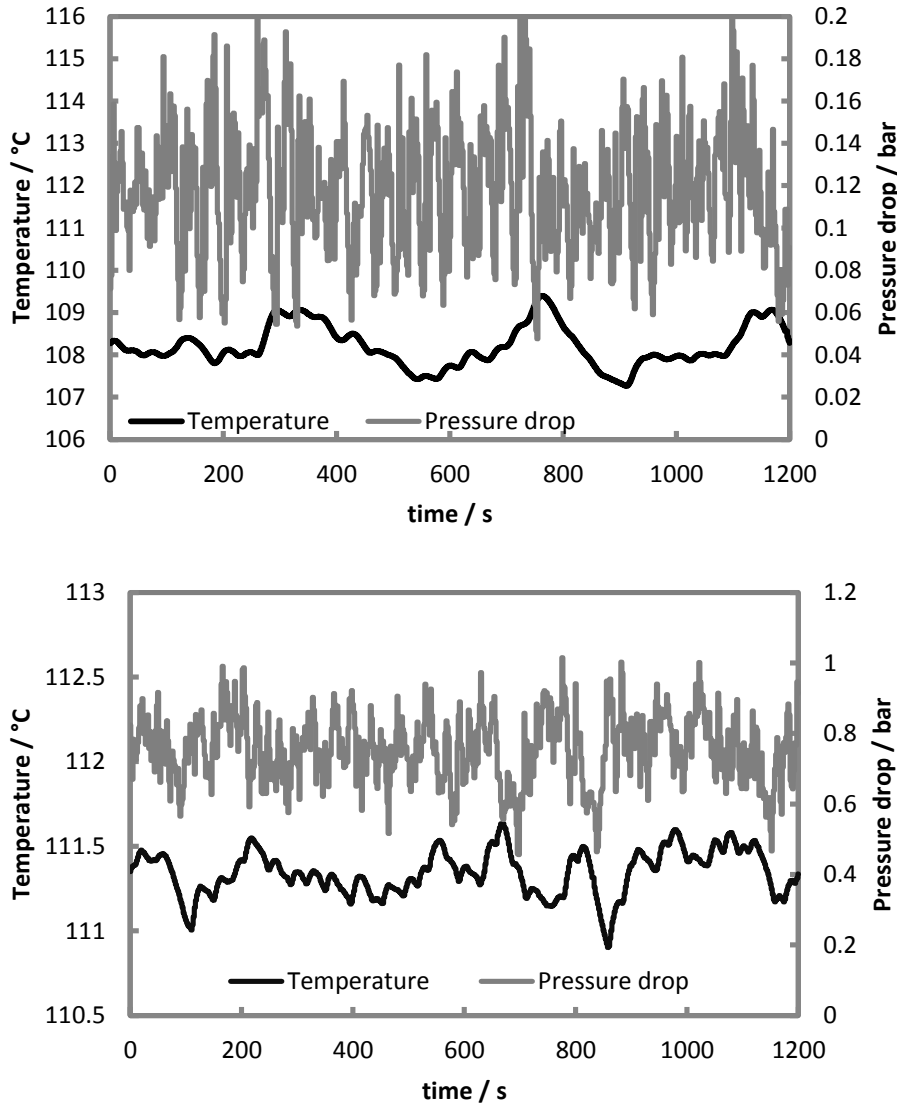
Fig. 4.6. Example of the development of absorber outlet temperature and pressure drop over time at a mass flux of 75 kg m^{-2} s^{-1} for the absorber with the absorber outlet temperature fluctuating between 107 and 109 °C (top). The bottom presents a similar example at higher mass flux. The mass flux is 250 kg m^{-2} s^{-1} for the absorber, with the absorber outlet temperature fluctuating between 111.2 and 111.6 °C.

During transient temperatures it becomes clear that the PT100 elements and thermowells have inertia. In steady state however, it is assumed that the temperature indicated by the PT100 in the thermowell is the actual temperature of the ammonia/water mixture and the water, respectively.

The absorber mass flow, outlet temperature and the pressure drop showed an oscillating character during the experiments. This is illustrated in Fig. 4.6 where values for temperature and pressure are given for 1200 s of a test with 75 kg m^{-2} s^{-1} absorber mass flux (top) and with 250 kg m^{-2} s^{-1} (bottom). The temperature oscillates with ±1 K for the lower flow rate and ±0.3 K at higher flow rate. The pressure drop oscillates 50% around the average at low flow and 33% at high flow. Inlet temperatures were controlled by the electrical tracing which results in random, non-periodic fluctuations in the range of 107 and

110 °C. At larger flow rates, bottom of Fig. 4.6, this periodic behavior was significantly dampened although the frequency of spikes with lower amplitude for pressure drop and mass flux increased. Temperature at high flow rates was more stable and remained within ±0.3 K from the average temperature. The sensitivity of the PT-100 is better than the accuracy. The large peaks occurring in Fig. 4.6 could be a result of the flow pattern, which can be expected to be a slug flow. At larger flow rates, the pattern could have shifted to an annular pattern at the inlet. In a slug flow the vapor and film region is followed by a liquid slug which flows at a relatively high velocity and high density, which could give rise to a temporarily larger pressure drop. Annular flow patterns do not have such an intermittent flow pattern, resulting in less pressure drop fluctuations. A second possibility is that at lower flow rates the operating pressure and temperature is more influenced by the switching on and off by the electrical tracing element. Closer to the outlet of the annulus, flow velocities are lower due to the absorption of ammonia-water vapor into the liquid phase.

4.3   Data reduction

It is not possible to measure the heat transfer coefficients directly from the sensor data from the setup described in section 4.2. The measured mass flows, temperatures, pressures and pressure drops have to be translated to temperature difference, vapor quality, thermal power and heat transfer coefficient.

As experiments are performed with water in the tube side, pressure drop on this side of the heat exchanger is of limited importance. On the shell side of the heat exchanger the pressure drop is of importance as the pressure influences vapor quality, and thereby the transfer of thermal energy. A lower outlet pressure means less ammonia has been absorbed.

The average temperature difference was determined by dividing the heat exchanging test section in 10 segments with equal heat load. Then the temperature difference was calculated by taking the difference between the bulk water temperature and the equilibrium temperature of the ammonia/water mixture. The resulting temperature differences were averaged over the 10 segments, resulting in the average temperature driving force. With a heated length (L) of 806 mm, the heat transfer area at the outside of the inner tube is obtained with eq. (4.2).

$$A_o = 2\pi r_o L \qquad \text{(4.2)}$$

The thermal power transferred to the tube is determined from the cooling water flow and compared against the ammonia/water side transferred thermal power assuming equilibrium conditions at the in- and outlets of the test section. The equilibrium condition states that the liquid and vapor have equal temperature and the concentration of the liquid and vapor are equal to the saturated liquid and vapor concentrations at given pressure and temperature. Enthalpy and vapor quality can now be directly determined from FluidProp [17],

$$h = f(P, T, x) \qquad \text{(4.3)}$$

$$q = f(P, T, x) \qquad \text{(4.4)}$$

The transferred thermal power on tube and annular side respectively,

$$\dot{Q}_{tube} = \dot{m}_{tube}(h_{tube,out} - h_{tube,in}) \tag{4.5}$$

$$\dot{Q}_{ann} = \dot{m}_{ann}(h_{ann,out} - h_{ann,in}) \tag{4.6}$$

By comparing the thermal power transferred from annular side of the heat exchanger to the tube side of the heat exchanger it is possible to estimate the error introduced by heat loss to environment and inaccuracy of the equipment. As a best estimate the thermal power transferred to the water side is used as actual thermal power since most of the tube is insulated by the shell; therefore the tube side has no energy loss to the surroundings. The average temperature difference is used to determine the overall heat transfer coefficient.

$$U_o = \dot{Q}_{tube}/(A_o \Delta T_{avg}) \tag{4.7}$$

The heat transfer coefficient and pressure drop in both laminar and turbulent single phase flows through a circular tube can be determined according to conventional theory with sufficient accuracy; Heat transfer coefficients for laminar flows in tubes are an exact solution of the Navier-Stokes equation and the equation proposed by Gnielinsky for turbulent flows has an uncertainty of up to 6%. Since the inner tube is relatively long and thin, the entrance effects can be ignored [74]. Fluid properties are best determined at the average temperature of the tube. In the shell and tube heat exchanger under consideration four heat transfer coefficients have to be determined: the overall heat transfer coefficient, the heat transfer coefficient for the wall, the heat transfer coefficient for the water in the tube and the heat transfer coefficient for the ammonia/water mixture in the shell. The water side heat transfer coefficient is given by

$$hc_i = Nu \, \lambda/d_i \tag{4.8}$$

Where the Nusselt number is given by laminar theory with a constant heat flux boundary for Reynolds numbers below 2300 and by the Gnielinski equation for Reynolds numbers above 4000.

$$Nu = \begin{cases} 4.36 & for \, Re < 2300 \\ \dfrac{f/8 \, (Re - 1000)Pr}{1 + 12.7\sqrt{(f/8)}(Pr^{2/3} - 1)} & for \, Re > 4000 \end{cases} \tag{4.9}$$

According to ref. [74], the friction factor f can be obtained by eq. (4.10),

$$f = \frac{64}{Re} for \, Re < 2300$$

$$f = (0.79ln(Re) - 1.64)^{-2} \, for \, Re > 4000 \tag{4.10}$$

In the range between Re = 2300 and Re =4000 the value for f was determined by interpolation between the laminar and turbulent friction factor. The maximum value of either the Gnielinski correlation or the laminar Nusselt number has been taken as the Nusselt number in this range. Given the wall thickness, the resistance against heat transfer of the walls is not insignificant.
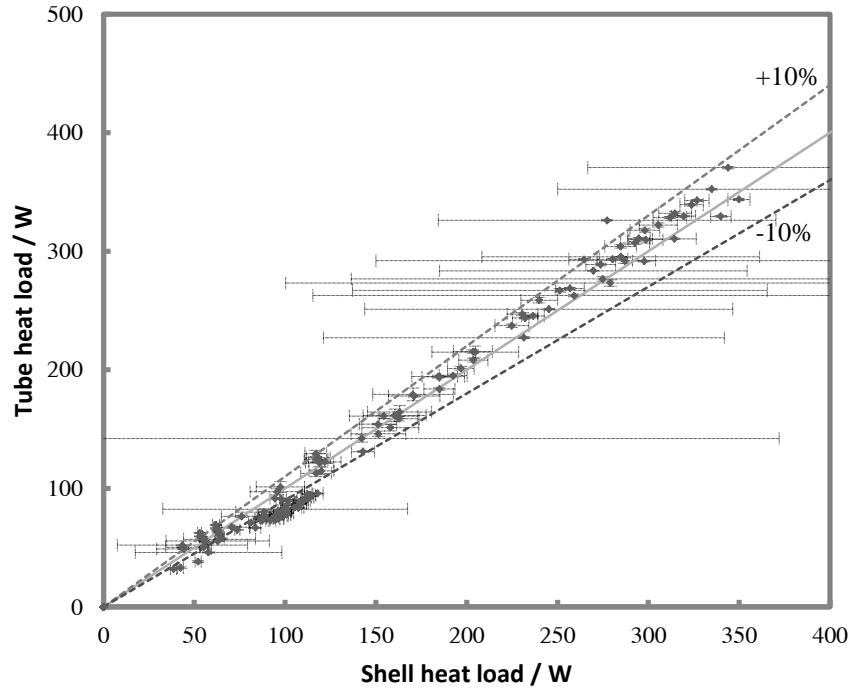
Fig. 4.7. Measured heat load in the tube and in the shell sides for different experiments. The heat load should be equal in the ideal case. The deviations can be explained by the heat loss to the surrounding as well as by measurement errors. Deviations appear to be relatively large when the temperature difference between water in- and outlet is small.

$$hc_{w,o} = \frac{2\lambda_W}{d_o \ln(d_o/d_i)} \qquad \text{(4.11)}$$

Then, to obtain the local heat transfer coefficient at the shell side,

$$\frac{1}{hc_o} = \frac{1}{U_o} - \frac{1}{hc_{w,o}} - \frac{1}{hc_i}\frac{d_o}{d_i} \qquad \text{(4.12)}$$

4.4   Results

This section is divided into five subsections. In section 4.4.1 the energy balance is discussed. The experimental results for the heat transfer coefficient are presented in Section 4.4.2. They are compared with correlations from literature in section 4.4.3. In section 4.4.4 the pressure drop results from experiments are shown and compared against literature in section 4.4.5.

4.4.1   Energy balance

The heat load can be varied by changing the inlet temperature of the heat exchanger and/or the flow rate. The measured heat loads are given in Fig. 4.7. The transferred thermal power measured for the tube side and shell side should be identical. However, some error can arise due to heat losses to the surroundings as well as inaccuracies in temperature, flow and ammonia concentration measurement. Errors are calculated by the methods suggested by Taylor [99]. The large error bars are mainly a result of the oscillations discussed in section 4.2.
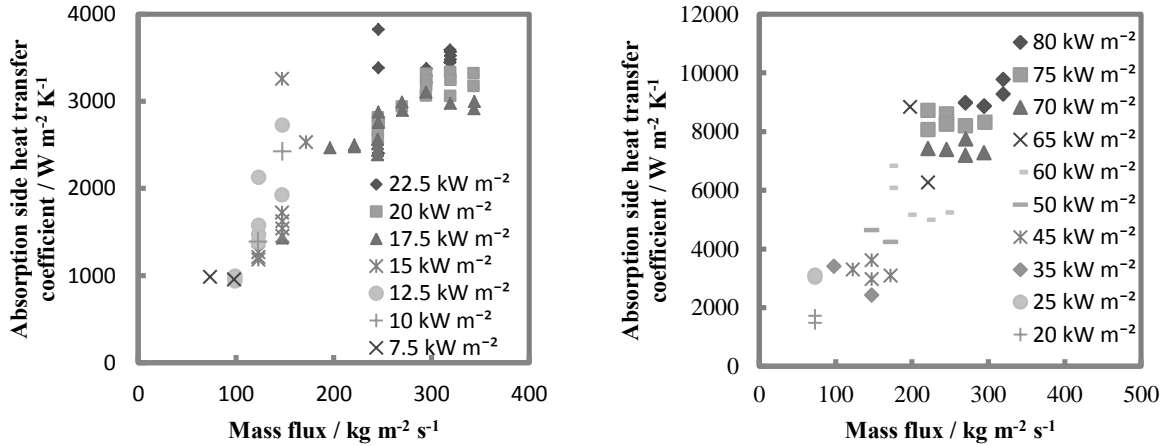
Fig. 4.8. Heat transfer coefficient as function of shell side mass flow with heat load as a parameter for inlet temperature set points of 140°C (left) and 180°C (right). Inlet vapor qualities range between 24 to 40% (left) and 61 to 83% (right) for the respective figures. Each symbol represents an experiment. Error bars have not been included since the error is within the symbol size.

4.4.2   Heat transfer - experiments

In Fig. 4.8 the heat transfer coefficients obtained from eqs. (4.2) to (4.12) are given as function of shell side mass flux, with the heat load as parameter. Both at low (left) as well as at high (right) inlet temperatures of the absorption section, the heat transfer coefficient increases with increasing heat load. The behavior of the heat transfer coefficient as function of the mass flux is slightly different. The heat transfer coefficient seems to increase with mass flux at low vapor qualities (left) and heat loads, while at high vapor quality (right) the heat transfer coefficient appears to be constant for different mass fluxes. At low vapor quality (left) the heat transfer coefficient increases sharply between mass fluxes of 100 and 175 kg m^{-2} s^{-1}. At higher inlet temperature set point (right) the heat transfer coefficient varies less with mass flow and the heat transfer coefficient becomes a function of wall heat flux only. Fig. 4.9 displays the heat transfer coefficient as function of the heat load. A clear trend can be observed for both the low and high temperature inlet conditions of the absorber. For high inlet temperatures (set point 180 °C) the relation between the heat flux and the heat transfer coefficient was determined to be

$$hc_{NH3-H2O} = 0.0152\left(\frac{\dot{Q}}{A_O}\right)^{1.17}$$

(4.13)

With A_O the heat transfer area in m^2 and $\dot{Q}$ the heat transfer rate in W. At lower inlet temperatures (set point 140 °C) the heat transfer coefficient as function of the heat flow across the wall is given by

$$hc_{NH3-H2O} = 0.0079\left(\frac{\dot{Q}}{A_O}\right)^{1.29}$$

(4.14)

Fig. 4.10 correlates the heat transfer coefficient with inlet vapor quality and mass flow. The overall trend that can be observed is an increasing shell side heat transfer coefficient with both increasing mass flow and increasing inlet vapor quality.
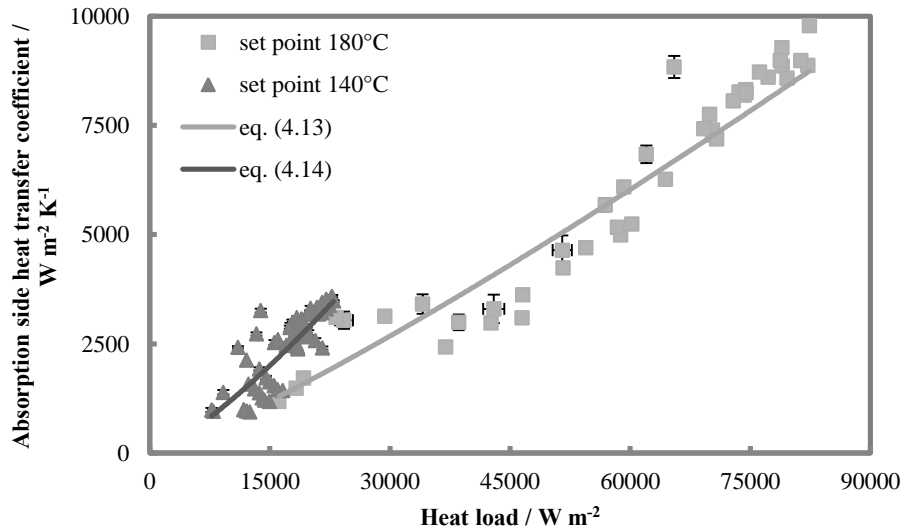
Fig. 4.9. Heat transfer coefficient correlated to heat load. The figure clearly illustrates the dependency of the heat transfer coefficient on the cooling power applied. Furthermore it is shown that at higher inlet temperature and vapor quality the heat transfer coefficient is much larger.
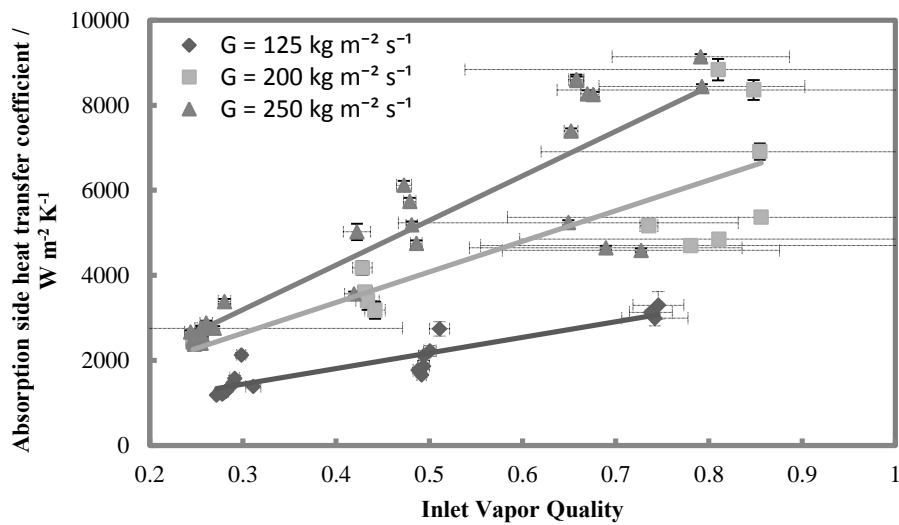
Fig. 4.10. Absorption side heat transfer coefficient as function of inlet vapor quality with mass flux as parameter. It can be observed that increasing mass flow and vapor inlet quality increases the heat transfer coefficient. Each symbol represents an experiment. The lines are trend lines.

4.4.3   Heat transfer - comparison with literature

The measured temperature glides and absorber side heat transfer coefficients have been compared against models by Wang et al. [110] and Koyama et al. [57]. If the models predict the ammonia-water mixture to be outside of the two-phase region, a single phase model is applied. The heat transfer coefficient from the models was averaged over the length of the heat exchanger. The model by Wang et al. [110] is able to make predictions for 45% of the experiments; In 55% of the cases the predicted
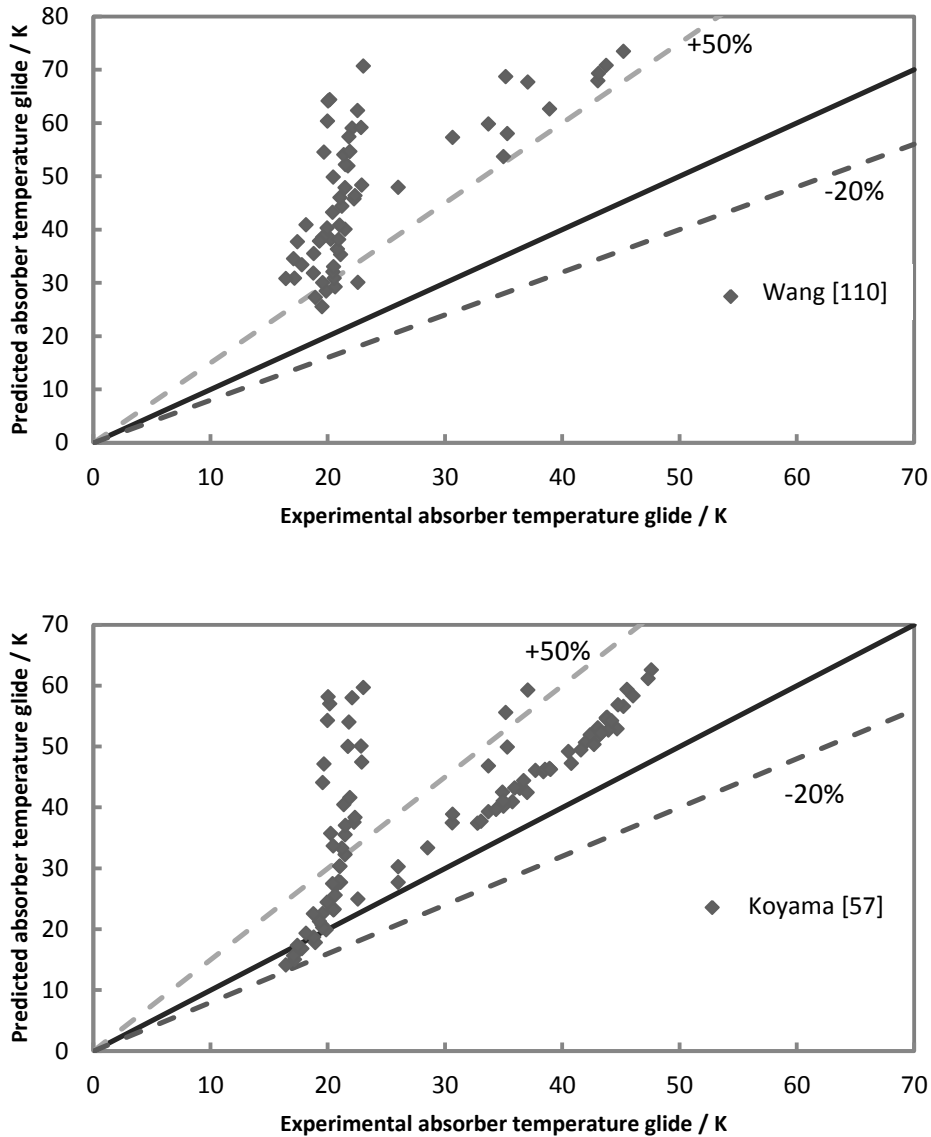
Fig. 4.11. Comparison between measured temperature glide and predictions by Wang et al. [110] (top) and Koyama et al. [57] (bottom).

absorber inlet temperature was outside the range of validity of the equations of state. The temperature glide predicted by the model of Wang et al. [110] is up to 3.5 times larger than the measured temperature glide. The model by Koyama et al. [57] is able to predict 72% of the experiments. The temperature glide is predicted within -20% / +200% for these experiments. The results for the temperature glide are visualized in Fig. 4.11. Fig. 4.12 gives a comparison between the absorber heat transfer coefficient determined from experiments and predictions by Wang et al. [110] (top) and Koyama et al. [57] (bottom). Although the temperature glide was better predicted by Koyama et al. [57], this is not the case for the heat transfer coefficient. On average, Wang et al. [110] over predicts the heat transfer coefficient by a factor 5, where Koyama's correlations over predict the heat transfer coefficient on average by a factor of 17.
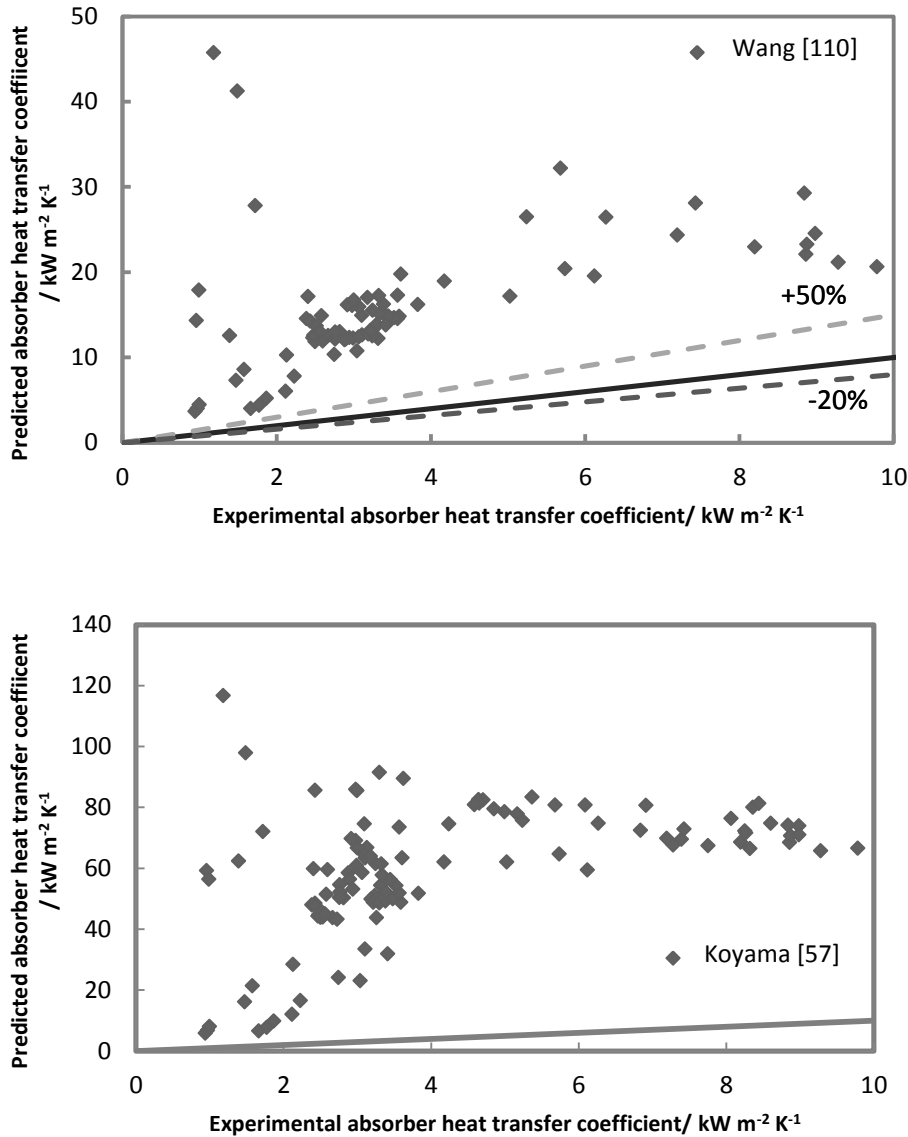
Fig. 4.12. Comparison between absorber heat transfer coefficient determined from experiments and predictions by Wang et al. [110] (top) and Koyama et al. [57] (bottom).

Since both models are intended to predict condensation heat transfer performance in a tube, they do not include mass transfer resistances and do not take into account the geometry of an annulus except for the hydraulic diameter. No new model is proposed here since they could only be validated for annuli with the same eccentricity as the annulus under investigation.

4.4.4   Pressure drop - experiments

From Fig. 4.13 it can be concluded that pressure drop increases with increasing mass flow and inlet vapor quality. Fig. 4.14 displays the heat transfer coefficient as function of pressure drop. The overall trend is an increasing heat transfer coefficient with an increasing pressure drop. Therefore it can be concluded
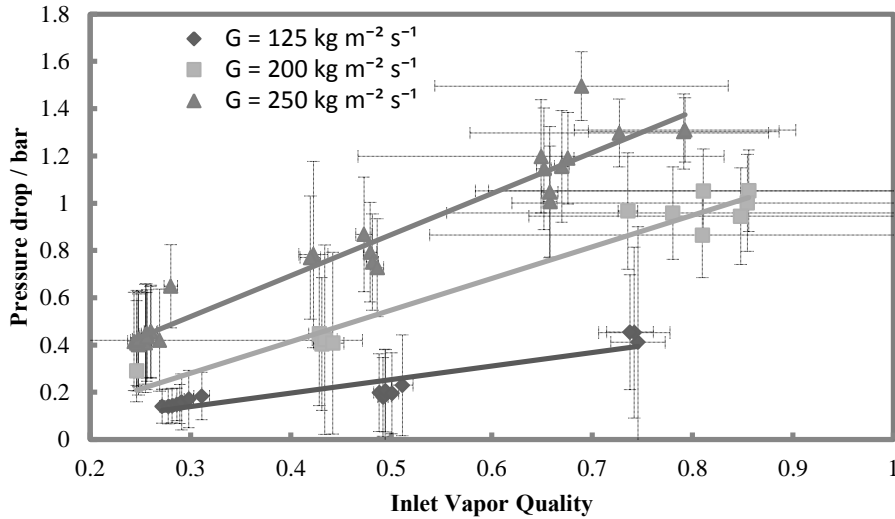
Fig. 4.13. Pressure drop as function of vapor quality with mass flux as parameter. The pressure drop increases with increasing inlet vapor quality and with mass flow. Each symbol represents an experiment. The lines are trend lines.
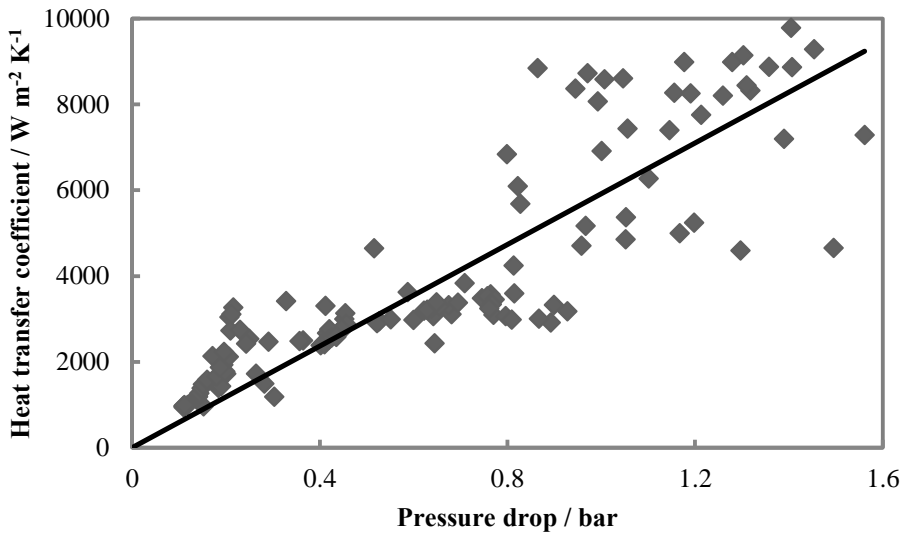
Fig. 4.14. Heat transfer coefficient related to pressure drop. There appears to be a linear relation between the two variables, but the spread is large. The solid line is the trend line.

that no "optimal" pressure drop exists where the heat transfer coefficient is large and pressure drop is relatively small. In an engineering problem one would most likely want to try to increase the heat transfer coefficient to the maximum within the allowable pressure drop in order to minimize heat exchanger area and the associated investment cost.
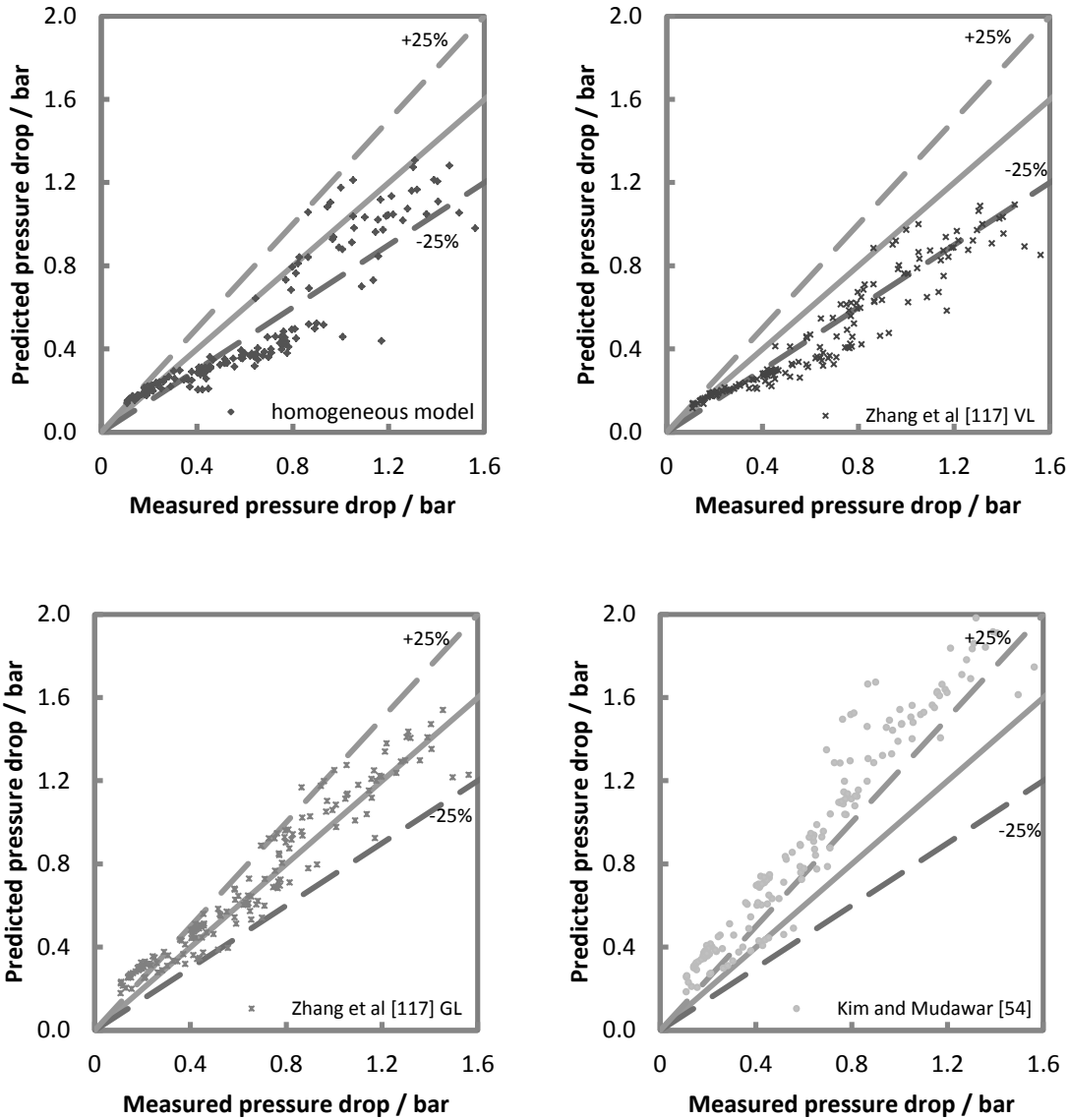
Fig. 4.15 Correlation between the current measurements and different pressure drop models. The Gas-Liquid model by Zhang et al. [117], bottom-left, is able to best predict the pressure drop for pressure drops above 0.3 bar, while the Vapor-Liquid model by Zhang et al. [117], top right, and homogeneous model, top left, perform better at lower pressure drop. The recent model by Kim and Mudawar [54] over predicts the pressure drop by about 40% on average.

4.4.5 Pressure drop – comparison with literature

Pressure drop was predicted based on average flow conditions in the annulus: the numerical average of the pressure drop and vapor quality have been taken to determine the values for fluid properties. In Fig. 4.15 the measurements have been compared against the homogeneous pressure drop model using the viscosity model by Lin et al. [63], empirical models for gas-liquid like air-water and vapor-liquid (refrigerants) by Zhang et al. [117] and against the empirical pressure drop model by Kim and Mudawar [54]. The gas-liquid model by Zhang et al. [117] predicts pressure drops (above 0.3 bar) most accurately, while for lower pressure drops their vapor-liquid model shows better accuracy.

4.5 Conclusions

Inside a mini-channel annulus with a hydraulic diameter of 0.4 mm, a length of 0.8 m and an eccentricity of 0.6, shell side absorption heat transfer coefficients have been obtained for mass fluxes between 75 and 350 kg m^{-2} s^{-1}, inlet vapor qualities between 0.2 and 0.9 mole per mole and heat transfer power between 50 and 350 W. The range of measured heat transfer coefficients is large; heat transfer coefficients between 1000 and 10000 W / m^2 / K have been measured. The heat transfer coefficient increases with increasing mass flow, increasing inlet vapor quality and increasing heat load. The heat transfer coefficient increases sharply between flow rates of 100 and 175 kg m^{-2} s^{-1} at low inlet vapor qualities and constant heat load. Inaccuracies are mainly a result from the oscillations in measured values.

Pressure drop increases with increasing mass flow and vapor quality. The pressure drop was compared against the homogeneous pressure drop model, two models by Zhang et al. [117] and a recent model by Kim and Mudawar [54]. The pressure drop model by Zhang et al. [117] for gas-liquid flows predicts the pressure drop best when pressure drop is above 0.3 bar. Below this value, the vapor-liquid pressure drop model by the same authors predicts the pressure drop most accurately. When the heat transfer coefficient is set as a function of the pressure drop the relation appears to be of globally linear nature.

Comparison of the heat transfer performance against condensation heat transfer models shows large discrepancies between predictions and measurements ranging. On average the predicted heat transfer coefficient is a factor 5 or 17 larger than the measured heat transfer coefficient. These models are intended to predict condensation heat transfer in a tube. They do not fully take into account the geometric difference of an annulus and possibly more importantly, mass transfer resistance.

5 DESORPTION OF AMMONIA-WATER IN MINICHANNELS

The performance of mini-channels during desorption of ammonia-water mixtures in mini-channels has been experimentally investigated. Measurements have been executed in a channel with a diameter of 1.1 mm and a length of 0.8 m. The mass flux was varied between 150 and 300 kg m^{-2} s^{-1}. The experiments are used to determine the heat transfer coefficient and pressure drop during desorption for different operating conditions along the channel. Results were set out against mass flux and heat load in order to investigate the dependency of heat transfer coefficients and pressure drop on the given variables. Mass flow is directly measured; vapor quality is obtained from equations of state with pressure and temperature at in- and outlet of each channel as input. When possible the experimental results have been compared to models for boiling heat transfer and pressure drop.

This chapter is for a large part based on:

D.M. van de Bor and C.A. Infante Ferreira, *Desorption of ammonia-water in Mini-Channels*, manuscript in preparation.

5.1 Introduction

From chapters 2 and 3 it can be concluded that compression-resorption heat pumps can be an attractive way to increase the energy efficiency of distillation columns in the process industry. Unfortunately, when comparing to the traditional steam boilers with large temperature driving forces, the application of heat pump systems operating with low temperature driving forces requires one or more heat exchangers with a large surface area for heat transfer. On conventional scale, such a heat exchanger can become rather large and costly due to the large amount of materials required. Decreasing the channel size in heat exchangers increases heat and mass transfer performance. Doing so also results in higher heat transfer area per unit of volume which could possibly lead to cost reductions and lower material use.

In the past, many experiments have been done to determine the two phase flow pattern, pressure drop and heat transfer characteristics in mini-channels for (adiabatic) air/water mixtures [25, 37] and refrigerants like CO_2 [24, 82], R-134a [24, 60, 82] and water [10, 86] (non-adiabatic). A variety of models predicting heat transfer coefficients for evaporation of these refrigerants in mini channels are available in literature, but for certain systems they are not in agreement with each other. Very few experiments have been performed with mini-channels using the water-ammonia mixture [20, 21].

Infante Ferreira et al. [42] investigated the performance of absorbers working with the ammonia-water mixture. The absorbers have been tested under adiabatic and diabatic conditions and had tube sizes in the range of 10 to 20 mm with a maximum length of 1 m. From inlet to outlet the flow patterns changed from a froth flow for approximately 20% of the absorber length, to a slug flow for about 65% and finally a bubbly flow for the last 15% of the tube.

Kang et al. [48] analyzed the combined heat and mass transfer for ammonia-water absorption processes and did a parametric analysis on important variables such as heat transfer area on the absorption rate in falling film and bubble mode absorption. In the plate heat exchanger they used, bubble mode absorption rates showed to be almost 50% larger than in falling film mode.

Kim et al. [53] performed a study on a countercurrent slug absorber with low solution flow rates. Like Infante Ferreira et al. [42] they noticed changes in flow pattern from churn flow at the gas inlet to slug flow and to bubbly flow. They noticed that the heat transfer rate is higher during absorption than after the absorption has ended. Absorption length could be influenced by varying flow and thermal conditions. Walls appeared to be fully wetted and no waves were observed on the liquid-vapor interface.

Táboas et al. [98] report on the performance of a plate heat exchanger operating as desorber with an ammonia/water mixture. The plate heat exchanger in their investigation had a plate distance of 2 mm and a hydraulic diameter of 4 mm. Heat transfer coefficients were in the order of 5 to 15 kW m^{-2} K^{-1} for mass fluxes from 50 kg m^{-2} s^{-1} to 140 kg m^{-2} s^{-1} with the trend being increasing heat transfer coefficients with increasing flow rates. The mean vapor quality remained below 0.2. Clearly these geometries allow for large heat transfer coefficients making low temperature driving forces possible. These small temperature driving forces are a must for efficient heat pump designs.

The number of studies specifically dedicated to ammonia-water absorption or desorption in mini-channels is very limited. Determan [20] conducted experiments with a micro-channel falling film
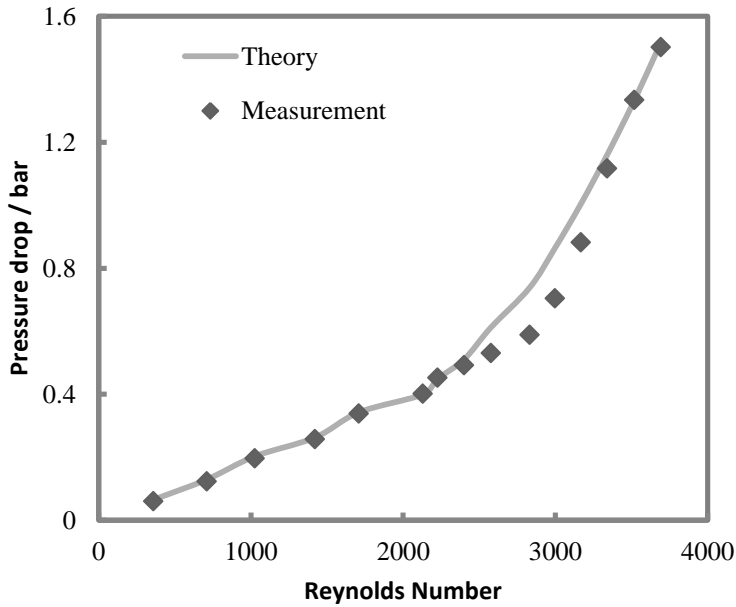
Fig. 5.1. Calibration of tube diameter. For a diameter of 1.08 mm the pressure drop of the experiment matches pressure drop theory. The theoretical line is not entirely smooth because of small fluctuations in operational conditions.

desorber. The main purpose of this research was to capture the effects of the concentrated solution flow rate and the vapor fraction on the desorber heat duty and heat transfer coefficient. The limited number of studies related to the topic identifies the need for additional studies in this field.

The objective of this study is to experimentally investigate the desorption performance of an ammonia/water mixture flowing through a mini-channel with a diameter of 1.1 mm. These results can then be used to design mini-scale heat exchangers for use in heat pumps. The heat transfer coefficient and pressure drop are discussed and set out against mass flux, vapor quality and heat load. Where possible the experimental data is compared with prediction methods for boiling heat transfer and pressure drop. The measurements are done at the industrial conditions of some of the processes of the project partners.

5.2 Experimental Setup and data reduction

The experimental setup is the same setup as described in chapter 4. During the experiments described in chapter 4 the test setup operated with an ammonia-water mixture in the annular side of the heat exchanger and water in the tube side of the heat exchanger. The water in the tube side is replaced by an ammonia-water mixture with a concentration of 0.33 mole per mole to investigate the heat transfer performance of the tube side of the heat exchanger under desorption conditions. By means of pressure drop measurements the diameter of the tube was calibrated to be 1.08 mm, see Fig. 5.1.

The data reduction method is similar to the method described in section 4.3. The tube side is now filled with an ammonia-water mixture. For both sides, the in- and outlet enthalpies can be obtained by assuming that the measured temperature and pressure are at equilibrium conditions. Using the

FluidProp [17] library, the enthalpies and vapor qualities can be obtained as a function of overall ammonia concentration, temperature and pressure, see eqs. (4.3) and (4.4).

The average temperature difference was determined by dividing the heat exchanger in 10 segments with equal heat load. Then the temperature difference was calculated by taking the difference between the equilibrium temperatures of the ammonia/water mixtures on both sides of the tube wall. The resulting temperature differences were averaged over the 10 segments, resulting in the average temperature driving force. The heat transfer area can be obtained from eq. (4.2)

The tube side heat load is obtained by assuming equilibrium conditions at the in- and outlet for the ammonia-water mixture and compared against the shell side heat load assuming equilibrium conditions at the in- and outlet of the test section. The heat load on the tube side is used as actual heat load as most of it is insulated by the shell. The average temperature difference is used to determine the overall heat transfer coefficient. The overall heat transfer coefficient can be calculated from eq. (4.7)

In the coaxial tube heat exchanger under consideration four heat transfer coefficients have to be determined: the overall heat transfer coefficient, the heat transfer coefficient of the wall, the heat transfer coefficient of the ammonia/water mixture in the tube and the heat transfer coefficient of the ammonia/water mixture in the shell. From the experimental data of chapter 4,

$$
hc_{\text{abs}} =
\begin{cases}
453.37 e^{\left[4.4816 \cdot 10^{-5} \cdot \left(\frac{\dot{Q}}{A_O}\right)\right]} & G_{\text{abs}} \leq 150 \\[2mm]
0.2426 \dfrac{\dot{Q}}{A_O} - 8217.9 & for\ 150 < G_{\text{abs}} \leq 175 \\[2mm]
0.3911 \dfrac{\dot{Q}}{A_O} - 17014 & for\ 175 < G_{\text{abs}} \leq 200 \\[2mm]
0.2159 \dfrac{\dot{Q}}{A_O} - 7652.2 & for\ 200 < G_{\text{abs}} \leq 225 \\[2mm]
0.1827 \dfrac{\dot{Q}}{A_O} - 5604.5 & for\ 225 < G_{\text{abs}} \leq 250
\end{cases}
\tag{5.1}
$$

Given the wall thickness, the resistance against heat transfer of the walls is not insignificant. The heat transfer coefficient of the wall can be calculated from eq. (4.11).Then, to obtain the local heat transfer coefficient at the tube side,

$$
\frac{1}{hc_{des}} \frac{d_o}{d_i} = \frac{1}{U_o} - \frac{1}{hc_{w,o}} - \frac{1}{hc_{abs}}
\tag{5.2}
$$

Or rewritten,

$$
hc_{des} = \frac{\dfrac{d_o}{d_i}}{\dfrac{1}{U_o} - \dfrac{1}{hc_{w,o}} - \dfrac{1}{hc_{abs}}}
\tag{5.3}
$$
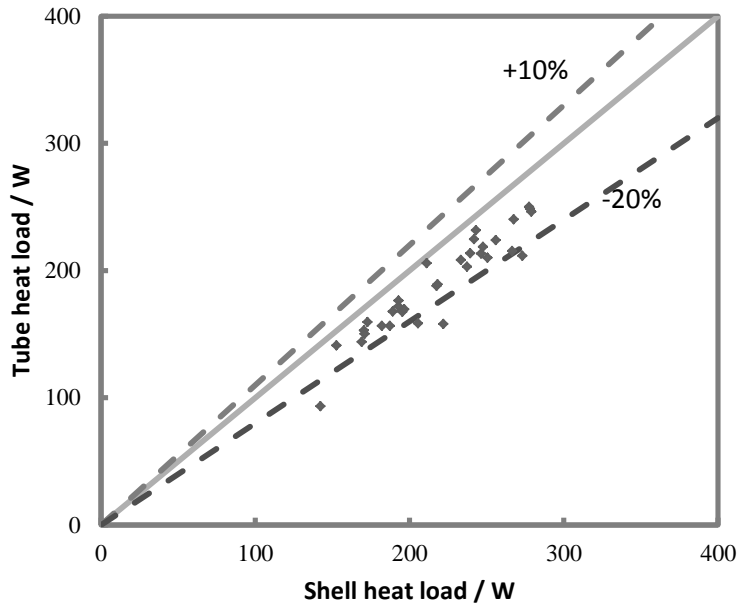
Fig. 5.2. Comparison of the measured heat load on tube and shell sides.

5.3 Results and discussion

This section is divided in 3 subsections. In the first subsection the energy balance is verified. The second subsection discusses the results obtained for the heat transfer coefficient and compares the heat transfer coefficient with literature values. The third subsection gives the pressure drop which is compared with empirical models from literature.

5.3.1 Energy balance and Heat transfer coefficient

The transferred thermal power has been measured on both the tube and shell sides. The difference between the two values indicates the significance of heat losses during the experiments and accuracy of the measurements. Most of the measured points lie within 0 to -20% heat loss, see Fig. 5.2.

The heat transfer coefficients have been obtained using the method described in section 5.2. Application of eqs. (4.2) and (4.7) to the experimental data leads to the overall heat transfer coefficient for different desorber mass fluxes as presented in Fig. 5.3. The inlet temperature set point of the absorber is 180°C in all experiments, while the desorber inlet temperature has a set point of 110°C. Eq. (5.1) can be applied to predict the shell side heat transfer coefficient. This approach results in the desorber side heat transfer coefficients presented as function of mass flux in Fig. 5.4 and as function of heat load in Fig. 5.5
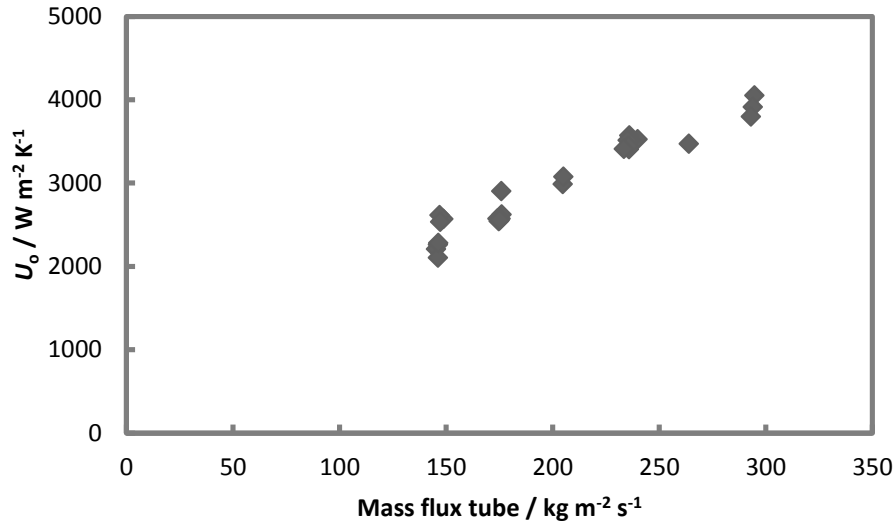
Fig. 5.3. Overall heat transfer coefficient obtained as function of desorption side mass flux.
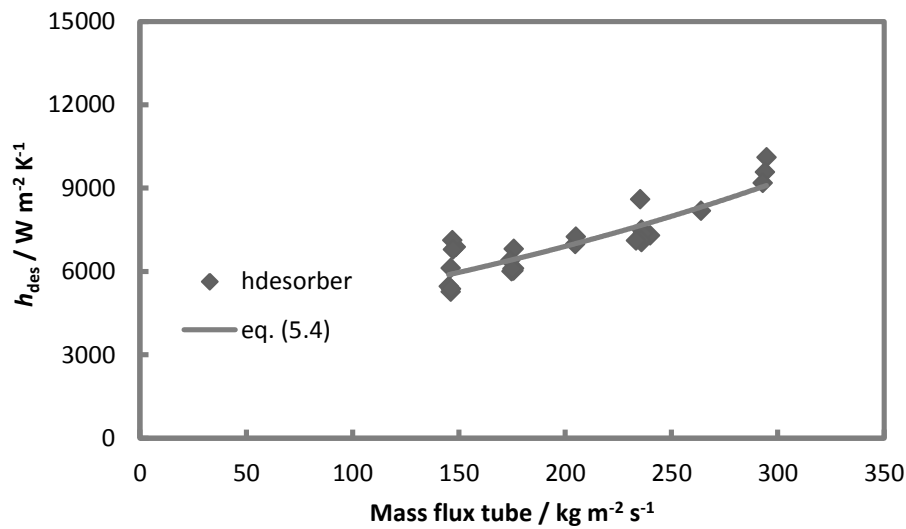
Fig. 5.4. Desorber heat transfer coefficient as function of desorber mass flux based on eqs. (5.1) and (5.3). A larger mass flux results in larger heat transfer coefficients. The solid line represents eq. (5.4)

The heat transfer coefficient can be determined as function of mass flux with reasonable accuracy from

$$hc_{des} = 3852.7e^{0.0029G_{des}} \qquad (5.4)$$

Eq. (5.4) is compared to the experimental data in Fig. 5.4. With slightly lower accuracy, the heat transfer coefficient can also be obtained as function of the heat flux,

$$hc_{des} = 3024e^{1.15\cdot10^{-5}\cdot\frac{\dot{Q}}{A_o}} \qquad (5.5)$$
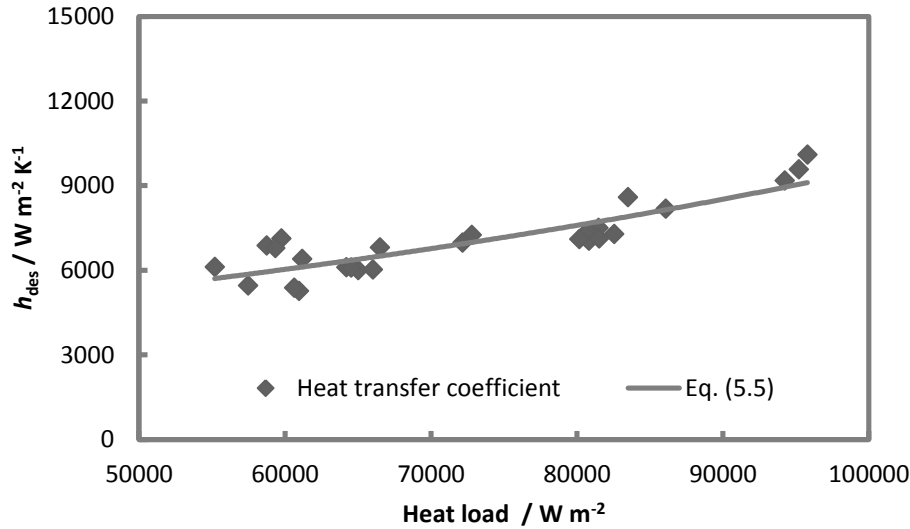
Fig. 5.5. Heat transfer coefficient as function of heat load. Increasing the heat load on the tube increases the heat transfer coefficient. The solid line represents eq. (5.5) and can be used to determine the heat transfer coefficient with reasonable accuracy.
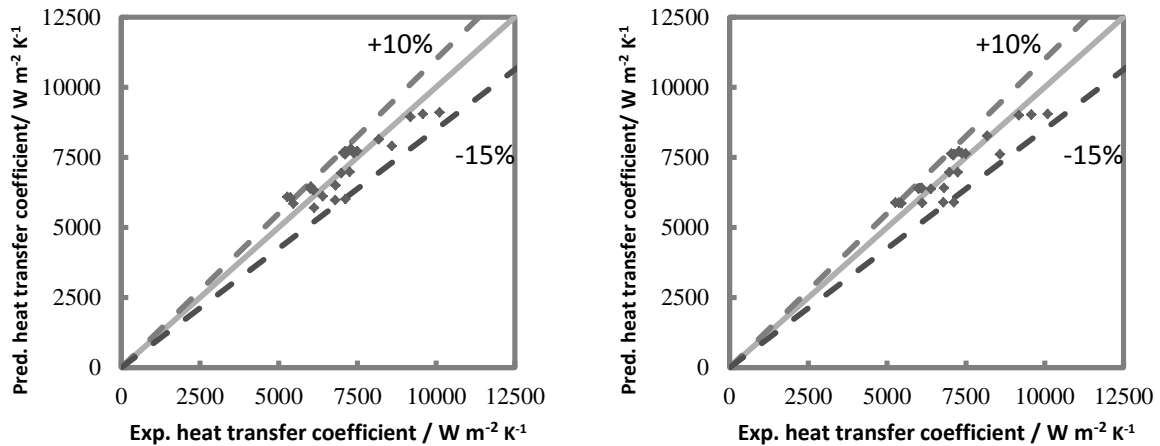
Fig. 5.6. Comparison between predicted heat transfer coefficient (left based on eq. (5.4) and right based on eq. (5.5) and experimentally obtained heat transfer coefficient. Both equations predict the heat transfer coefficient within +10 / -15% accuracy.

Fig. 5.5 shows a comparison between eq. (5.5) and the experimental data. Fig. 5.6 compares the heat transfer coefficient from eq. (5.4), left and eq. (5.5), right, with experimental values. Both equations are able to predict the heat transfer coefficient within +10 / -15%. The latter has a slightly worse root mean square value of 0.756 compared to 0.751 for eq. (5.4).

The results for the heat transfer coefficient have also been compared against a mini channel evaporator model [101]. Although no correlation was found between the model and the data by using the suggested empirical constants [24], arbitrarily changing the empirical constant in the reference heat load from 3328
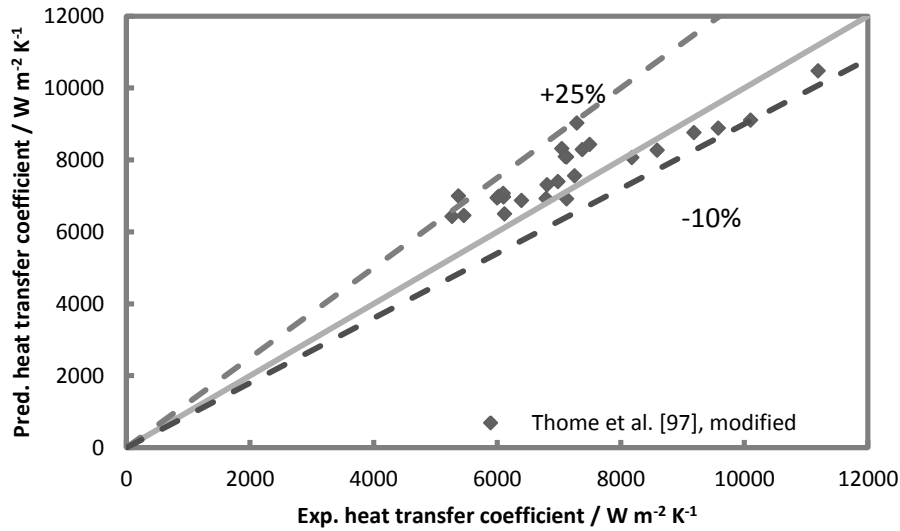
Fig. 5.7. Comparison of the experimental data with the model proposed by Thome, et al. [101] with one modified constant.
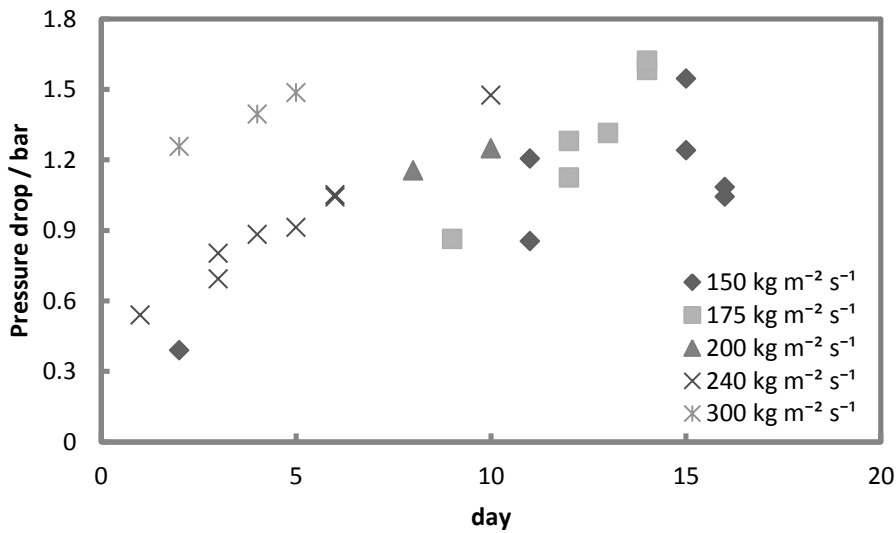
Fig. 5.8. Pressure drop over experimental time for different mass fluxes. In and outlet conditions for a given mass flux deviate only slightly.

to 70000 makes the model able to predict the current experiments with an accuracy between 25% over prediction and 10% under prediction, see Fig. 5.7. Such a model can be more useful to predict heat transfer coefficients for desorption of ammonia-water at conditions far from the currently measured ones.
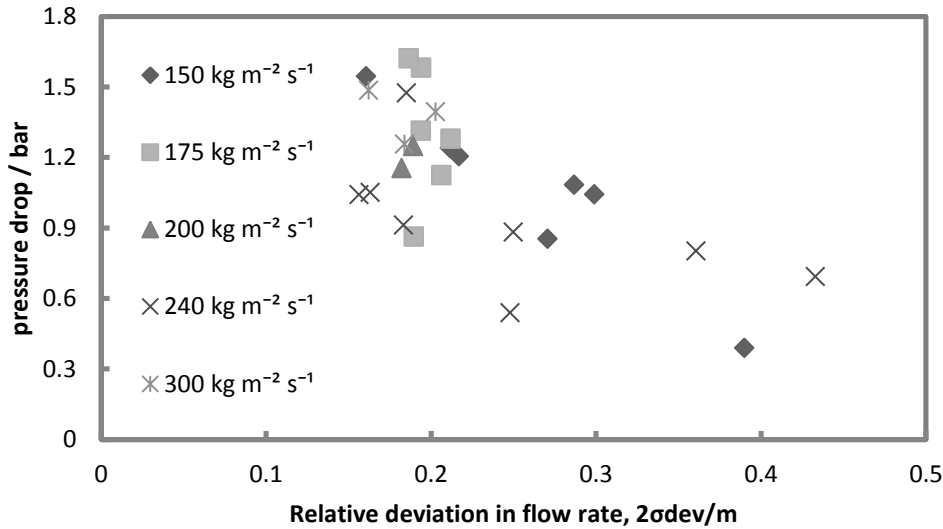
Fig. 5.9. Correlation between pressure drop and relative deviation of flow rate. At lower pressure drop, the oscillation in flow rate is clearly larger.

5.3.2 Pressure drop

Pressure drop is one of the measured variables. Furthermore, in heat pump applications pressure drop could negatively affect the performance of the system and should be minimized. During the experiments there was some buildup of debris inside the tube and at the inlet of the tube. Since such a partial blockage of the tube could have a negative effect on the pressure drop, the measured pressure drop is presented as function of the day that the experiments took place with mass flow as parameter in Fig. 5.8. Clearly, the measured pressure drop increases over time as a result of the ongoing deposition of debris inside the tube. No clear trends can be observed with respect to mass flux or vapor quality. The desorber flow rate appears to become more constant as pressure drop increases. At high pressure drops, flow oscillations around 20% were measured, while at lower pressure drop the oscillations in flow rate could reach up to 45%, see Fig. 5.9.

A comparison with literature [54, 117], as given in Fig. 5.10, confirms that the measured values are unexpectedly high and generally fall outside the inaccuracy of the equations. Furthermore, the pressure drop has been compared against a specialized correlation for flow boiling, [55], to verify that this increased pressure drop is not caused by the desorption process. By comparing Fig. 5.10b and Fig. 5.10c it can be concluded that the correction for flow boiling is small. From Fig. 5.10 it also becomes clear that the deviation between experimental pressure drop and predicted pressure drop becomes larger as time progresses. Given that in the first experiments, for which the tube was still clean, the deviation between the model by Zhang et al. [117] for gas-liquid systems is relatively small, it can be concluded that this model would probably predict experimental results well for a clean tube.

5.4 Conclusion

The experimental heat transfer coefficient for desorption in a 1.1 mm tube has been determined. It varies from approximately 5800 W m^{-2} K^{-1} at a mass flux of 150 kg m^{-2} s^{-1} to 10500 at a mass flux of 300
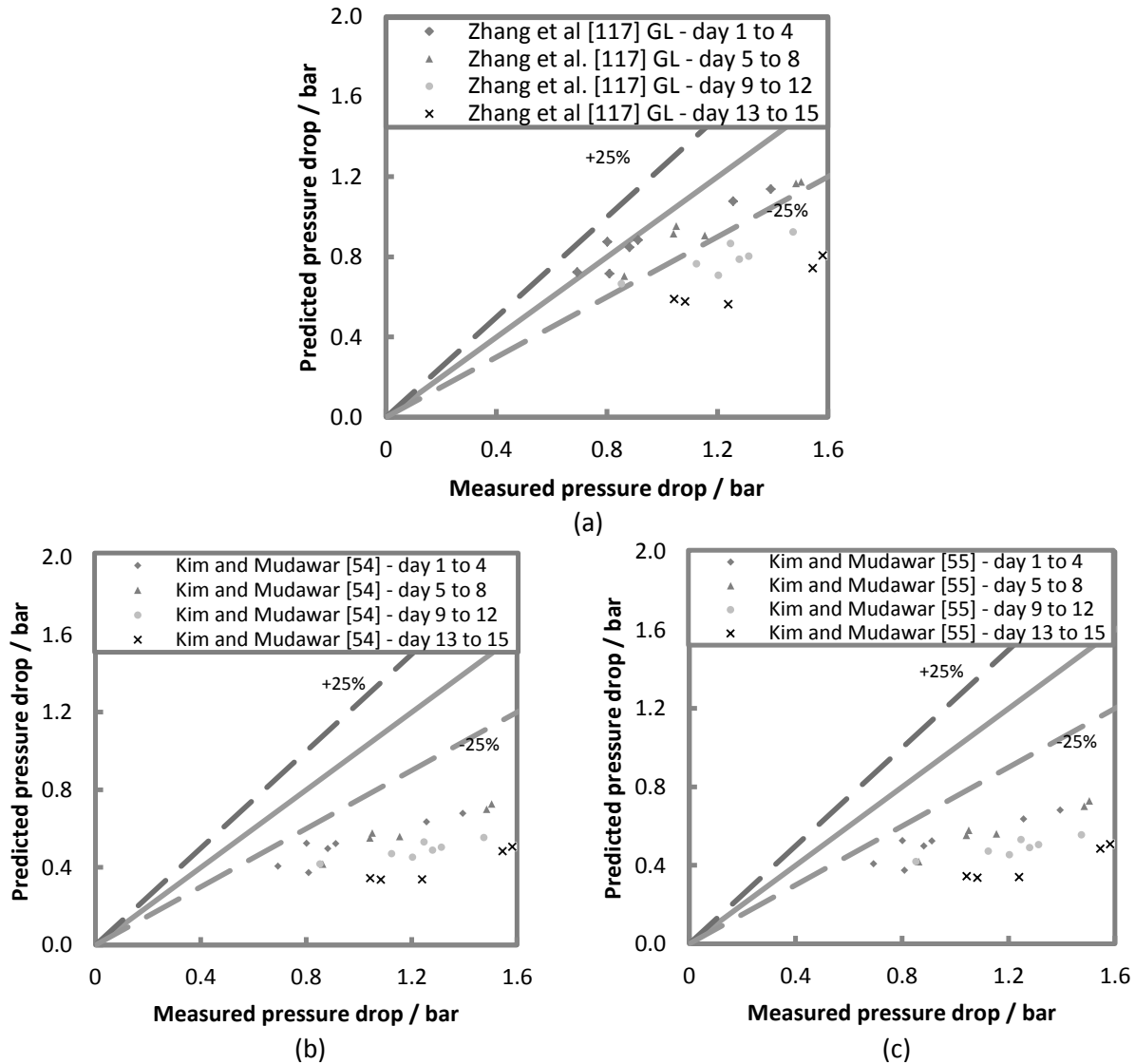
Fig. 5.10. Comparison of experimental pressure drop with literature models for two-phase flows. Since the tube was partially blocked, the under prediction of the pressure drop by the models is expected. a: Comparison with the model by Zhang, et al. [117] for gas-liquid flows. b: comparison of the experimental values with the model by Kim and Mudawar [54] for condensation. c: comparison of the experimental values with a similar model which includes corrections for flow boiling [55].

kg m^{-2} s^{-1}. The obtained correlations for the heat transfer coefficient predict the heat transfer performance within +10% / -15%. The experimental result did show a correlation with a mini-channel flow boiling model after one of the empirical constants in this model was adjusted. Pressure drops up to 1.6 bar were measured but no clear trend could be indicated from the measurements. The inlet of the heat exchanger and the heat exchanger tube became more and more obstructed during the experiments due to the deposition of debris. Comparison with literature shows that pressure drop indeed is larger than predicted, while earlier measurements are in good agreement. Most likely Zhang et al.'s model is able to predict the experiments well for a clean tube. An interesting result of the partial blockage of the tube was the reduction in oscillation of the flow rate.

6 LAMINAR SINGLE PHASE FLOW DISTRIBUTION, PRESSURE DROP AND HEAT TRANSFER IN A MULTI-TUBE MINI-CHANNEL EXCHANGER USING FRACTAL DISTRIBUTION

Mini-channel technology is a promising technology in a world where there is a growing demand for product miniaturization. In this chapter a new geometry for a distributor of a multi-tube mini-channel shell and tube exchanger is described which is tested with water to verify the distribution performance. The flow in the heat exchanger is pure counter current flow; for ease of manufacturing no baffles have been used in the shell. Experimental heat transfer and pressure drop data for laminar single phase water in both the tube and shell side are reported. A mathematical model is developed which can predict the performance of the multi-tube mini-channel that uses the newly proposed distributor. This model considers both heat transfer and pressure drop and makes use of prediction methods proposed in the literature for similar geometries. It has been experimentally validated that the newly proposed distributor gives a good distribution for laminar single phase flows. The mathematical model can predict the experimental performance of the multi-tube mini-channel exchanger within 10% accuracy.

6.1   Introduction

Energy is a fundamental aspect of modern society. The continuous growth and increase in welfare of the world's population is accompanied by an increasing demand for energy. With limited available resources it is crucial to change our way of life to a more energy-efficient and a more sustainable one. The largest portion of the world's energy consumption originates from industry, specifically the chemical industry [56, 83]. Heating and cooling of various process streams hold a large contribution in the energy consumption of the chemical industry. Companies are interested in increasing the efficiencies of their systems without large investments. Mini-channel heat exchangers have a large surface to volume area, which results in a large heat duty and a small material requirement. Therefore the application of mini channels make it possible to increase the efficiency and reduce the investment cost for similar capacities as compared to macro-channel exchangers.

An important aspect which is introduced in a multi-tube exchanger is the flow distributor. Not only could the flow distributor contribute significantly to the pressure drop of a heat exchanger, it also determines the relative mass flow to each tube [30]. Due to the smaller geometries of mini-channels, the distributors require more compact designs. Fractal distributors have a compact design due to the high distribution point density [51] and well-designed fractal distributors have equal flow resistances to each end point. Another advantage of fractal distributors is that all the flow paths are hydraulically equivalent e.g. the pressure drop to each individual flow path is the same while the mass flows are approximately equal. By having an equal flow in each tube the temperature driving forces in a heat exchanger can be reduced because all tubes would operate with equal flow, heat transfer coefficient and heat load.

Quite some work has been published in the field of fractal distribution for cooling and heating systems [65, 67, 70]. Haller et al. [35] numerically investigated the pressure loss and heat transfer characteristics of fractal networks in micro-channels. Different flow geometries were investigated using a single phase laminar water flow. Chen and Cheng [14] studied the heat transfer performance of a newly proposed fractal distributor that is based on the fractal pattern of mammalian and respiratory systems. Stronger heat transfer capabilities and a lower pumping power were calculated for the newly proposed fractal distributor. The effect of the Svelteness number in the design of fractal distributor is investigated by Ghaedamini et al. [30]. Using numerical simulations it was concluded that the Svelteness number is an important design parameter to consider for fractal distributors. Wang et al. [109] investigated the relative importance of pressure drop contributions as function of the Svelteness number. It was concluded that in geometries with Svelteness numbers higher than 10, the pressure drop due to local junctions can be neglected with respect to the pressure drop caused by wall friction.

In the present chapter a newly proposed design of a fractal distributor for a multi-tube mini-channel heat exchanger for single phase laminar flows is discussed. The distributor is originally designed to work with laminar two-phase flows, but the performance of the distributor is first evaluated for laminar single phase flows to validate the distribution under more simple flow conditions. Experiments have been conducted where laminar single phase water was used as the heat transfer medium in both the tube and shell sides. The heat exchange section of the multi-tube mini-channel exchanger has a shell side diameter of 21 mm and hydraulic diameter of 1.8 mm. The heat exchanger holds 116 tubes of 681 mm

Fig. 6.1. Side view of the multi-tube mini-channel heat exchanger. Shell side internal diameter is 21 mm.
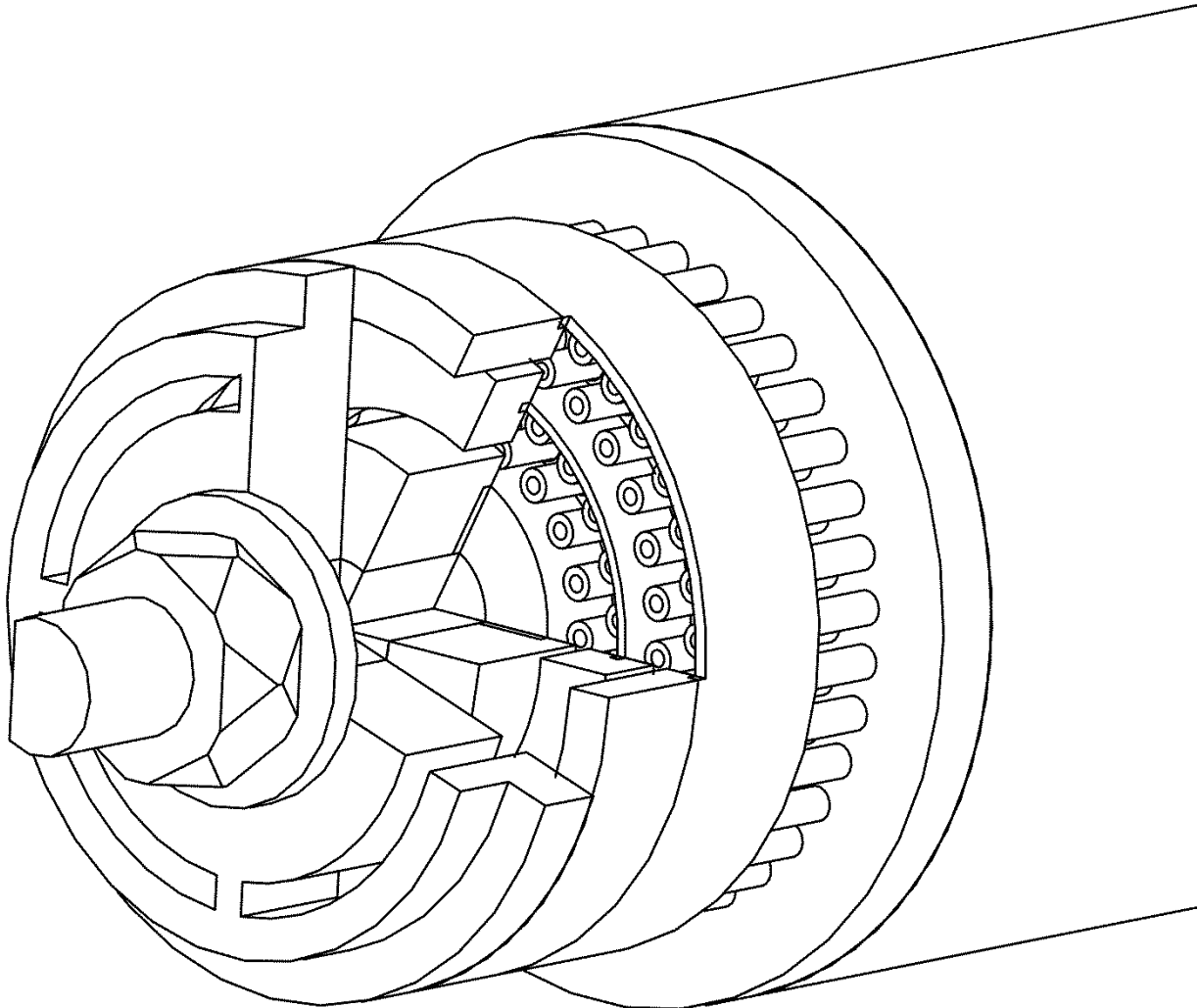
Fig. 6.2. 3D view of the tube flow distributor. Part of the shell side distributor is visible behind the tube side distributor.

length with an external diameter of 1 mm and an internal diameter of 0.5 mm. A side view of the multi-tube mini-channel heat exchanger is shown in Fig. 6.1. The geometry of the distributors is identical to the geometry of the collectors. Laminar counter current operating conditions are used during the experiments. The experiments have been performed with a vertical arrangement of the exchanger. The first goal of this research is to measure and evaluate the quality of the distribution. Secondly this research is aimed at identifying the heat transfer and pressure drop characteristics of single phase water flows in the multi-tube mini-channel heat exchangers, which use the newly proposed fractal distributor, and compare these to a mathematical model.
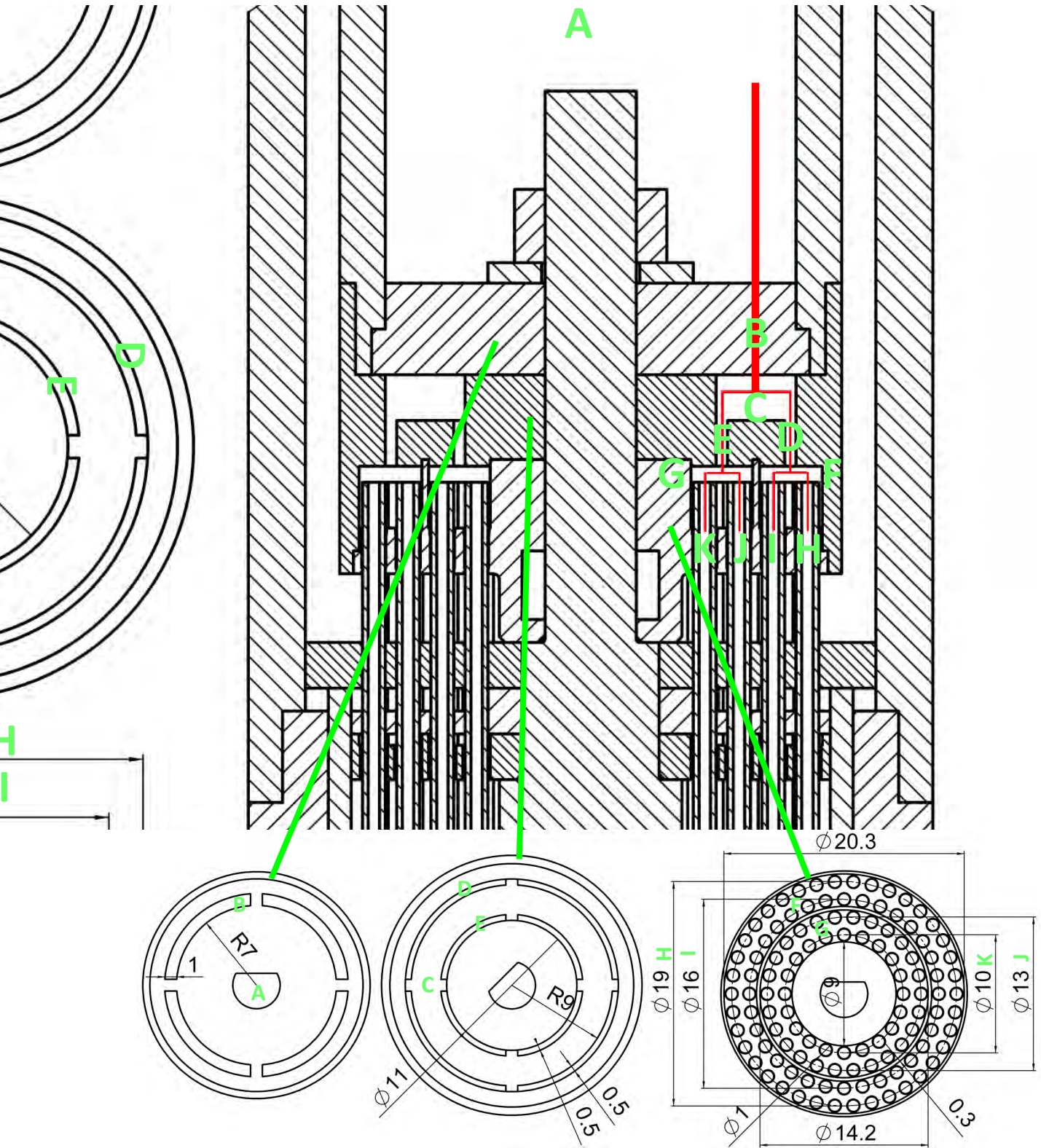
Fig. 6.3. Cross-sectional view of newly proposed fractal distributor for the use in multi-tube mini-channel exchangers. Bottom left to right: First distributor plate, second distributor plate, third distributor plate. The thick line indicates the different flow paths of the tube side.
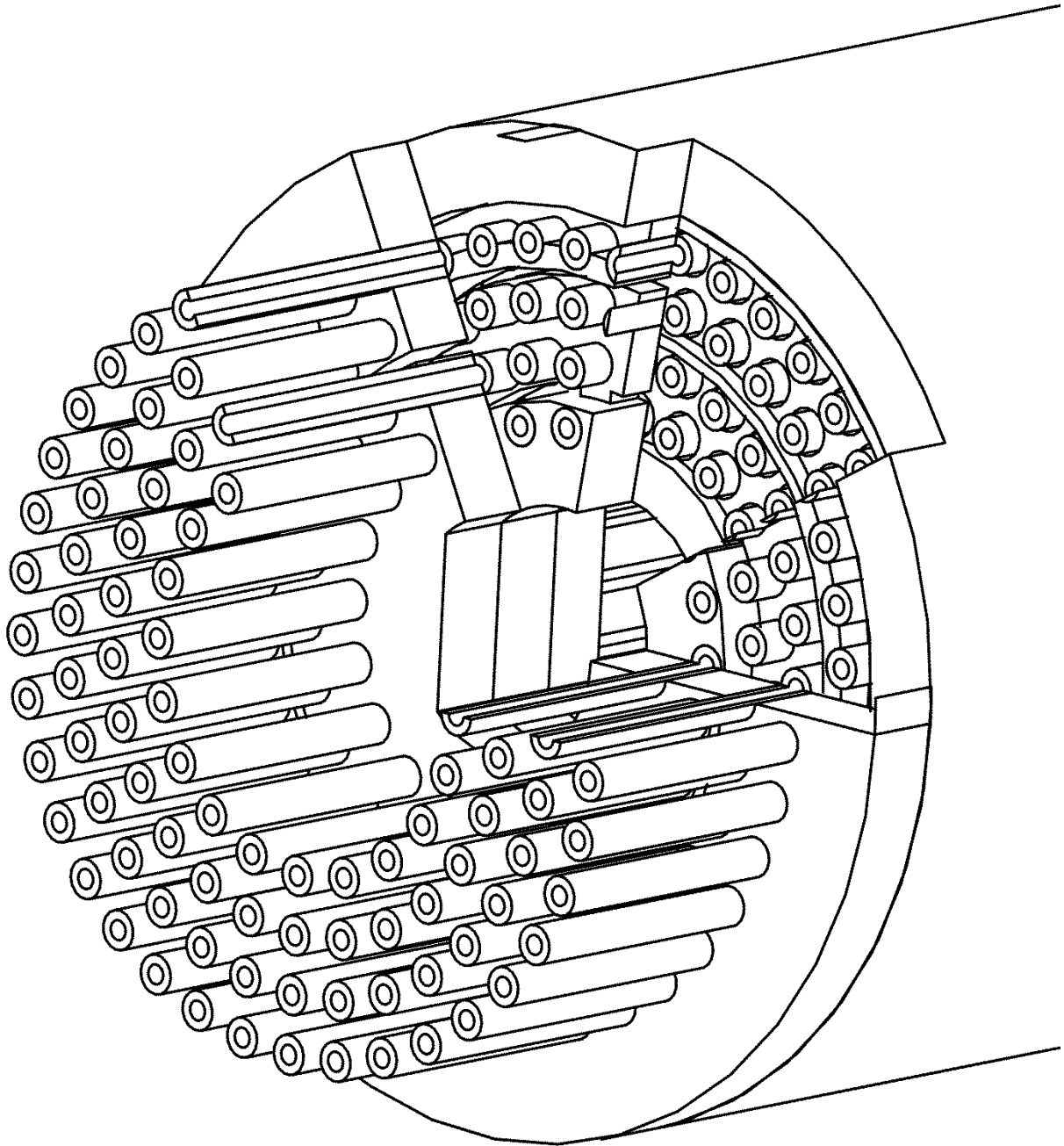
Fig. 6.4. 3D cut out view of the shell side distributor. The tube side distributor is removed.

6.2 Fractal distribution

A 3D view and a cross-sectional view of the newly proposed fractal distributor for the use in multi-tube mini-channel exchangers are shown in Fig. 6.2 and Fig. 6.3. In this figure the flow paths of the tube side flow are schematically indicated. The letters indicate the different sections of the flow paths the fluid can take in the tube side. The geometry of the collector is identical to the geometry of the distributor for both the tube and shell sides. The tube side flow is distributed over 116 tubes using three different distributor plates. Starting in section A, the fluid flows through the first distributor plate (B). The purpose
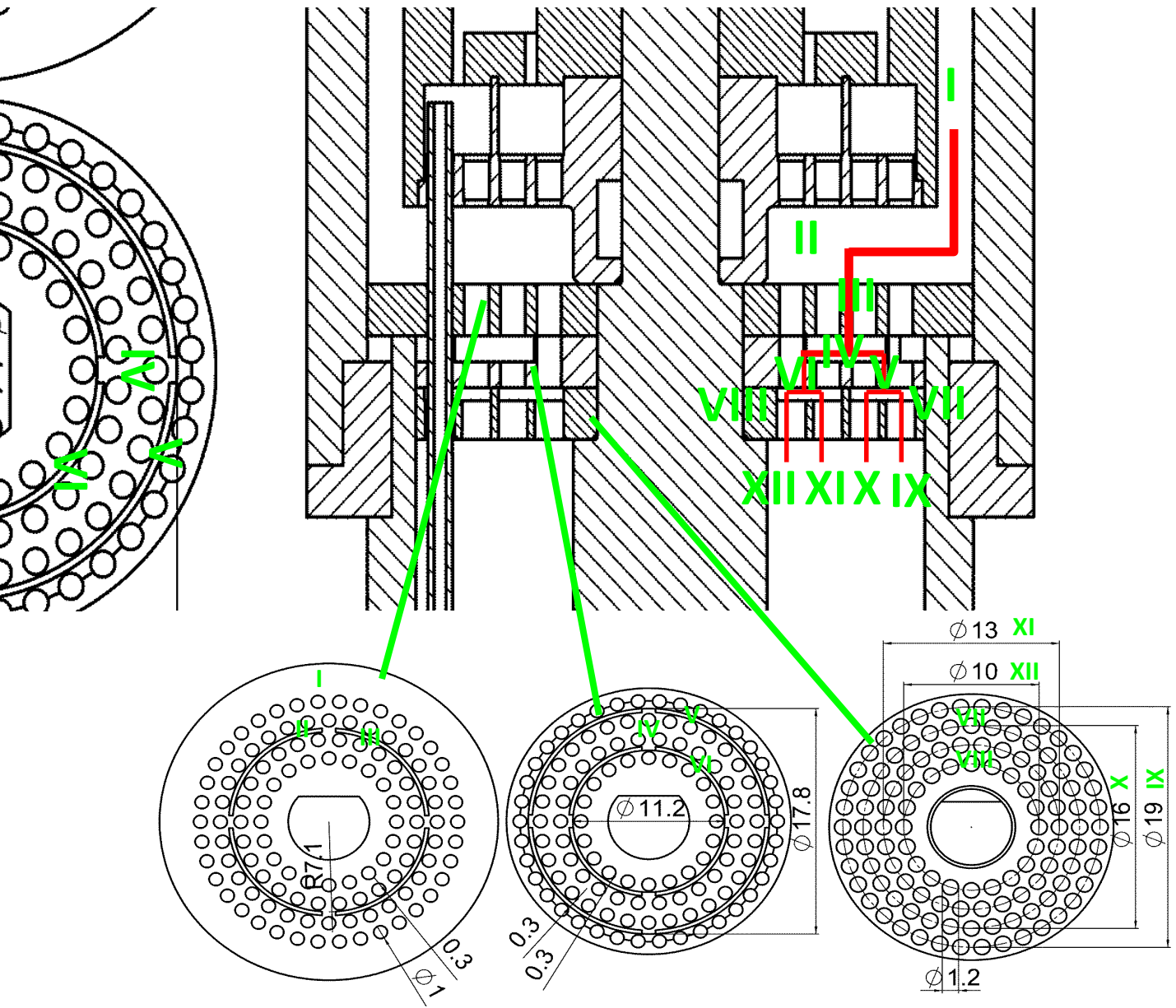
Fig. 6.5. Cross-sectional view of newly proposed fractal distributor for the use in multi-tube mini-channel exchangers. Bottom left to right: First distributor plate, second distributor plate, third distributor plate. The thick line indicates the different flow paths of the shell side.

of this distributor plate is to channel the flow in such a way that the fluid approximately hits the second distributor plate on the middle ring plate (C). At the second distributor plate, the fluid is separated into two different streams. The fluid can either flow through the outer ring (D) or the inner ring (E). The fluid then reaches the final distributor plate (F/G), which holds the 116 mini-channel tubes and here the fluid is separated from 2 different streams to 116 different streams (H/I/J/K). To further clarify the geometry of the distributor, section H contains 38 tubes, section I contains 32 tubes, section J contains 26 tubes and section K contains 20 tubes.

Table 6.1. Svelteness numbers of the prototype heat exchanger.

Section	Svelteness number [-]
Distributor/Collector tube side	4.1
Distributor/Collector shell side	4.0
Total tube side geometry	23.8
Total shell side geometry	15.5

In Fig. 6.4 and Fig. 6.5 the same fractal distributor is presented with an indication of the shell side flow. The purpose of the shell side distributor is to create a good initial wetting of the tubes. To increase the visibility of the shell side distributor, most tubes are not shown in this figure. Starting in section I the shell side flow enters the distributor (I). The fluid flow is then perpendicular to the tubes (II) and reaches the first shell side distributor plate (III). The purpose of this distributor plate is similar to the purpose of the first distributor plate of the tube side. The fluid is channelled in such a way that it hits the second distributor plate on the middle section (IV). At the second distributor plate, the fluid can either go through the outer ring (V) or the inner ring (VI). The shell side flow is now separated from one single flow to two different flows (VII/VIII). The diameter of the holes in the first and second distributor plate is the same as the outer diameter of the tubes. The shell side fluid can therefore not flow between the tubes and the distributor plates. Finally the fluid reaches the third distributor plate and here the diameter of the holes is slightly larger than the outer diameter of the tubes i.e. the fluid can flow between the tubes and the distributor plate. This should distribute the shell side flow evenly over all the 116 tubes and give a good initial wetting of the tubes.

6.3 Mathematical model

6.3.1 Pressure drop

The total pressure drop of the multi-tube mini-channel exchanger is dependent on the pressure drop in the distributor, collector and the pressure drop in the heat exchange section.

$$\Delta P_{tube,tot} = \Delta P_{tube,distr} + \Delta P_{tube,HES} + \Delta P_{tube,col} \tag{6.1}$$

$$\Delta P_{shell,tot} = \Delta P_{shell,distr} + \Delta P_{shell,HES} + \Delta P_{shell,col} \tag{6.2}$$

In the distributor and collector the pressure drop is not only caused by frictional wall effects, but pressure is also lost due to the redirection of the fluid flow. Momentum is lost since the fluid has to go through bends, contractions and expansions. The relative importance between the frictional losses and losses due to the redirections of the fluid can be analysed using the dimensionless Svelteness number as discussed by Ghaedamini et al. [30].

Table 6.2. Different flow paths in the distribution network of the tube side.

Flow paths	Sections in flow paths
Outer flow path	Inlet – A – B – C – D – F – H
Third flow path	Inlet – A – B – C – D – F – I
Second flow path	Inlet – A – B – C – E – G– J
Inner flow path	Inlet – A – B – C – E – G – K

$$Sv = \frac{\text{external flow length scale}}{\text{internal flow length scale}} \qquad (6.3)$$

The Svelteness numbers for the geometry of the prototype multi-tube mini-channel exchanger are given in Table 6.1. If the Svelteness number is higher than 10 then the momentum losses due to the redirections of the fluid can be neglected as stated by Wang et al. [109]. This means that in the distributor and collector the frictional losses are just as important as the local junction losses. For the total tube side or shell side geometry, the pressure drop can be determined by the frictional pressure drop losses only. Logically this means that the pressure drop of this exchanger can be modelled by the frictional pressure drop losses only. However the local junction losses in the tube side distributor are necessary in the numerical model, since the local pressure drop in the tube side distributor determines the relative mass flow to each individual tube. For the shell side a perfect distribution is assumed in the numerical model. If the results from the numerical model agree with the experimental results then the fluid will probably be evenly distributed over the tubes. A poor distribution reduces the heat transfer performance of a multi-tube exchanger and it is reasonable to assume that the comparison between the heat transfer performance predicted by the numerical model and the experimental results can be used to validate the assumption that the flow is evenly distributed in the shell side. Since the pressure drop in the distributor and collector are negligible compared to the frictional pressure drop in the heat exchange section, the total pressure drop of the tube and shell sides are:

$$\Delta P_{tube,tot} = \Delta P_{tube,HES} \qquad (6.4)$$

$$\Delta P_{shell,tot} = \Delta P_{shell,HES} \qquad (6.5)$$

The pressure drop of each flow path in the tube side distributor is required for the relative mass flow in each tube. The pressure drop of the flow paths in the tube side distributor is modelled as a series of expansions, contractions, tube flows and annuli flows.
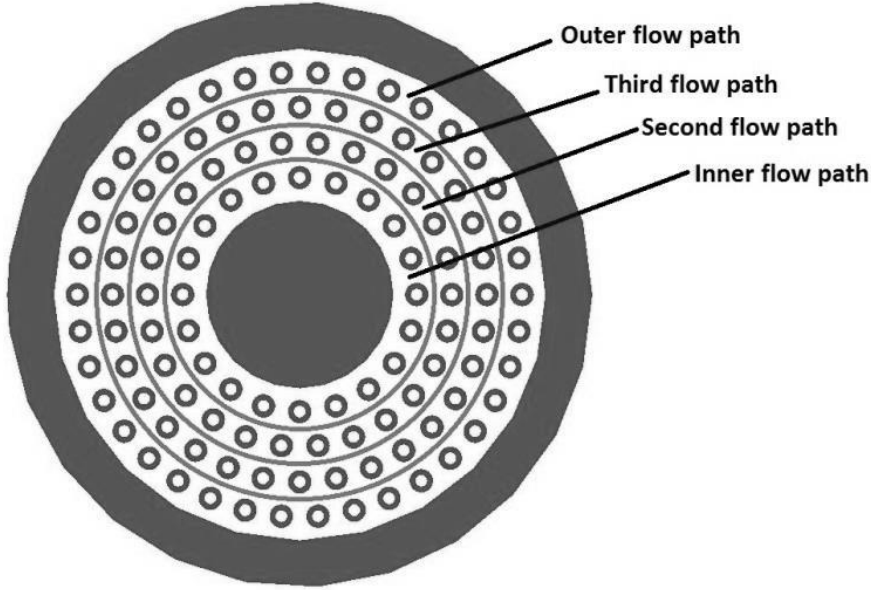
Fig. 6.6. Schematic indication of different flow paths of the multi-tube mini-channel exchanger.

$$\Delta P_{tube,fp} = \sum \Delta P_{tube,fp,s} + \sum \Delta P_{tube,fp,sc} \qquad (6.6)$$

As shown in Fig. 6.3 and Fig. 6.5, there are four different flow paths the fluid can take in the tube side. The tube side and shell side flows are therefore divided into four different flow paths as indicated in Fig. 6.6. Using the symbols from Fig. 6.3 and Fig. 6.5, the different sections of the four tube side flow paths are listed in Table 6.2. The sections which are modelled as a tube flow are: Inlet, A, H, I, J and K. The sections which are modelled as an annular flow are: B, C, D, E, G and F. The flow is contracted at the section changes: A/B, C/D, C/E, G/H, G/I,F/J and F/K. The flow is expanded at the section changes: Inlet/A, B/C, D/G and E/F. The pressure drop of a single phase fluid flow through an expansion or contraction in a mini-channel is modelled using the equations proposed by Chalfi and Ghiaasiaan [12].

$$\Delta P_{exp} = K_{exp}\rho\frac{u^2}{4} - \rho\frac{u^2}{2}(1 - \sigma^2) \qquad (6.7)$$

$$\Delta P_{con} = K_{con}\rho\frac{u^2}{2} + \rho\frac{u^2}{2}(1 - \sigma^2) \qquad (6.8)$$

With σ the flow area ratio. The velocities are based on the smaller area and the loss coefficients for expansion and contraction are calculated from:

$$K_{exp} = 0.8 \qquad (6.9)$$

$$K_{con} = 0.0588\ln(Re) + 0.0218 \qquad (6.10)$$

Since the flow lengths are relatively short in the distributor, the developing region of the laminar flow is taken into account in the pressure drop calculations of the flow path sections. The frictional pressure

drop of a laminar single phase flow in a tube in the developing region is modelled by the relation described by Kandlikar [47]:

$$\Delta P_{tube,dev} = \rho \frac{u_{tube}^2}{2} \left(13.74(z^+)^{0.5} + \frac{1.25 + 64z^+ - 13.74(z^+)^{0.5}}{1 + 0.00021(z^+)^{-2}} \right) \qquad \text{(6.11)}$$

The dimensionless length and developing length are given by:

$$z^+ = 0.0565 \qquad \text{(6.12)}$$

$$L_{dev,tube} = 0.0565 d_{H,tube} Re_{tube} \qquad \text{(6.13)}$$

The frictional pressure drop of a fully developed laminar single phase flow in a tube is calculated by:

$$\Delta P_{tube,fd} = f_{tube} \rho \frac{u_{tube}^2}{2} \frac{L_{tube} - L_{dev,tube}}{d_{H,tube}} \qquad \text{(6.14)}$$

$$f_{tube} = \frac{64}{Re_{tube}} \qquad \text{(6.15)}$$

The frictional pressure drop of a fully developed single phase laminar flow in an annulus is modelled by:

$$\Delta P_{ann,fd} = f_{ann,fd} \rho \frac{u_{ann}^2}{2} \frac{L_{ann} - L_{ann,dev}}{d_{H,ann}} \qquad \text{(6.16)}$$

$$f_{ann,fd} = \frac{64}{Re_{ann}} \qquad \text{(6.17)}$$

$$Re_{ann} = Re \frac{(1 + R^{*2}) \ln(R^*) + (1 - R^{*2})}{(1 - R^{*2}) \ln(R^*)} \qquad \text{(6.18)}$$

$$R^* = \frac{r_{tube,o}}{r_{shell,i}} \qquad \text{(6.19)}$$

The developing region of the single phase laminar flow in an annulus is modeled using the equations proposed by Gupta and Garg [33].

$$\Delta P_{ann,dev} = \rho \frac{u_{ann}^2}{2} \left[K_{ann,dev} + \frac{L_{ann,dev}}{d_{H,ann}} f_{ann,dev} \right] \qquad \text{(6.20)}$$

The developing length, pressure drop parameter K and the friction factor in the developing region are numerically calculated and listed in Gupta and Garg [33].The total pressure drop of the shell side flow is only dependent on the frictional pressure drop in the heat exchange section of the shell side. This pressure drop is calculated using:

$$\Delta P_{shell} = f_{shell} \rho \frac{u_{shell}^2}{2} \frac{L_{shell}}{d_{H,shell}} \qquad \text{(6.21)}$$

The friction factor is determined using the Reynolds analogy. The results of obtained by Mahulikar and Herwig [68] are used to determine the friction factor. In this chapter, the change in fluid properties is taken into account in the conservation of momentum, which is used in the derivation of the friction factor. For the operating conditions during the experiments, the effective friction factor is:

$$f_{shell} = 22 \tag{6.22}$$

6.3.2 Heat transfer

In the numerical model it is assumed that no heat transfer takes place in the distributor and collector. Also the assumption is made that no heat is lost to the environment. It has been experimentally verified that the heat losses to the environment are smaller than 5%. The overall heat transfer coefficient of the heat exchanger section is:

$$\frac{1}{U_O} = \frac{1}{hc_{shell}} + \frac{d_{o,tube} \ln\left(\frac{d_{o,tube}}{d_{i,tube}}\right)}{2\lambda_w} + \frac{d_{o,tube}}{d_{i,tube}} \frac{1}{hc_{tube}} \tag{6.23}$$

The heat transfer coefficients of the shell and tube sides are calculated using the Nusselt numbers:

$$hc_{tube} = Nu_{tube} \frac{\lambda_{tube}}{d_{H,tube}} \tag{6.24}$$

$$hc_{shell} = Nu_{shell} \frac{\lambda_{shell}}{d_{H,shell}} \tag{6.25}$$

The Nusselt number for a laminar single phase tube flow is modeled using the approach of Sparrow and Patankar [94]. In this study, the Nusselt number is related to the Biot number where it can range between the constant heat flux condition (Nu_{tube} = 4.344) and constant wall temperature condition (Nu_{tube} = 3.66). This dependency of the Nusselt number with the Biot number is listed in [94]. The Nusselt number for a laminar single phase flow along a tube bundle is modeled using the approach of Miyatake and Iwashita [75].

$$Nu_{shell} = (c^2 + d^2 Gz^{2/3})^{1/2} \tag{6.26}$$

$$c = \frac{3.1\alpha^{0.1} + 324\alpha^{16}}{1 + 69.5\alpha^{24}} \tag{6.27}$$

$$d = \frac{1.536(1 + 8.24\alpha^{0.39})}{\left(2\sqrt{3}\beta^2 - \pi\right)^{1/3}(1 + 6.37\alpha^{0.73})} \tag{6.28}$$

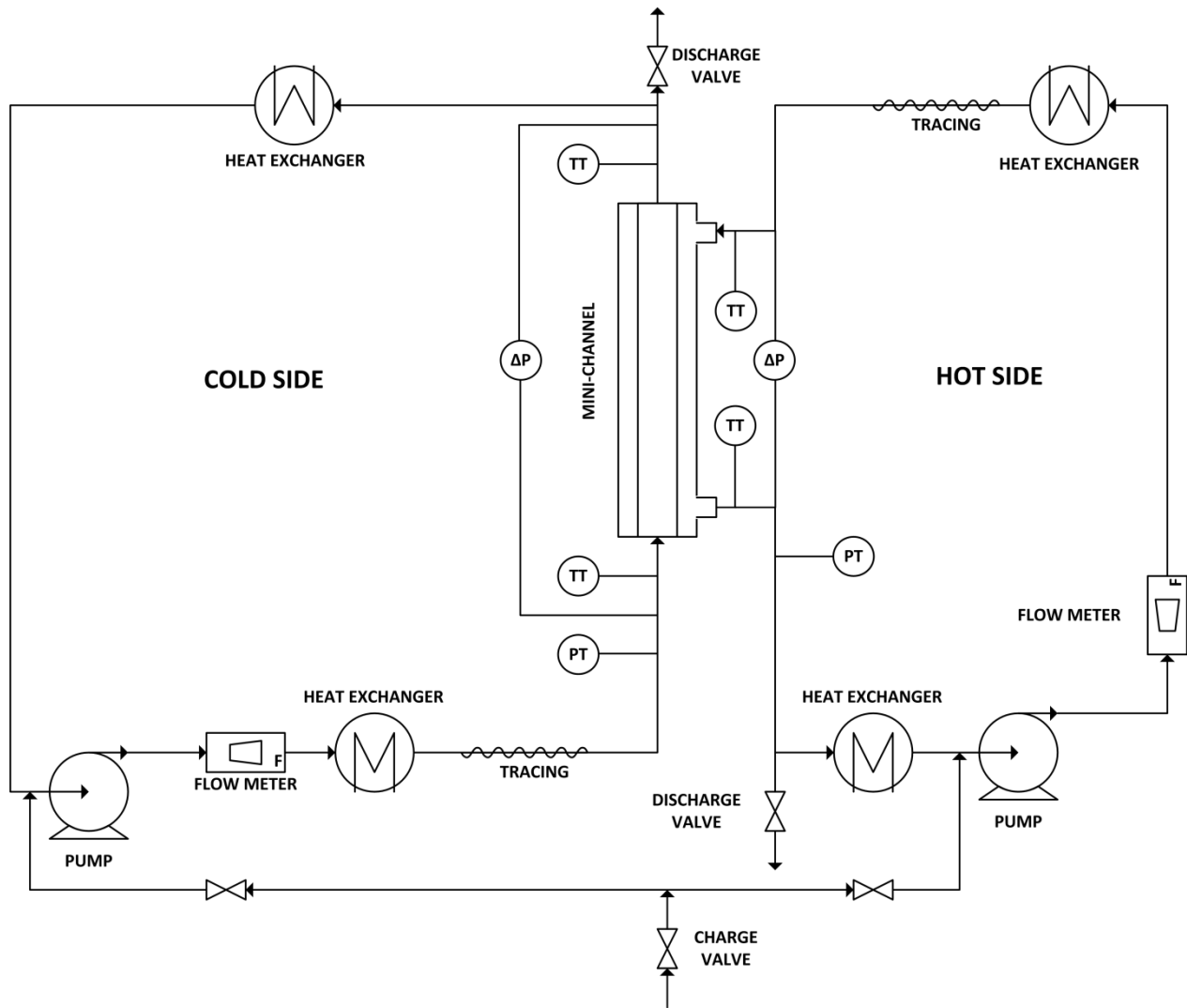**Fig. 6.7. Experimental setup used to measure the pressure drop and heat transfer performance of the multi-tube mini-channel exchanger.**

The local Graetz number, pitch-to-tube diameter ratio and dimensionless spacing between tubes are defined as:

$$Gz = \frac{\dot{m}_{shell} C_p}{N \lambda_{shell} z} \qquad (6.29)$$

$$\beta = \frac{2p}{d_{o,tube}} \qquad (6.30)$$

$$\alpha = \beta - 1 \qquad (6.31)$$

6.3.3   Solution algorithm

The numerical model uses the experimental inlet conditions of both shell and tube side as initial values for the inlet and outlet conditions of the exchanger model. The number of control volumes is 5000 and the model starts with a linear temperature profile in the tube side. The four tube flow paths of the shell side and tube side are alternately computed and the numerical model is iterated until the mean relative error of the heat flux between the shell side and tube side is less than 1%. The programming environment used to solve the proposed numerical model is Matlab R2012a [100].

6.4   Experimental setup and data reduction

6.4.1   Setup

The experimental setup used for the experiments is shown in Fig. 6.7. The multi-tube mini-channel exchanger is placed vertically and the shell side flow enters from the top and the tube side flows enters from the bottom, creating a counter-current flow. Both the shell side and tube side flows are preheated using a thermostatic bath and then they are heated to their desired temperature using electrical tracing. The flows are driven by two magnetically coupled positive displacement pumps. The pump's flow rate is controlled using a Coriolis based flow meter. The temperatures of both flows are measured in both ends of the exchanger using PT-100 temperature sensors. The differential pressure is also measured for both sides of the exchangers by Sitrans P DS III pressure sensors. Sitrans P DS III pressure sensors are also used to measure the pressures in the bottom of the exchanger. Measurements have been taken over a time-span of half an hour with a sampling frequency of 0.5 Hz. The experimental conditions have been selected to reproduce the operating conditions of a compression-resorption heat pump integrated with a distillation process. The operating temperatures range from 100 °C to 160 °C. During single phase flows measured inlet temperatures remained within ± 0.5 K from their average value.

6.4.2   Pressure drop and overall heat transfer coefficient

The pressure drop of the exchanger can directly be obtained from the experimental data using the differential pressure sensor. The overall heat transfer coefficient is defined by:

$$U_O = \frac{\dot{Q}}{A_O \Delta T} \tag{6.32}$$

Where the contact area is defined by:

$$A_O = \pi d_{o,tube} N L \tag{6.33}$$

The total heat that is transferred between the inlet of the exchanger and the outlet is retrieved from:

$$\dot{Q} = \dot{m}_{shell} \bar{C}_p \left(T_{shell,i} - T_{shell,o} \right) \tag{6.34}$$
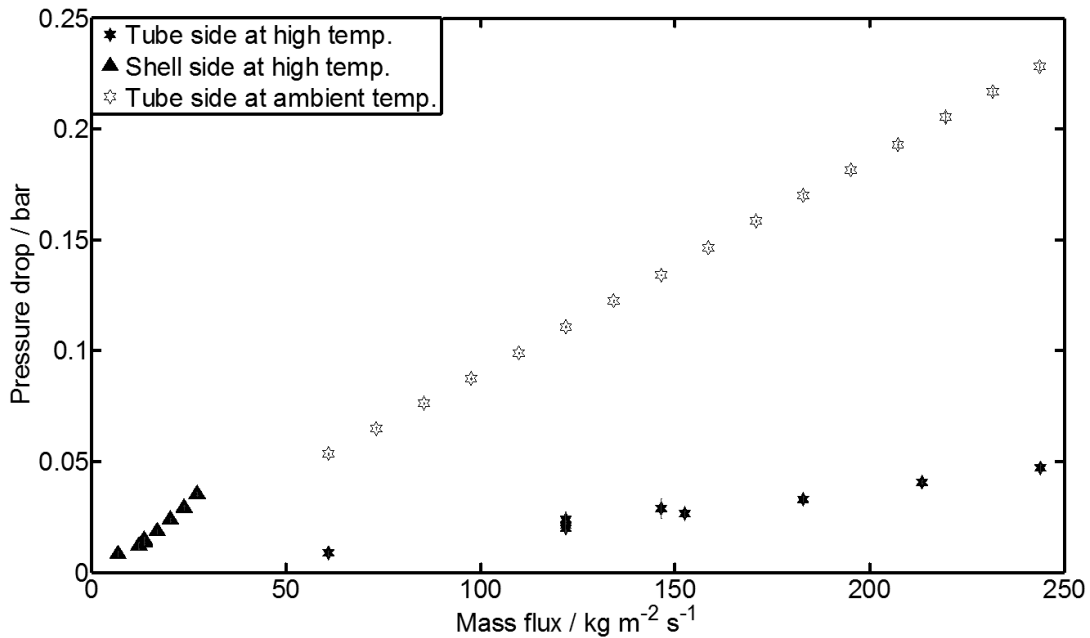
Fig. 6.8. Experimental pressure drop results for single phase water in both the tube and shell sides.

The isobaric heat capacity is estimated to be the mean isobaric heat capacity of the temperature range of the experiments, which is 100°C to 160°C. This equals

$$\bar{C}_p = 4262 \frac{J}{kgK} \tag{6.35}$$

When the tube side of the heat exchanger is filled with water, the tube side Nusselt number can be directly determined from laminar flow theory as function of the Biot number [94].

$$hc_{tube} = Nu_{tube} \frac{\lambda_{water}}{d_{H,tube}} \tag{6.36}$$

Using the tube side heat transfer coefficient it is possible to determine the shell side heat transfer coefficient. The shell side heat transfer coefficient can then be calculated from

$$hc_{shell} = \left(\frac{1}{U_o} - \frac{d_{o,tube}}{hc_{tube} d_{i,tube}} - \frac{d_{o,tube} ln\left(\frac{d_{o,tube}}{d_{i,tube}}\right)}{2\lambda_w} \right) \tag{6.37}$$
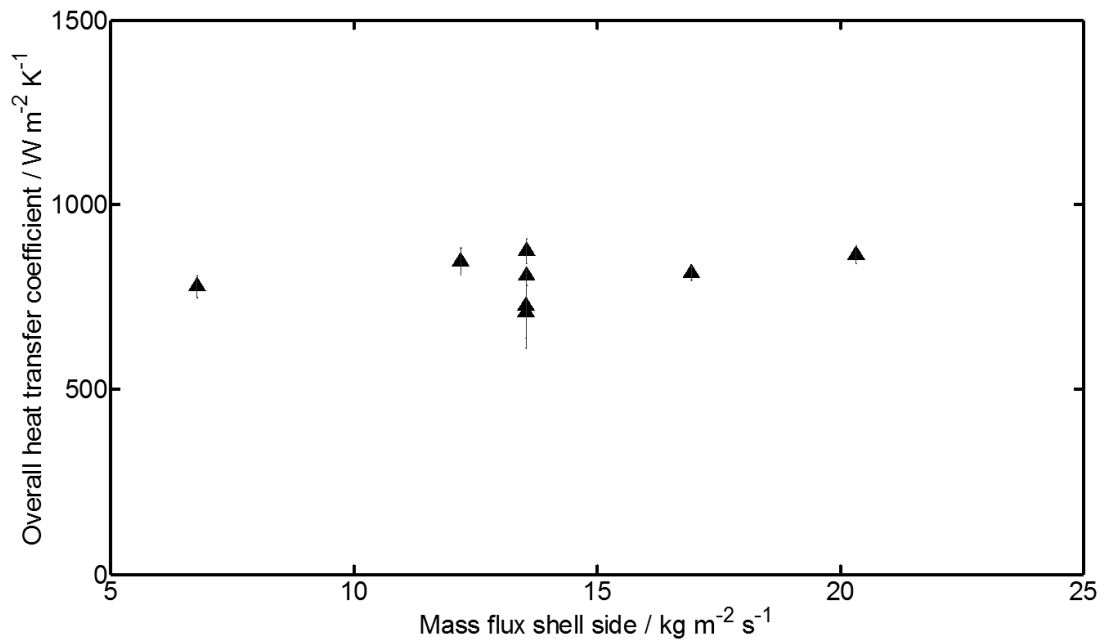
(a)
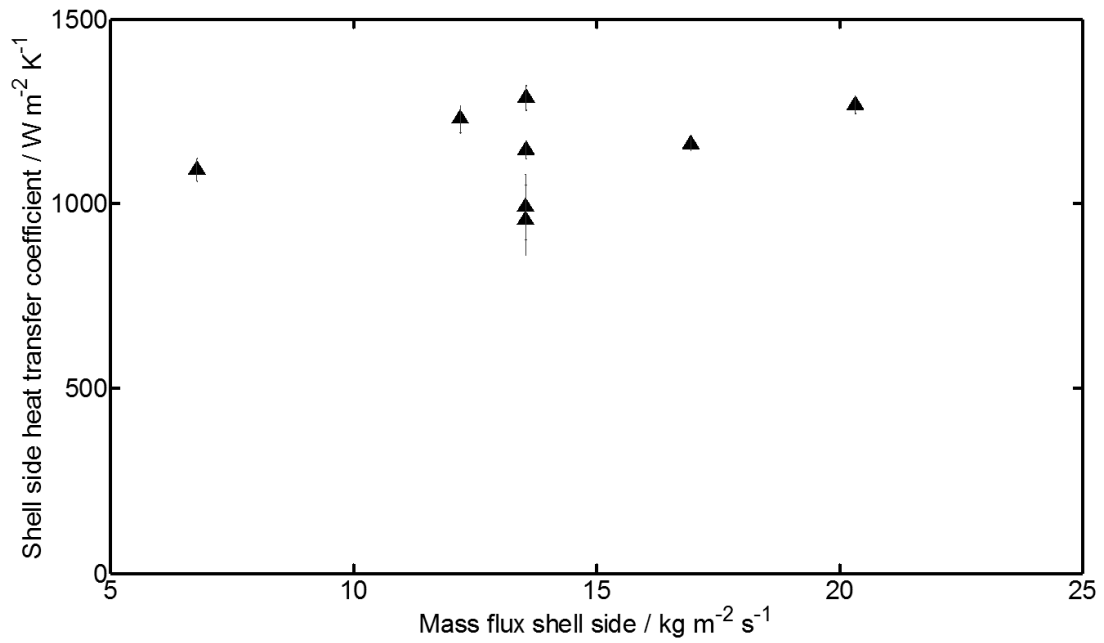
(b)

Fig. 6.9. Experimental results for the overall (a) and shell side heat transfer coefficient for single phase water in both the tube and shell sides.
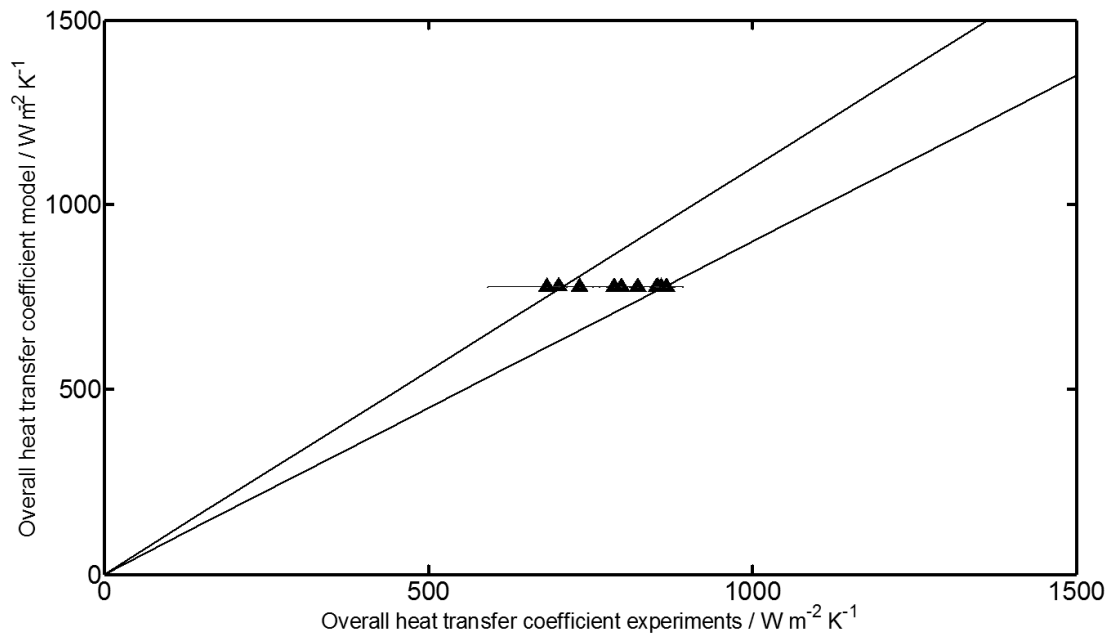
(a)
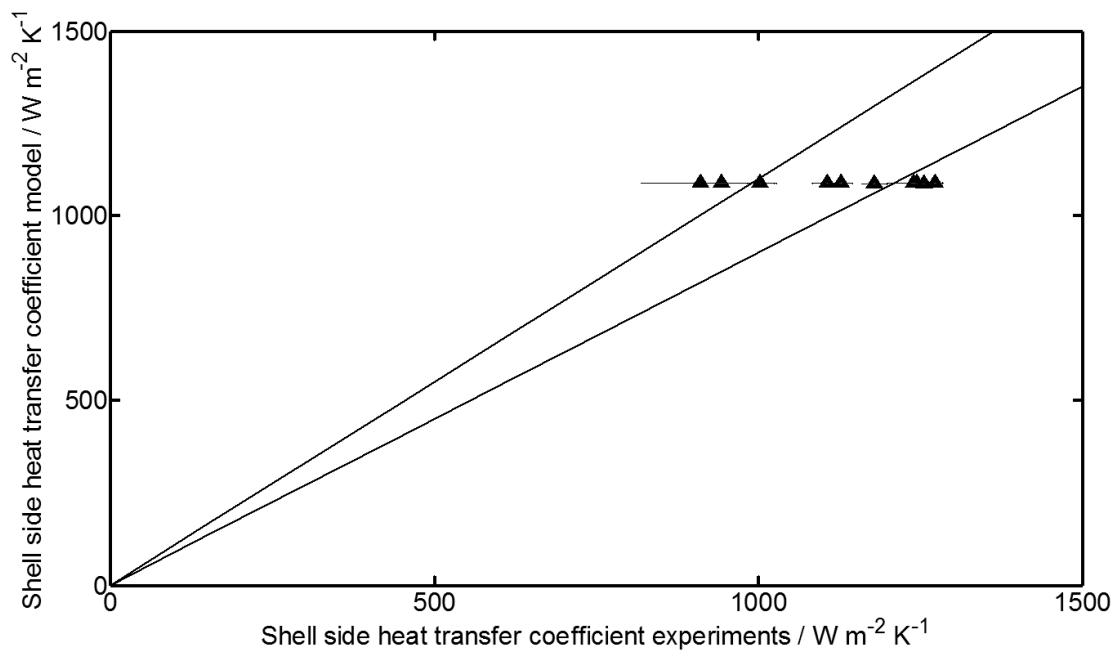
(b)

Fig. 6.10. Comparison between the numerical and experimental results for the overall (a) and shell side (b) heat transfer coefficient for single phase water in both the tube and shell sides. The lines indicate the 10% error band.
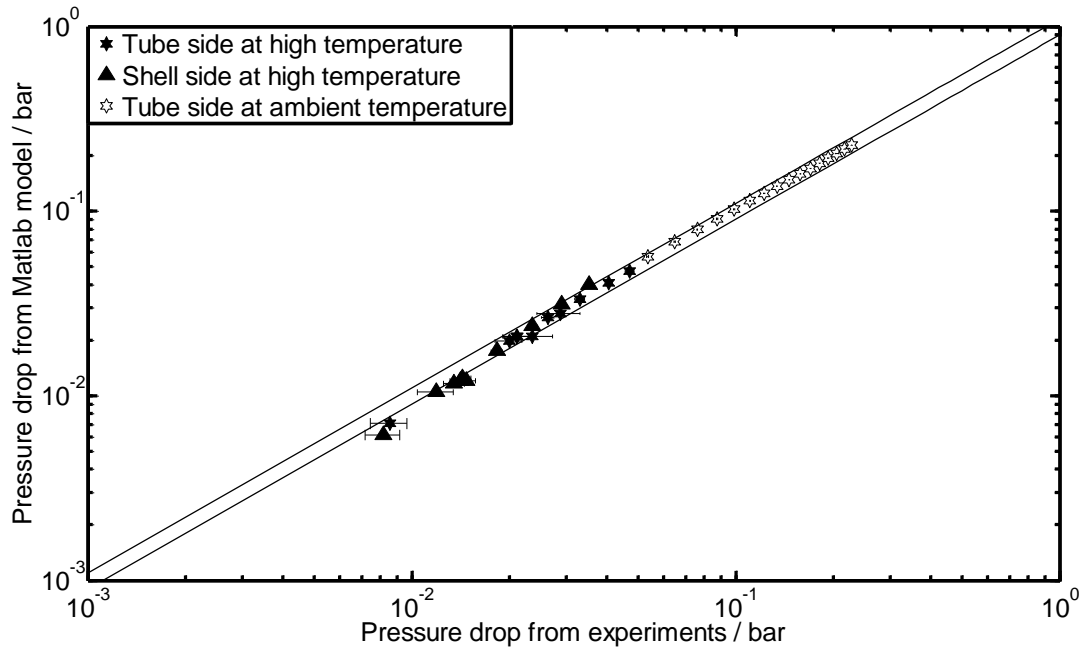
Fig. 6.11. Comparison between numerical and experimental results for the pressure drop for single phase water in both the tube and shell sides. The lines indicate the 10% error band.

Table 6.3. Numerical results of mass flux through each tube of a flow path for the largest tube side mass flux condition.

Flow path	Mass flux per tube [kg m^{-2} s^{-1}]
Outer flow path	243.79
Third flow path	243.75
Second flow path	243.71
Inner flow path	243.73

6.5   Results and discussion

Ten experiments have been conducted with a shell side inlet temperature of 160 °C and a tube side inlet temperature of 100 °C. Sixteen experiments have been conducted at ambient temperature (20 °C). The experiments at ambient temperature are only used to validate the pressure drop of the numerical model. The results for the pressure drop and overall heat transfer coefficient are respectively shown in Fig. 6.8 and Fig. 6.9. Linear relations are shown between the pressure drop and mass fluxes for both the tube and the shell sides. This is as expected, since both the flows remain laminar for all the experiments. The overall heat transfer coefficient remains constant for different mass fluxes. The Nusselt numbers are therefore approximately constant as one could expect for laminar flows.

The comparison between the mathematical model and the experimental results is shown in Fig. 6.10 for the overall and shell side heat transfer coefficient and in Fig. 6.11 for the pressure drop. The model shows agreement with the experimental results for all the data points. The lines indicate the 10% error band. The overall heat transfer coefficient is predicted within 10% deviation from the experiments, while the shell side heat transfer coefficient is predicted within approximately 15% deviation from the experiments. The deviations found during the experiments have a similar magnitude. The model can thus accurately predict the performance for laminar single phase flows. The reason why the overall heat transfer coefficients that are calculated by the numerical model are on a straight line is because the Nusselt numbers are constant in the numerical model. Due to the uncertainty in the experimental data the overall heat transfer coefficients obtained from the experiments are not located exactly on a single point. Table 6.3 shows, for the largest tube side mass flux condition, the numerical results for the mass flux through each tube. The distributor creates an excellent distribution of the fluid among all the tubes, since the difference in mass flux through each tube is less than 0.1%. Therefore the distributor performs well for a single phase laminar flow.

6.6   Conclusions

The newly proposed fractal distributor is able to evenly distribute the flow, since the relative mass flow through each tube for laminar single phase flows is approximately the same. The differences between the mass fluxes in each tube are less than 0.1% from average. The mathematical model agrees well with the experimental results for both the pressure drop and heat transfer performance, since all the data are predicted within 10% accuracy.

7 EXPERIMENTAL VALIDATION OF A MINI-CHANNEL MULTI-TUBE AMMONIA/WATER ABSORPTION/DESORPTION MODEL

In this chapter the pressure drop characteristics and heat transfer performance of a prototype multi-tube mini-channel heat exchanger are investigated. Experimental data for two-phase ammonia/water mixture flows are reported. During the experiments absorption takes place in the shell side and desorption takes place in the tube side. It is attempted to create a mathematical model which can predict the performance of the multi-tube mini-channel exchanger. Both empirical correlations and analytical derivations of conservation equations are used to identify which gives the best agreement with the experimental data.

This chapter is for a large part based on:

7.1 Introduction

In chapter 4 and 5 the performance of coaxial mini channel heat exchangers have been presented. With an ammonia water mixture flowing through these heat exchangers, heat transfer coefficients up to 10000 W m^{-2} K^{-1} can be attained. The total heat transfer under small temperature driving forces was limited to 200 W. Process industry has heating demands on the megawatt scale. To reach the megawatt scale the heat exchangers should be scaled up. Chapter 6 treated a mini channel shell and tube heat exchanger with 116 tubes that was tested for flow distribution and heat transfer performance under single phase conditions. This chapter discusses the performance of this heat exchanger when the working fluid is replaced by an ammonia-water mixture.

Since mini-channels are a relatively new technology, not many papers have been published on this topic, especially for multi-tube mini-channel heat exchangers. Li and Wu [62] correlated two-phase adiabatic pressure drop for flows in mini-channels. They first derived a general correlation to identify mini-channel flows from macro-channel flows. It was found that the dimensionless Bond and Reynolds numbers can be used to separate macro-channel driven flows from mini-channel driven flows. These two dimensionless numbers were then incorporated into the Chisholm parameter for the two-phase pressure drop multiplier. Kuczyński et al. [59] investigated the effect of hydrodynamic instabilities on the condensation heat transfer performance in mini-channels. It was found that hydrodynamic instabilities have a profound effect on the heat transfer coefficient during condensation. Garimella et al. [28] investigated the performance of a falling film absorber/desorber multi-tube mini-channel exchanger using ammonia/water as the working medium. It was found that the absorption side of the exchanger was the limiting side for heat transfer. Poor absorption side heat transfer was caused by poor distribution of the fluid. Improving the inlet distribution of the absorption flow significantly improved the heat transfer performance of the multi-tube mini-channel exchanger.

In the present chapter, the prototype multi-tube mini-channel exchanger with the geometry of a shell and tube heat exchanger without baffles as described in chapter 6 is used. In particular, the pressure drop and overall heat transfer characteristics of the shell side flow are investigated. Experiments have been conducted for absorption of an ammonia/water mixture with a composition of 33.7 wt. % ammonia in the shell side. In the tube side, experiments have been conducted for the heating of a single phase water flow and for desorption of an ammonia/water mixture with a composition of 34.0 wt. % ammonia.

The goal of this research is to measure the heat transfer en pressure drop characteristics of a prototype multi-tube mini-channel and compare these to a mathematical model.

7.2 Mathematical model

The total pressure drop of the multi-tube mini-channel exchanger is dependent on the pressure drop in the distributors and the pressure drop in the tube bundle section. In the distributors the pressure drop is caused by frictional effects and due to the redirection of the fluid. Momentum is lost since the fluid has to go through bends, contractions and expansions. The relative importance between the frictional losses and losses due to the redirections of the fluid, as well as the calculation of single phase flow pressure drop is discussed in chapter 6. For the two-phase flows, an annular flow pattern is assumed and the

Navier-Stokes momentum equations are solved for a single tube control volume. The assumptions that are made in the derivation are:

- Steady state
- Fully developed flow
- Axisymmetric flow
- Tangential and radial velocities are negligible.
- Vertical placement of exchanger.
- Laminar flow: inertial terms are negligible.
- Annular flow pattern
- Perfect distribution of liquid and vapor between the tubes.

For the heat transfer model, no heat transfer is assumed in the distributors. Heat losses to the environment are assumed to be negligible. For the single phase flows, the heat transfer coefficient of both the tube and shell side are constant and a constant heat flux condition is assumed. For the two-phase flows, the Navier-Stokes momentum equations are combined with the energy conservation equation. It is assumed that there is no axial conduction and no viscous dissipation. The result for the film velocity and vapor velocity profile is given by, respectively,

$$
u_{z,L} = \left[\frac{r^2 - R_i^2}{4\mu_L} - \frac{R_o^2}{2\mu_L} ln\left(\frac{r}{R_i}\right) \right] \frac{\partial P_V}{\partial z}
$$

$$
- \left[\frac{r^2 - R_i^2}{4\mu_L} - \frac{R_{film}^2}{2\mu_L} ln\left(\frac{r}{R_i}\right) \right] \left(\frac{\sigma}{R_{film}^2} \frac{\partial R_{film}}{\partial z} + \rho_L g_z \right) \quad \text{(7.1)}
$$

$$
- \left[\frac{R_{film}^2 - R_o^2}{2\mu_L} ln\left(\frac{r}{R_i}\right) \right] \rho_V g_z
$$

$$
u_{z,V} = \left[\frac{r^2 - R_{film}^2}{4\mu_V} + \frac{R_{film}^2 - R_i^2}{4\mu_L} - \frac{R_o^2}{2\mu_V} ln\left(\frac{R_{film}}{r}\right) - \frac{R_o^2}{2\mu_L} ln\left(\frac{R_{film}}{r}\right) \right] \frac{\partial P_V}{\partial z}
$$

$$
+ \left[\frac{R_{film}^2 - R_i^2}{4\mu_L} - \frac{R_{film}^2}{2\mu_L} ln\left(\frac{R_{film}}{R_i}\right) \right] \left(\frac{\sigma}{R_{film}^2} \frac{\partial R_{film}}{\partial z} + \rho_L g_z \right) \quad \text{(7.2)}
$$

$$
- \left[\frac{r^2 - R_{film}^2}{4\mu_V} + \frac{R_o^2}{2\mu_V} ln\left(\frac{R_{film}}{r}\right) + \frac{R_{film}^2 - R_o^2}{2\mu_L} ln\left(\frac{R_{film}}{R_i}\right) \right] \rho_V g_z
$$

R_film is the film radius, R_i is the tube radius and R_o is the tube half-pitch radius taken as the outside contour of the control volume. See Fig. 7.1 for a visual interpretation. A full derivation is given in [79]
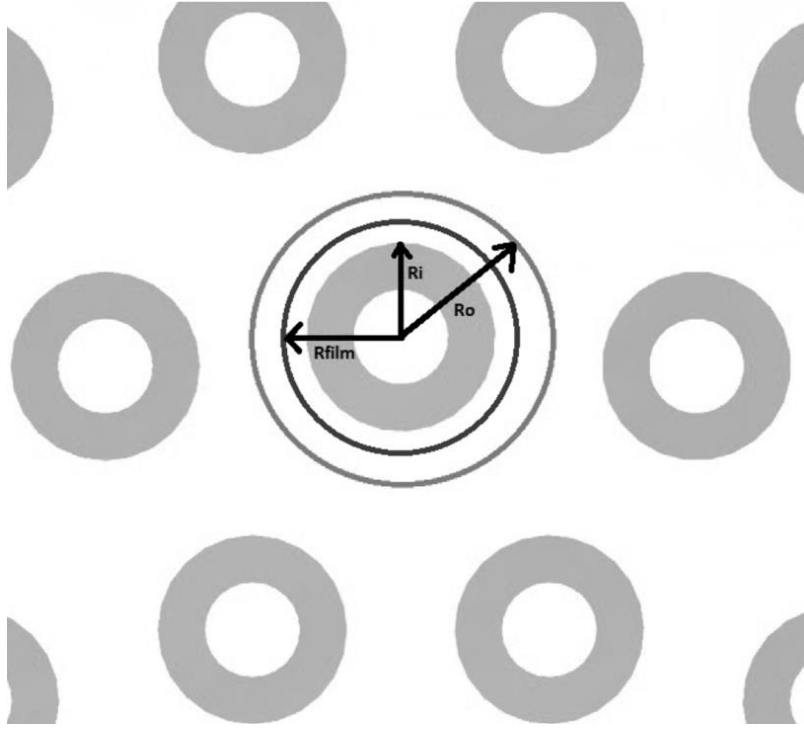
Fig. 7.1. Geometry of control volume for the shell side flow. R_{film} is the film radius, R_i is the outside radius of the tubes and R_o is the tube half pitch radius taken as the outside radius of the control volume.

There are three unknowns in the equations of the velocity profiles. These are the frictional pressure drop, the film thickness and the film thickness gradient in axial direction. The mass conservation law provides two new independent equations so the number of unknowns can be reduced to one. The conservation of mass prescribes,

$$\dot{m}_{L,inlet} = \rho_L \int_0^{2\pi} \int_{R_i}^{R_{film}} u_{z,L} r \, dr \, d\theta \tag{7.3}$$

$$\dot{m}_{V,inlet} = \rho_v \int_0^{2\pi} \int_{R_{film}}^{R_o} u_{z,V} r \, dr \, d\theta \tag{7.4}$$

The last unknown, the change in film thickness in axial direction can be calculated by iteration between two control volumes. The result of the temperature field for the shell side film is

$$T_L(r) = \frac{\rho_L C_{p,L}}{\lambda_L} \frac{\partial T}{\partial z} \left(\begin{array}{c} \left[\dfrac{r^4 - 4r^2 R_i^2}{64\mu_L} - \dfrac{R_o^2 r^2}{8\mu_L} \left(\ln\left(\dfrac{r}{R_i}\right) - 1 \right) \right] \dfrac{\partial P_V}{\partial z} \\[2ex] - \left[\dfrac{r^4 - 4r^2 R_i^2}{64\mu_L} - \dfrac{R_{film}^2 r^2}{8\mu_L} \left(\ln\left(\dfrac{r}{R_i}\right) - 1 \right) \right] \left(\dfrac{\sigma}{R_{film}^2} \dfrac{dR_{film}}{dz} + \rho_L g_z \right) \\[2ex] - \left[\dfrac{R_{film}^2 - R_o^2}{8\mu_L} r^2 \left(\ln\left(\dfrac{r}{R_i}\right) - 1 \right) \right] \rho_V g_z + c_5 \ln(r) + c_6 \end{array} \right) \tag{7.5}$$

For the shell side vapor the temperature profile is given by

$$T_V(r) = \frac{\rho_V C_{p,V}}{\lambda_V} \frac{\partial T}{\partial z}$$

$$
\left(
\begin{array}{c}
\left[\frac{r^4 - 4r^2 R_{film}^2}{64\mu_V} + r^2 \frac{R_{film}^2 - R_i^2}{16\mu_L} - \left(\frac{R_o^2}{8\mu_V} + \frac{R_o^2}{8\mu_L}\right) r^2 \left(\ln\left(\frac{R_{film}}{r}\right) + 1\right)\right] \left(\frac{\partial P_V}{\partial z}\right) \\
+ r^2 \left[\frac{R_{film}^2 - R_i^2}{16\mu_L} - \frac{R_{film}^2}{8\mu_L} \ln\left(\frac{R_{film}}{R_i}\right)\right] \left(\frac{\sigma}{R_{film}^2} \frac{dR_{film}}{dz} + \rho_L g_z\right) \\
- \left[\frac{r^4 - 4r^2 R_{film}^2}{64\mu_V} + \frac{R_o^2}{8\mu_V} r^2 \left(\ln\left(\frac{R_{film}}{r}\right) + 1\right) + r^2 \frac{R_{film}^2 - R_o^2}{8\mu_L} \ln\left(\frac{R_{film}}{R_i}\right)\right] \rho_V g_z \\
+ c_7 \ln(r) + c_8
\end{array}
\right)
$$

(7.6)

The values of constants c_5, c_6, c_7 and c_8 depend on the boundary conditions and are given in Table 7.1. The wall temperature is determined using the outlet temperature of the previous control volume.

Three different heat transfer coefficients can be identified: between wall and film, between film and interface and between interface and vapor core.

$$hc_{wall,film} = \frac{\lambda_L}{\bar{T}_L - T_w} \frac{\partial T_{film}}{\partial r}(R_i)$$

(7.7)

$$hc_{film,interface} = \frac{\lambda_L}{T_{int} - \bar{T}_L} \frac{\partial T_{film}}{\partial r}(R_{film})$$

(7.8)

$$hc_{interface,vap} = \frac{\lambda_V}{\bar{T}_V - T_{int}} \frac{\partial T_V}{\partial r}(R_{film})$$

(7.9)

The average temperature for the liquid film and vapor core are defined as

$$\bar{T}_L = \frac{\int_{R_i}^{R_{film}} u_{z,L}(r) T_L(r) r\, dr}{\int_{R_i}^{R_{film}} u_{z,L} r\, dr}$$

(7.10)

$$\bar{T}_V = \frac{\int_{R_i}^{R_{film}} u_{z,V}(r) T_V(r) r\, dr}{\int_{R_i}^{R_{film}} u_{z,V}(r) r\, dr}$$

(7.11)

The heat transfer coefficients for the empirical model are determined using a more straightforward method. The film thickness is calculated according to the equations proposed by Ausillious and Quèrè [5], were the hydraulic diameter of the shell has been substituted for the diameter of the tubes.

$$R_{film} = R_i + \frac{0.67 d_{H,shell} Ca^{2/3}}{1 + 3.35 Ca^{2/3}}$$

(7.12)

101

Table 7.1 Integration constants for the film and vapor temperature profile.

Constant	equation

c_5

$$\frac{\lambda_L(T_w - T_{int})}{\rho_L C_{p,L} \frac{\partial T}{\partial z} \ln\left(\frac{R_i}{R_{film}}\right)} - \frac{\left[\frac{R_o^2 R_i^2}{8\mu_L} - \frac{R_{film}^4 - 4R_{film}^2 R_i^2 + 3R_i^4}{64\mu_L} + \frac{R_o^2 R_{film}^2}{8\mu_L}\left(\ln\left(\frac{R_{film}}{R_i}\right) - 1\right)\right]\frac{\partial P_V}{\partial z}}{\ln\left(\frac{R_i}{R_{film}}\right)}$$

$$+ \frac{\left[\frac{R_{film}^4 - 4R_{film}^2 R_i^2 + 3R_i^4}{64\mu_L} - \frac{R_{film}^2 R_i^2}{8\mu_L} - \frac{R_{film}^4}{8\mu_L}\left(\ln\left(\frac{R_{film}}{R_i}\right) - 1\right)\right]\left(\frac{\sigma}{R_{film}^2}\frac{dR_{film}}{dz} + \rho_L g_z\right)}{\ln\left(\frac{R_i}{R_{film}}\right)}$$

$$+ \frac{\left[\frac{R_{film}^2 - R_o^2}{8\mu_L}R_i^2 + \frac{R_{film}^2 - R_o^2}{8\mu_L}R_{film}^2\left(\ln\left(\frac{R_{film}}{R_i}\right) - 1\right)\right]\rho_V g_z}{\ln\left(\frac{R_i}{R_{film}}\right)}$$

c_6

$$\frac{\lambda_L T_{int}}{\rho_L C_{p,L}\frac{\partial T}{\partial z}} - \left(\begin{array}{c} \left[\frac{R_{film}^4 - 4R_{film}^2 R_i^2}{64\mu_{film}} - \frac{R_o^2 R_{film}^2}{8\mu_{film}}\left(\ln\left(\frac{R_{film}}{R_i}\right) - 1\right)\right]\frac{\partial P_V}{\partial z} \\ -\left[\frac{R_{film}^4 - 4R_{film}^2 R_i^2}{64\mu_L} - \frac{R_{film}^4}{8\mu_L}\left(\ln\left(\frac{R_{film}}{R_i}\right) - 1\right)\right]\left(\frac{\sigma}{R_{film}^2}\frac{dR_{film}}{dz} + \rho_L g_z\right) \\ -\left[\frac{R_{film}^2 - R_o^2}{8\mu_L}R_{film}^2\left(\ln\left(\frac{R_{film}}{R_i}\right) - 1\right)\right]\rho_V g_z + c_5 \ln(R_{film}) \end{array}\right)$$

c_7

$$-\frac{\rho_V C_{p,V}}{\lambda_V}\frac{\partial T}{\partial z}$$

$$\left(\begin{array}{c} \left[\frac{R_o^4 - 2R_o^2 R_{film}^2}{16\mu_V} + R_o^2\frac{R_{film}^2 - R_i^2}{8\mu_L} - \left(\frac{R_o^4}{8\mu_V} + \frac{R_o^4}{8\mu_L}\right)\left(\ln\left(\frac{R_{film}}{R_o}\right) + \frac{1}{2}\right)\right]\left(\frac{\partial P_V}{\partial z}\right) \\ + R_o^2\left[\frac{R_{film}^2 - R_i^2}{8\mu_L} - \frac{R_{film}^2}{4\mu_L}\ln\left(\frac{R_{film}}{R_i}\right)\right]\left(\frac{\sigma}{R_{film}^2}\frac{dR_{film}}{dz} + \rho_L g_z\right) \\ -\left[\frac{R_o^4 - 2R_o^2 R_{film}^2}{16\mu_V} + \frac{R_o^4}{4\mu_V}\left(\ln\left(\frac{R_{film}}{R_o}\right) + \frac{1}{2}\right) + \frac{R_o^2 R_{film}^2 - R_o^4}{4\mu_L}\ln\left(\frac{R_{film}}{R_i}\right)\right]\rho_V g_z \end{array}\right)$$

c_8

$$\frac{\lambda_V T_{int}}{\rho_V C_{p,V}\frac{\partial T}{\partial z}} -$$

$$-\left\{\begin{array}{c} \left[\frac{-3R_{film}^4}{64\mu_V} + \frac{R_{film}^4 - R_{film}^2 R_i^2}{16\mu_L} - \left(\frac{R_o^2}{8\mu_V} + \frac{R_o^2}{8\mu_L}\right)R_{film}^2\right]\left(\frac{\partial P_V}{\partial z}\right) \\ + R_{film}^2\left[\frac{R_{film}^2 - R_i^2}{16\mu_L} - \frac{R_{film}^2}{8\mu_L}\ln\left(\frac{R_{film}}{R_i}\right)\right]\left(\frac{\sigma}{R_{film}^2}\frac{dR_{film}}{dz} + \rho_L g_z\right) \\ -\left[\frac{-3R_{film}^4}{64\mu_V} + \frac{R_o^2 R_{film}^2}{8\mu_V} + \frac{R_{film}^4 - R_{film}^2 R_o^2}{8\mu_L}\ln\left(\frac{R_{film}}{R_i}\right)\right]\rho_V g_z + c_7 \ln(R_{film}) \end{array}\right\}$$

The velocity in the film is relatively low, so a Nusselt number of 1 is assumed here, indicating that the heat transfer is governed by conduction through the film only. The vapour core is modelled as an annulus. For an annulus, VDI [105]gives

$$Nu_V = 3.66 + 1.2 \left(\frac{R_{film}}{R_o}\right)^{-0.8} \tag{7.13}$$

$$hc_{film,int} = \frac{\lambda_L}{R_{film} - R_i} \tag{7.14}$$

$$hc_{V,int} = Nu_V \frac{\lambda_V}{d_{H,shell}} \tag{7.15}$$

The interface temperature of the liquid film and the annular vapour core flow during absorption and desorption is determined by the molar balances as proposed by Sieres and Fernández-Seara [91]. The interface temperature can be obtained using the energy conservation at the interface and assuming that the interface is at equilibrium conditions. This prescribes that

$$\dot{Q}_{film,conv} + \dot{m}_{int} h_L = \dot{Q}_{V,conv} + \dot{m}_{int} h_V \tag{7.16}$$

The molar fluxes into the liquid and out of the vapour should be equal in binary mixtures. The molar fluxes are related to the driving force of mass transfer with [91]

$$\bar{J}_{V,NH_3} = F_V ln\left(\frac{z^* - X_{bulk,V}}{z^* - X_{int,V}}\right) = F_L ln\left(\frac{z^* - X_{int,L}}{z^* - X_{bulk,L}}\right) \tag{7.17}$$

The mass transfer coefficients are related to the heat transfer coefficients using the Chilton-Colburn analogy:

$$F_V = \frac{hc_{V,int}}{C_{p,V}\left(X_{bulk,V} MW_{NH_3} + \left(1 - X_{bulk,V}\right)MW_{H_2O}\right)} Pr_V^{2/3} Sc_V^{-2/3} \tag{7.18}$$

$$F_L = \frac{hc_{film,int}}{C_{p,L}\left(X_{bulk,L} MW_{NH_3} + \left(1 - X_{bulk,L}\right)MW_{H_2O}\right)} Pr_L^{2/3} Sc_L^{-2/3} \tag{7.19}$$

Both the tube and shell sides are divided into 5000 control volumes. The model starts with a linear temperature profile for the tube side. Then the 5000 control volumes of the shell side are evaluated, starting with the shell inlet side of the exchanger. When the entire shell side is calculated, the tube side is then calculated, starting with the tube inlet of the exchanger. This gives a new temperature profile of

the tube side. Using this new temperature profile, the shell side is once again evaluated. This iteration is continued until the mean relative error of the heat flux between the tube side control volumes and shell side control volumes is less than 1%. The programming environment used to solve the equations is Matlab R2012a [100].

7.3 Experimental setup and data reduction

The experimental setup described in chapter 6 and shown in Fig. 6.7 is used for the experiments. The multi-tube mini-channel exchanger is placed vertically and the shell side flow enters from the top and the tube side flows enters from the bottom, creating a counter-current flow. The experimental conditions have been selected to reproduce the operating conditions of a compression-resorption heat pump integrated with a distillation process. The operating temperatures range from 100 °C to 160 °C. For experiments conducted with the ammonia/water mixture the inlet temperatures remained within ± 2 K from their average value.

The pressure drop of the exchanger can directly be obtained from the experimental data using the differential pressure sensor. The overall heat transfer coefficient is defined by:

$$U_O = \frac{\dot{Q}}{A_O \Delta T}$$

(7.20)

Where the contact area is defined by:

$$A_O = \pi d_o N L$$

(7.21)

The total heat that is transferred between the inlet of the exchanger and the outlet is retrieved from:

$$\dot{Q} = \dot{m}_{shell}\left(h_{shell,i} - h_{shell,o}\right)$$

(7.22)

The enthalpy's are obtained from RefProp 9 thermodynamic database, Lemmon et al. [61], and are based on the current pressure, temperature and composition.

$$h_{shell,inlet} = f(P_{shell,i}, T_{shell,i}, x_{shell})$$

(7.23)

$$h_{shell,outlet} = f(P_{shell,o}, T_{shell,o}, x_{shell})$$

(7.24)
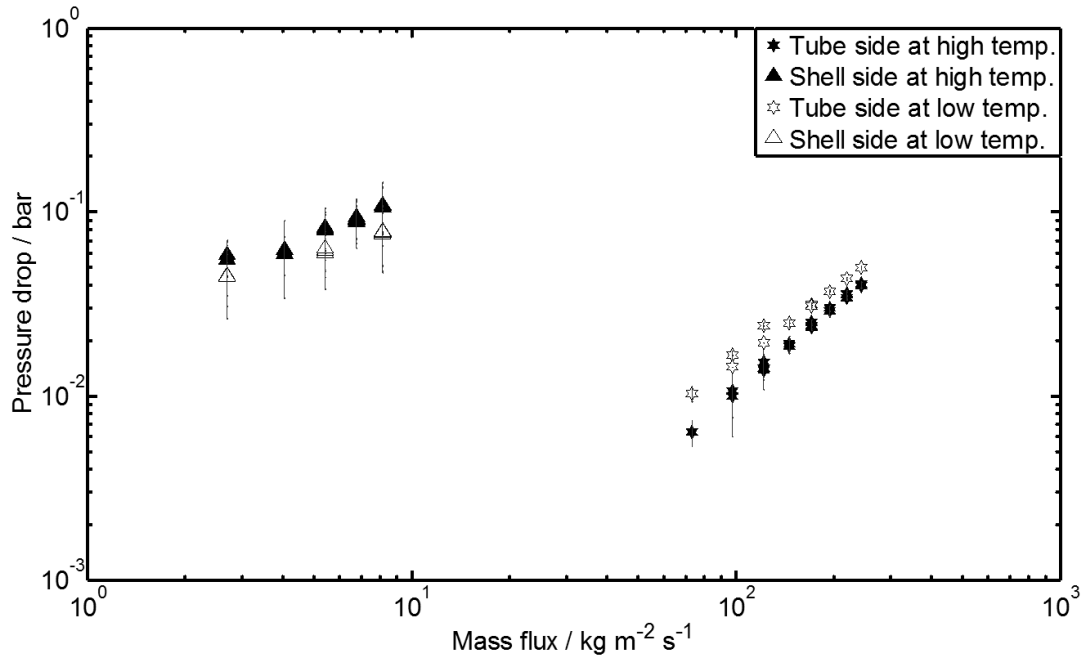
Fig. 7.2. Experimental pressure drop results for single phase water flow in tube side and absorption of ammonia/water in the shell side.

To improve the estimation of the mean temperature driving force in the exchanger, the exchanger is divided into 5000 control volumes. For each control volume, the local driving force is calculated and a constant heat flux is assumed within the control volume. The temperatures in each control volume are calculated by applying the conservation of energy. Equilibrium conditions have been assumed at both the inlet and outlet of the heat exchanger. The mean driving force and overall heat transfer coefficient of the exchanger is then obtained by:

$$\Delta T = \Delta \bar{T}_{local}$$

(7.25)

$$U = \bar{U}_{local}$$

(7.26)

7.4   Results and discussion

The results for single phase heat transfer have extensively been discussed in chapter 6. The results showed a constant heat transfer coefficient regardless of mass flux and increasing pressure drop with increasing mass flux. The model developed for the single phase flow was capable of predicting all experimental results within 10%. In this chapter the focus lies on the heat transfer in the shell side of a prototype heat exchanger where a two-phase ammonia-water mixture flows through the shell and water flows through the tubes. The heat transfer characteristics of the same prototype mini channel heat exchanger are treated when a two-phase ammonia-water mixture flows through both the tube and the shell side.
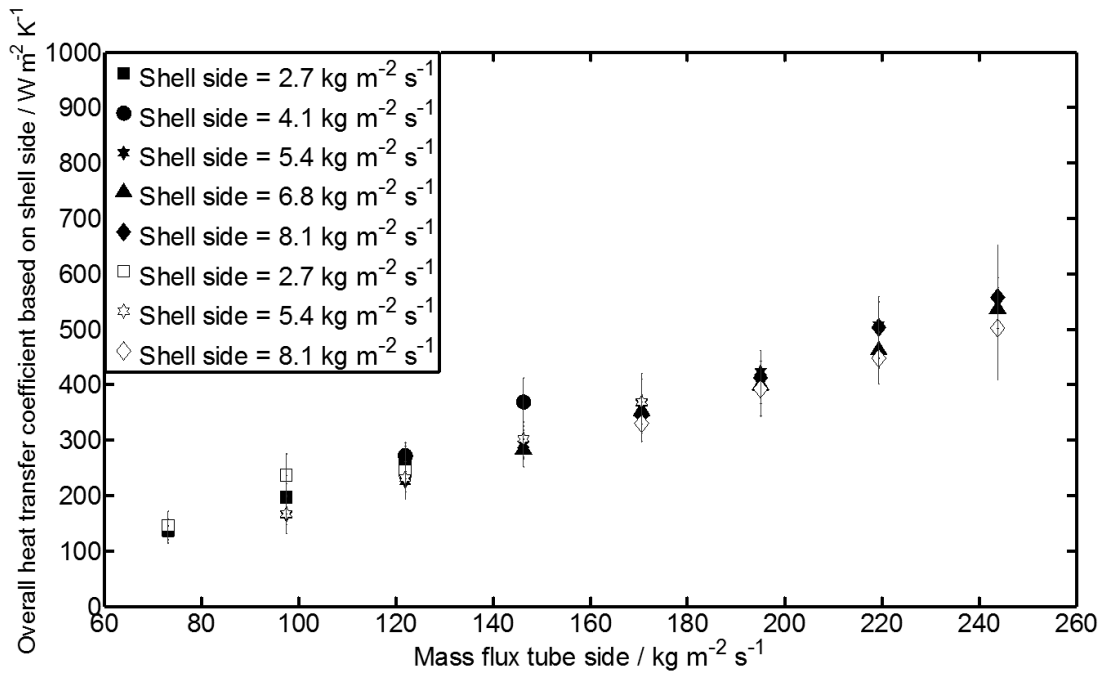
Fig. 7.3. Experimental results for the overall heat transfer coefficient for single phase water flow in the tube side and absorption of ammonia/water in the shell side. The closed symbols are the results for high operating temperature and the open symbols are the results for low operating temperature.

Fig. 7.4. Comparison between the shell side pressure drop obtained with the mathematical models and the experimental results. The lines indicate the 10 % error band.

Fig. 7.5. Comparison between the overall heat transfer coefficient obtained from the mathematical model based on the empirical correlations/analytical solution and the experimental results. The lines indicate the 10 % error band.

7.4.1 Single phase water flow in the tube side and absorption of ammonia/water in the shell side

Twenty experiments have been conducted with a shell side inlet temperature of 160 °C and a tube side inlet temperature of 100 °C to match the industrial conditions of the processes of the companies involved. Eleven experiments have been conducted with a shell side inlet temperature of 140 °C and a tube side inlet temperature of 100 °C to investigate the influence of vapour quality. The results for the pressure drop and overall heat transfer coefficient are respectively shown in Fig. 7.2 and Fig. 7.3. The comparison between the mathematical model and the experimental results are shown in Fig. 7.4 for the pressure drop and in Fig. 7.5 for the overall heat transfer coefficient. The uncertainty is determined by the methods suggested by Taylor and is a function of both sensor inaccuracy and variation in measurement data. The accuracy of the sensors used is given in Table 4.1.

The pressure drop for the two-phase ammonia/water mixture is higher than for a single phase water flow. An interesting result is the large increase in uncertainty for the measurement data. The experimental overall heat transfer coefficient has dropped significantly when compared to the single phase flow previously discussed in chapter 6. The heat transfer coefficient of the ammonia/water absorption in the shell side is therefore much lower than in the case of a single phase water flow. The heat transfer is now limited by the shell side flow. This is also shown by the strong influence of the tube side mass flux on the overall heat transfer coefficient, see Fig. 7.3. Increasing the tube side mass flux will lower the tube wall temperature and this will increase the heat transfer coefficient of the shell side. Increasing the heat flux through the wall thus increases the shell side heat transfer coefficient. Since the shell side is the limiting side for heat transfer, the overall heat transfer coefficient increases strongly for higher tube side mass fluxes.

Fig. 7.6. Experimental pressure drop results for absorption of ammonia-water in the shell side and desorption of ammonia-water in the tube side.
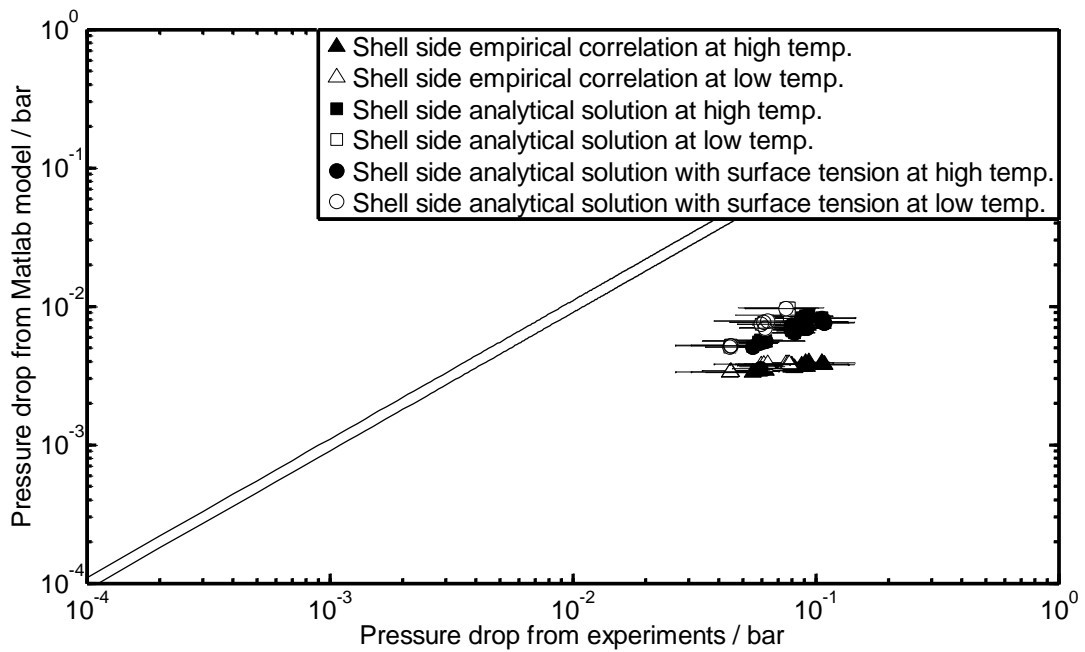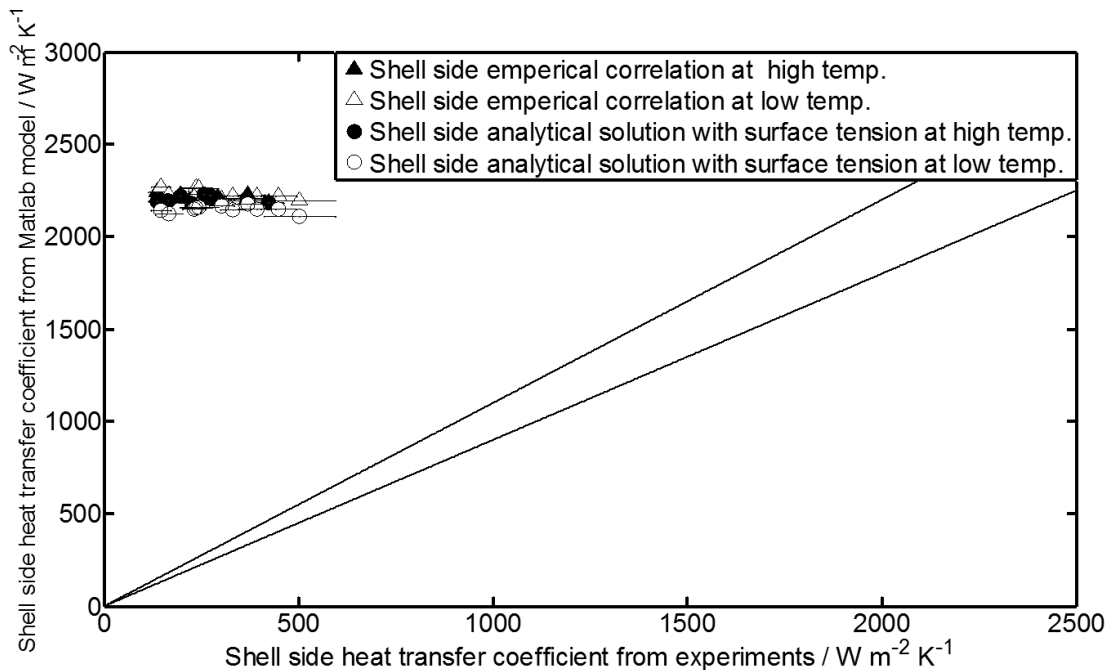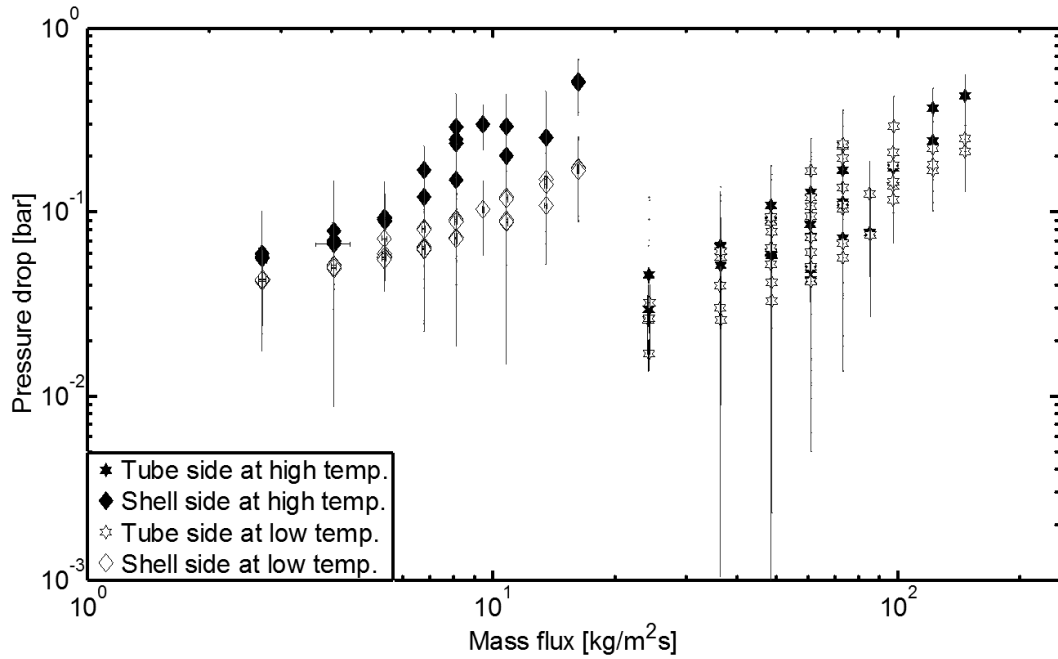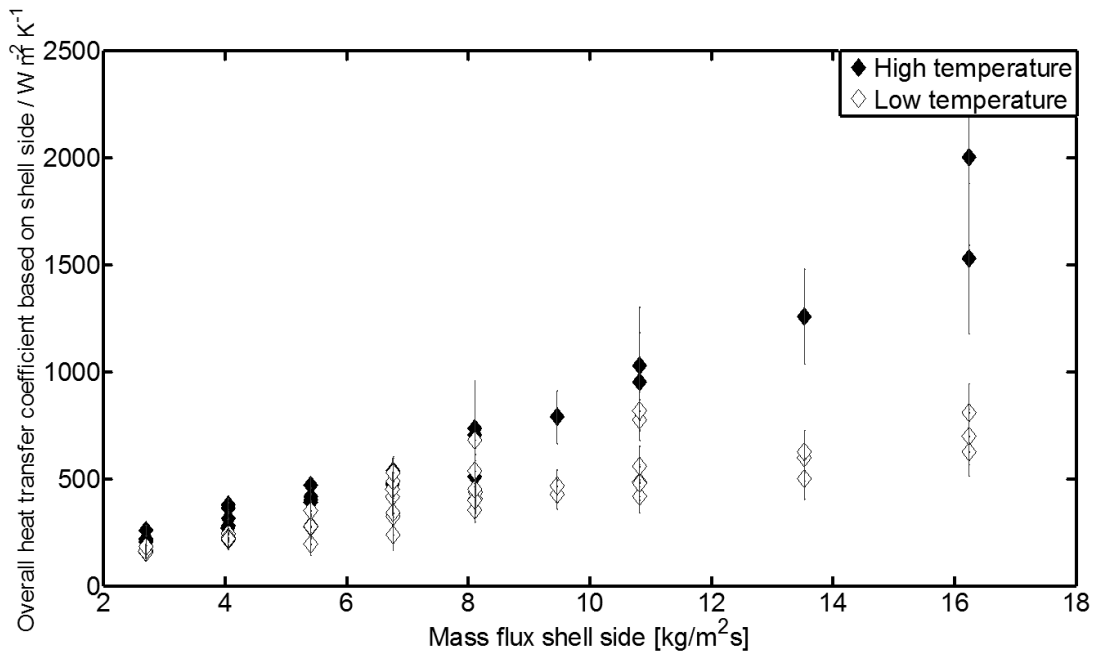

Fig. 7.7. Experimental results for the overall heat transfer coefficient for absorption of ammonia-water in the shell side and desorption of ammonia-water in the tube side.

The model cannot predict the performance of the exchanger in terms of pressure drop and heat transfer. The main reason why such a large difference exists between the model and reality is explained by hydrodynamic instabilities. Such instability is best explained as a dynamic effect caused by a vapour being absorbed by the liquid. The volume flow and velocity reduces rapidly, causing a slightly lower pressure locally. Flow further downstream temporarily slows down or might shortly move upstream, to move downstream a moment later again, while flow upstream is temporarily accelerated. The pressure drop between in- and outlet at that moment is below average. These instabilities and their effect on the pressure drop and heat transfer performance have not been taken into account in the model, but are reported in [58].

7.4.2 Ammonia/water in both the tube and shell side

Twenty-four experiments have been conducted with a shell side inlet temperature of 160 °C and a tube side inlet temperature of 110 °C. Forty-five experiments have been conducted with a shell side inlet temperature of 140 °C and a tube side inlet temperature of 110°C. The results for the pressure drop and overall heat transfer coefficient are respectively shown in Fig. 7.6 and Fig. 7.7. Both pressure drop and heat transfer coefficient increase with increasing shell side mass flux. For experiments with the high temperature set point the heat transfer coefficient is significantly larger than for the experiments with a low temperature set point. The effect is more pronounced compared to the experiments with water in the tube side and can be attributed to a larger vapour quality in the tube side and a large heat flux. In section 7.4.1 an increasing heat flux resulted in a better heat transfer coefficient for the ammonia/water mixture. Since the model of the previous flow configuration showed such a poor agreement with the experimental results, and hydrodynamic instabilities would also in this case cause large effects, no model for this flow configuration has been built yet.

Again the large uncertainty in the measurement data must be noticed, which is now also shown in the two-phase flow in the tube side. At low shell side mass fluxes, the overall heat transfer coefficient has not changed significantly in comparison to Fig. 7.3. This means that the heat transfer coefficient of the ammonia/water desorption flow is much higher than the heat transfer coefficient for the shell side flow.

7.5 Conclusions

Comparing the results for the single phase flows with the results of the two-phase flows, it is noticed that the uncertainty in the measurement data has increased significantly for two phase flows because of larger variation in this data. It appears that for two-phase, hydrodynamic instabilities start to occur in the multi-tube mini-channel exchanger. As stated before, hydrodynamic instabilities have a profound effect on the heat transfer performance during condensation and most likely also during absorption. These instabilities tend to decrease the heat transfer coefficient and this effect is clearly shown when comparing the results of the overall heat transfer coefficients between the single phase and two phase flows. The heat transfer coefficient is much lower when the single phase water flow is changed for an ammonia/water two phase mixture flow in the shell side. In the case where the two-phase ammonia/water mixture is present in the shell side, heat transfer of the multi-tube mini-channel heat exchanger is limited by the shell side. The tube side also shows hydrodynamic instabilities for two phase flows. However for the tube side, the hydrodynamic instabilities do not have such a profound effect on the heat transfer coefficient, since the heat transfer is still limited by the shell side.

The mathematical model shows good agreement with the experimental results for the case where single phase water flows in both the tube and shell sides. For the cases with two-phase flow, hydrodynamic instabilities start to occur. These effects are not taken into account in the model and therefore lead to large disagreement between the model and the experiments. Hydrodynamic instabilities increase the pressure drop of laminar flows and decrease the heat transfer performance of especially the absorption flow. The pressure drop is thus under predicted by the model and the heat transfer coefficient is over predicted by the model.

8 CONCLUSIONS AND RECOMMENDATIONS

The main objectives of the research presented in this thesis are to investigate the performance and the investment cost of compression-resorption heat pumps and to make its application in industry more feasible by improving the heat pumps efficiency and reducing investment costs. The main components of a compression-resorption heat pump are two heat exchangers and a compressor. Both components can be considered to be fully developed and improvements can be considered of minor importance. However, modern fabrication techniques allow for unconventional designs which could potentially be cost saving and increase the performance of a heat pump. Some of the recent developments are liquid injected compressors and miniaturization of heat exchangers. The first improves the performance of the heat pump and reduces the investment cost of a compression-resorption heat pump by eliminating a separate pump from the system. The latter offers higher performance and smaller sizes, thereby possibly reducing the investment cost of the system. In this thesis the heat exchangers have been investigated.

8.1   Conclusions

The technical and economic performance of different types of heat pumps based on conventional technology has been investigated. A method has been proposed for simple estimation of industrial heat pump performance. The economic performance was estimated, while no detailed knowledge of heat pumps, working fluids, or process was required. Applying the proposed method showed that the use of a heat pump could significantly reduce the costs for energy required to operate distillation columns. A generic column, which allows 50% of the lift to be used as temperature glide for a compression-resorption heat pump, will have a minimum pay-back period of about 3 years for a 10 MW$_{th}$ system. Thermally driven heat pumps could be a good alternative for smaller systems from a pay-back period point of view as long as large temperature driving forces are chosen. On the longer term mechanically driven heat pumps are preferred because they can attain larger reductions in energy cost.

A compression-resorption heat pump reduces both the energy use and related costs for more than 90% of the industrial process applications considered. Using this technology, energy savings are possible up to temperature lifts of 124 K and cost savings up to temperature lifts of 145 K when compared to conventional natural gas fired boilers.

Designing a compression-resorption heat pump for optimal efficiency has been simplified: the optimal operating conditions of a compression-resorption heat pump can be found at a resorber inlet vapor quality of 100% at the minimum specified temperature driving force. The glide of the resorber should exactly match the glide of the reboiler at this condition, so the ammonia concentration is dependent on the temperature glide and temperature level.

The heat transfer performance of a two phase ammonia-water mixture flowing through an annular mini channel heat exchanger with a hydraulic diameter of 0.4 mm was experimentally investigated. The heat transfer coefficients of the mixture ranged from 1000 up to approximately 10000 W m^{-2} K^{-1}. The heat transfer coefficient increases with increasing mass flux and vapor quality. The heat transfer coefficient rises sharply at low vapor qualities when the mass flux is increased from 100 to 175 kg m^{-2} s^{-1} Pressure drop was predicted well by the correlations for gas-liquid flow proposed by Zhang et al. [117]. Both of the investigated models for condensation in mini-channels over predicted the experimental heat transfer coefficient. A new correlation for predicting the heat transfer performance based on heat load was provided,

$$hc_{NH_3-H_2O} = 0.0152 \left(\frac{\dot{Q}}{A_O} \right)^{1.17}$$

(8.1)

With A_O the heat transfer area in m^2 and $\dot{Q}$ the heat transfer rate in W.

A similar investigation was performed for a tubular mini channel heat exchanger operating as a desorber. The heat transfer coefficients obtained in a 1.1 mm tube ranged from 5500 up to 10500 W m^{-2} K^{-1}. The heat transfer coefficient increases with increasing mass flux. During the experiments the pressure drop increased over time, indicating ongoing blockage of the tube. Therefore the pressure drop showed no good correlation with models available in literature. Taking into account only the first set of experiments,

the gas-liquid model by Zhang et al. [117] shows good agreement with the experimental data. The heat transfer performance on the other hand could be predicted by the model for boiling suggested by Thome [101] after changing one of the empirical constants. New empirical correlations based on mass flux or heat load showed better accuracy, but probably show limited predictive behavior for dissimilar conditions.

The flow distribution in a mini-channel heat exchanger with 116 tubes of 0.5 mm diameter was investigated. A model was created to investigate the distribution of a single phase flow. According to this model, based on the inlet geometry of the heat exchanger, the flow is distributed well within 0.1%. The obtained results for heat transfer and pressure drop are within a 10% error band from predictions.

The heat transfer performance of the same heat exchanger was also investigated with an ammonia-water mixture as working fluid. From the results obtained with this mixture it becomes clear that when the shell side is filled with the ammonia-water mixture under two-phase flow conditions, the shell side is limiting the heat transfer coefficient. Comparison with an analytical and empirical model shows that the heat transfer coefficient should be larger while the pressure drop should be lower. The combination of these effects is possibly caused by hydrodynamic instabilities which were measured during the experiments.

Putting an ammonia-water mixture operating under two-phase flow conditions in the tube side of the heat exchanger allowed for higher flow rates in the shell side as well. By doubling the flow rate through the shell the obtained overall heat transfer coefficient was increased from 600 W m^{-2} K^{-1} to around 1600 W m^{-2} K^{-1}. The heat exchanger performance is therefore very sensitive to the shell side mass flux. This could be the result of the, compared to the diameter of the tubes, relatively large hydraulic diameter of the shell. Measurements on the tube side of the heat exchanger with the water-ammonia mixture operating under two-phase flow conditions also showed instabilities. These instabilities did not show a clear reduction in heat transfer performance.

8.2   Recommendations

Comparing the heat transfer coefficients obtained during the experiment with the 116 tubes mini channel heat exchanger and the single 1.1 mm tube, the performance of the former is unexpectedly low. The heat transfer coefficient can be improved by increasing the shell side mass flux. It does not solve the main causes for the poor heat transfer coefficient, namely hydrodynamic instabilities, possible problems with flow distribution and a relatively large hydraulic diameter of the shell. These problems should be addressed in a new design of the heat exchanger. The performance should also be compared against a single tube with a diameter of 0.5 mm to assure the lower performance is not caused by the reduction in tube diameter.

Since the production costs of the heat exchanger were relatively high due to the complex components that had to be manufactured, more modern production techniques should be investigated. Examples of modern techniques that could be employed are etching, electrical discharge machining and metal layer 3D printing. Possibly these techniques can also be used to overcome the problems with flow instabilities, distribution and the hydraulic diameter of the shell since such technologies allow for more complex

shapes to be manufactured. Especially for the desorber there is no problem to have additional pressure drop at the inlet since it will be placed directly after an expansion valve, with the sole purpose of reducing the pressure to the desired pressure at the desorber inlet.

Reducing flow oscillations and improving the distribution to the absorber might be improved by distributing the flow as a gas; when using wet compression the optimum operating point is found when the fluid is a saturated vapor at the resorber inlet. Otherwise using a conventional compressor the inlet of the resorber is at superheated vapor conditions. Using the Osenbruck cycle where a pump is placed parallel to the compressor to pump the liquid could require a different header design where vapor is injected into the liquid stream.

Furthermore the overall performance of a heat pump could possibly be further improved by application of a wet compressor. However, the research should maybe not be focused on designing a compressor operating under wet conditions at both inlet and outlets, but only with wet conditions at the inlet, based on the results in the third chapter. Some conventional compressors, for instance screw and scroll compressors, already allow some liquid carry-over. Piston compressors are known to have problems with liquid slugging, thereby damaging the valves. Reducing the rotational speed reduces this problem, and operating such a compressor in the wet inlet / saturated outlet regime could also aid in significantly reducing or eliminating this problem. Research should therefore focus on controlling the systems such that the outlet of the compressors remains fixed at saturated conditions.

SUMMARY

In this thesis the technical and economic performance of compression-resorption heat pumps has been investigated. The main objective of this thesis was to improve the performance and reduce the investment costs of compression-resorption heat pumps applied in process industry. A model that is able to capture the performance of most heat pumps based on the Carnot and Lorentz COP by only knowing the temperature driving forces and estimating the compressor isentropic efficiency has been developed. By including an economic model for the investment costs of compressors and heat exchangers and including costs for electricity and heating, the model was capable of predicting the payback period for conventional systems. For larger systems of 10 MW$_{th}$ applied to a standard distillation column where compression-resorption heat pumps could use 50% of the lift as temperature glide, predictions show that such a heat pump will have a minimum payback period of approximately 3 years, while systems with a capacity of 2.8 MW$_{th}$ require about 5 years, clearly demonstrating the effect of system size.

A more detailed model was implemented to investigate the performance of a compression-resorption heat pump applied to distillation processes in the Dutch industry. In this case, the heat pump could only make use of the temperature glide available in reboilers and condensers, which is much smaller than using the temperature glide in the columns. This is limiting the possible performance of the heat pump. The results showed that for most cases the performance was such that both energetic and cost advantages can be obtained with the implementation of such heat pumps. Further the model showed that in case of wet compression the inlet of the absorber should be a saturated vapor to reach maximum efficiency.

To increase the performance of the compression-resorption heat pump and decrease the investment cost, the performance of mini-channel heat exchangers operating with a two-phase ammonia-water mixture was experimentally investigated. Initial research focused on the absorber performance in a mini channel annulus with a hydraulic diameter of 0.4 mm and a length of 0.8 m. Absorption side heat transfer coefficients in the range of 1000 to 10000 W m^{-2} K^{-1} were obtained for mass fluxes between 75 and 350 kg m^{-2} s^{-1} while the average vapor quality ranged from 0.2 to 0.6. The pressure drop varied between 0.2 and 1.6 bar under the given conditions and correlated with literature models within +25% / -25%. The heat transferred from shell to tube side ranged between 50 and 300 W. At low vapor qualities the heat transfer coefficient increases sharply between mass fluxes of 100 and 175 kg m^{-2} s^{-1}. This behavior was less profound during experiments at higher vapor qualities.

The tube side of the same heat exchanger was also investigated using the ammonia-water mixture during a desorption process. The tube side had a diameter of 1.1 mm and a length of 0.8 m. The obtained desorption side heat transfer coefficients lie in the range between 5500 and 10500 W m^{-2} K^{-1}. The mass fluxes ranged from 150 to 300 kg m^{-2} s^{-1} and the average vapor quality ranged from 0.2 to 0.5. The heat transfer performance was well predicted by a model from literature after one of the empirical constants was adjusted. Due to ongoing deposition of debris in and in front of the channel the pressure drop increased over time such that a clear trend in pressure drop as function of mass flux and vapor quality could not be derived. The heat transferred in the heat exchanger under the given conditions ranged from 50 to 250 W.

One of the problems with mini-channel heat exchangers is upscaling. One tube can deliver up to 250 W, so for a system of 10 MW$_{th}$ 40 000 tubes are required. Further problems arise with flow distribution: one wants to distribute the flow such that each tube gets the same amount of liquid and vapor. As an intermediate step a heat exchanger was designed comprising of 116 tubes with a diameter of 0.5 mm. The shell side has a hydraulic diameter of 1.8 mm and an inner diameter of 21 mm. The flow distribution for single phase flows was first analyzed using a model which could capture the effects of contraction and expansions in the distributor and a similar design of the collector. Modeling the pressure drop in the shell side of a heat exchanger with the given geometry is complex. To simplify the approach, the Chilton-Colburn method has been chosen to be able to predict the friction factor in the shell side. The results from the model using water as working fluid showed that the flow is distributed evenly over all the tubes, deviations from the average were smaller than 0.1%. The heat transfer coefficients obtained with water as the working fluid on both sides lie between 750 and 850 W m^{-2} K^{-1} for mass fluxes between 5 and 30 kg m^{-2} s^{-1}. The heat transfer model predicts 800 W m^{-2} K^{-1} for all heat transfer experiments, and the variation between the experiments can be merely seen as the deviations possible in the measurements and data reduction.

Heat transfer experiments using the ammonia-water mixture have been conducted on this heat exchanger. When using this mixture in the shell side of the heat exchanger, it becomes clear that the heat transfer performance is lower compared to the same unit working with water in both shell and tube side. The shell side heat transfer coefficient is the limiting factor during the experiments. The overall heat transfer coefficient during the experiments ranged from 150 to 600 W m^{-2} K^{-1} for shell side mass fluxes from 2.7 to 8.1 kg m^{-2} s^{-1}. The overall heat transfer coefficient now shows an increasing trend with mass flux, while during the water experiments the trend of increasing heat transfer coefficient with increasing mass flux remained within the error of the measurements. During all measurements the flow condition in the tube side was in all cases laminar flow.

The ammonia-water mixture has also been put as the working fluid in the tube side of the heat exchanger in such a way that both shell and tube sides operate within the two-phase region. The overall heat transfer coefficients ranged between 300 and 1800 W m^{-2} K^{-1}. The maximum attainable heat transfer coefficient increased because the mass flux could be increased from 8.1 kg m^{-2} s^{-1} to 16 kg m^{-2} s^{-1}. Again the trend of increasing heat transfer coefficient with increasing mass flux was obtained. By increasing the inlet temperature of the absorber, the average vapor quality increases and the heat transfer coefficients also. Pressure drop ranged from 0.01 bar to 0.3 bar for tube side mass fluxes between 25 and 200 kg m^{-2} s^{-1}, while the pressure drop on the shell side varied between 0.04 to 0.5 bar at mass fluxes between 2 and 16 kg m^{-2} s^{-1}.

During all two-phase measurements oscillations in flow rate and pressure drop have been identified, while they were stable during single phase flow. These oscillations are most likely caused by Taylor- and hydro-dynamic instabilities. During the desorption processes in the tube side of the heat exchangers the oscillations were larger, however, experiments on the 1.1 mm tube showed that by increasing the pressure drop the oscillations reduced.

SAMENVATTING

De technische en economische prestaties van compressie-resorptie warmtepompen is onderzocht, met als hoofdzakelijk doel het verbeteren van deze prestaties en het reduceren van de investeringskosten bij toepassing in de proces industrie. Er is een model ontwikkeld dat de prestaties van de meeste warmtepompen kan bepalen uitgaande van de Carnot en Lorentz COP, het temperatuurverschil tussen het koudemiddel en het proces en een schatting van het rendement van de compressor. Door hieraan een economisch model te koppelen voor het bepalen van de investeringskosten van warmtewisselaars en compressoren, alsmede de kosten voor elektriciteit en verwarming, stelt het model in staat om terugverdientijden te bepalen voor conventionele systemen. Compressie-resorptie warmtepompen toegepast bij een distillatiekolom met een warmtevraag van 10 MW$_{th}$, waarbij de warmtepomp een temperatuurverloop van 50% van de temperatuurlift kan gebruiken, heeft een terugverdientijd van ongeveer 3 jaar. Voor kleinere systemen van 2.8 MW$_{th}$ is de terugverdientijd ongeveer 5 jaar, wat duidelijk het effect van systeemgrootte demonstreert.

Een gedetailleerder model is geïmplementeerd om de prestaties van een compressie-resorptie warmtepomp te onderzoeken bij toepassing in de Nederlandse proces industrie. In dit geval was het slechts mogelijk om het temperatuurverloop in de condenser en reboiler te gebruiken, welke kleiner zijn dan de temperatuurverlopen in de distillatiekollomen. Dit limiteert de prestaties van de warmtepomp. Volgens de simulaties levert het implementeren van compressie-resorptie warmtepompen in het grootste deel van de onderzochte situaties zowel economische als energetische voordelen op. Verder liet het model zien dat de optimale prestaties van een dergelijke warmtepomp met natte compressie behaald worden indien de damp aan de inlaat van de absorber precies verzadigd is.

Om de prestaties van compressie-resorptie warmtepompen te verbeteren en de investeringskosten te reduceren is de warmteoverdracht van een ammoniak-water gas/vloeistof mengsel in minikanaal warmtewisselaars experimenteel onderzocht. Het eerste deel van dit onderzoek was gericht op de prestaties van een absorber in de vorm van een minikanaal annulus met een hydraulische diameter van 0.4 mm en een lengte van 0.8 m. De warmteoverdrachtscoefficient van het gebruikte ammoniak-water mengsel ligt tussen 1000 en 10000 W m^{-2} K^{-1} indien de massaflux tussen de 75 en 350 kg m^{-2} s^{-1} ligt en de dampfractie tussen 0.2 en 0.6 kg/kg. De drukval varieerde tussen 0.2 en 1.6 bar onder de gegeven condities en was te correleren met modellen uit de literatuur binnen een marge van 25%. De warmteoverdracht varieerde tussen 50 en 300 W. Bij lage dampfracties steeg de warmteoverdrachtscoefficient snel wanneer de massa flux toenam van 100 tot 175 kg m^{-2} K^{-1}. Dit effect was minder zichtbaar bij experimenten met een hogere dampfractie.

Dezelfde warmtewisselaar is ook onderzocht met een ammoniak-water mengsel in de buis gedurende het desorptie proces. De buis heeft een diameter van 1.1 mm en een lengte van 0.8 m. De warmteoverdrachtscoefficient van het mengsel in de buis tijdens desorptie ligt tussen 5500 en 10500 W m^{-2} K^{-1} waarbij de massa flux varieerde tussen 150 en 300 kg m^{-2} s^{-1}. De gemiddelde dampfractie ligt tussen 0.2 en 0.5 kg / kg. Door het aanpassen van een empirische constante in een model uit de literatuur kunnen de resultaten voor de warmteoverdracht worden voorspeld. Doordat vervuiling zich heeft afgezet in de buis en voor de inlaat was er geen duidelijke trend tussen drukval als functie van

massa flux en dampfractie zichtbaar. De warmteoverdracht ligt onder de gegeven condities tussen 50 en 250 W.

Een van de problemen met mini-kanaal warmtewisselaars is opschaling. Een enkele buis levert 250 W, voor een systeem met een vermogen van 10 MW$_{th}$ zijn circa 40 000 buizen benodigd. Verder ontstaan er problemen met het verdelen van vloeistof en gas over de verschillende buizen zodat elke buis ongeveer een gelijke volumestroom krijgt. Een warmtewisselaar met 116 buizen met een binnendiameter van 0.5 mm is ontwikkeld. Het omhulsel heeft een hydraulische diameter van 1.8 mm en een binnendiameter van 21 mm. De verdeling van een zuivere vloeistof is onderzocht met een model dat de effecten van contractie en expansie in de verdeler en gelijkvormige collector kan voorspellen. Het modelleren van de drukval in het omhulsel met de gegeven geometrie is complex. Om de aanpak te versimpelen, is de Chilton-Colburn methode toegepast om de frictiefactor in het omhulsel te voorspellen. De resultaten van dit model, waarbij water als werkmedium is gebruikt, laten zien dat de vloeistof evenredig over de buizen verdeeld word waarbij de afwijkingen ten opzichte van het gemiddelde binnen 0.1% blijven. Voor een massaflux in het omhulsen van 5 en 30 kg m^{-2} s^{-1} ligt de warmteoverdrachtscoefficient met water tussen 750 en 850 W m^{-2} K^{-1}, waarhet model een warmteoverdrachtscoefficient van 800 W m^{-2} s^{-1} voorspelt. De verschillen kunnen te wijten zijn aan afwijkingen in de metingen en data reductie.

De warmteoverdracht voor het ammonia-water mengsel is ook gemeten met deze warmtewisselaar. Wanneer het mengsel door het omhulsel stroomt wordt de warteoverdracht slechter ten opzichte van de experimenten met water. De warmteoverdracht in het omhulsel vormt de limiterende factor. De totale warmteoverdrachtscoefficient ligt tussen de 150 en 600 W m^{-2} K^{-1} indien de massaflux tussen 2.7 en 8.1 kg m^{-2} s^{-1} ligt. De warmteoverdrachtscoefficient vertoont nu een stijging met toenemende massastroom, terwijl deze, binnen de foutmarge van de experimenten, constant bleef tijdens de experimenten met water. Tijdens alle metingen bleef de stroming in de buis laminair.

Het ammoniak-water mengsel is ook als medium in de buizen van de warmtewisselaar gebruikt waarbij het mengsel zich zowel in de buizen als in het omhulsel in het tweefasen regime bevond. De totale warmteoverdrachtscoefficient ligt tussen 300 en 1800 W m^{-2} K^{-1}. De maximale warmteoverdrachts-coefficient is toegenomen doordat de maximale massa flux in het omhulsel is toegenomen van 8.1 kg m^{-2} s^{-1} tot 16 kg m^{-2} s^{-1}. Ook tijdens deze experimenten vertoont de warmteoverdrachtscoefficient een stijgende lijn voor toenemende massaflux in het omhulsel. Bij een toenemende absorber inlaat temperatuur neemt de gemiddelde dampractie en de warmteoverdrachtscoefficient toe. Voor een massaflux tussen 25 en 200 kg m^{-2} s^{-1} ligt de drukval in de buis tussen 0.01 en 0.3 bar, terwijl de drukval in het omhulsel tussen 0.04 en 0.5 bar ligt voor een massaflux tussen 2 en 16 kg m^{-2} s^{-1}.

Tijdens alle experimenten in het tweefase gebied waren oscillaties in volumestroom en drukval zichtbaar. Deze oscillaties worden waarschijnlijk veroorzaakt door Taylor- en hydrodynamische instabiliteit. Tijdens het desorptieproces in de buis zijde van de warmtewisselaar waren de oscillaties groter, terwijl de experimenten in de 1.1 mm buis lieten zin dat de oscillaties verminderen bij en vergroting van de drukval.

NOMENCLATURE

A	(Contact) area	m^2
Ac	Cross-sectional area	m^2
COP	Coefficient of Performance	-
c	Two-phase heat transfer parameter	-
C	Cost, in Euro	€
C_p	Isobaric heat capacity	$kJ\ kg^{-1}\ K^{-1}$
d	Diameter	m
d	Two-phase flow parameter	-
F	Mass transfer coefficient	$kmol\ m^{-2}\ s^{-1}$
f	Friction factor	-
G	Mass flux	$kg\ m^{-2}\ s^{-1}$
g	Gravitational constant	$m\ s^{-2}$
h	Enthalpy	$kJ\ kg^{-1}$
hc	Heat transfer coefficient	$W\ m^{-2}\ K^{-1}$
$\bar{J}$	Molar flux	$kmol\ m^{-2}$
K	Loss coefficient	-
L	Length	m
MW	Molar weight	$kg\ kmol^{-1}$
$\dot{m}$	Mass flow	$kg\ s^{-1}$
N	Number of tubes	-
P	Pressure	bar

p	Tube pitch	m
$\dot{Q}$	Heat flow	kW
q	Vapor quality	mol mol^{-1}
R	Radius	m
r	Radius	m
R_i	Outside radius of tubes	m
R_o	Outer radius of control volume	m
s	Entropy	kJ kg^{-1} K^{-1}
T	Temperature	K
U	Overall heat transfer coefficient	W m^{-2} K^{-1}
u	Velocity	m s^{-1}
$\dot{W}$	Power	kW
X	Ammonia concentration	mol mol^{-1}
x	Ammonia concentration	mol mol^{-1}
z	Axial position in the heat exchanger	m
z^{+}	Dimensionless length	-
$z*$	Ammonia molar flux fraction	Mol mol^{-1}

Dimensionless numbers

Ca   Capillary number, $\frac{\mu_L u_V}{\sigma}$

Gz   Graetz number, $\frac{m C_p}{\lambda L}$

Nu   Nusselt number, $hc\frac{d_H}{\lambda}$

Re Reynolds number, $\frac{\rho u d_H}{\mu}$

Sv Svelteness number, external flow length scale / internal flow length scale

Greek symbols

α Dimensionless spacing between tubes

β Pitch-to-diameter ratio

ΔP Pressure drop bar

ΔT Temperature difference K

ΔT_{avg} Average temperature difference K

ΔT_{glide} Temperature change that a fluid undergoes from K
moving through a heat exchanger

ΔT_{lift} Highest minus lowest process temperature K

η Efficiency -

η_{Carnot} COP / COP$_{\text{Carnot}}$ -

η_{Lorentz} COP / COP$_{\text{Lorentz}}$ -

λ Thermal conductivity W m^{-1} K^{-1}

μ Viscosity Pa s

ρ Density kg m^{-3}

σ Surface tension N m

σ Flow area ratio m^2 m^{-2}

Abbreviations

AHP	Absorption heat pump
CRHP	Compression-resorption heat pump
HES	Heat exchange section
HIDiC	Heat integrated distillation column
HP	Heat pump
HP	High pressure
GL	Gas-liquid
LP	Low pressure
PBT	Payback time
TAHP	Thermoacoustic heat pump
TCHP	Transcritical heat pump
TDF	Temperature driving force
VCHP	Vapor compression heat pump
VL	Vapor-liquid
VRHP	Vapor recompression heat pump

Subscripts

abs	Absorber
ad	Adiabatic flame temperature
ahp	Absorption heat pump

ann	Annulus
avg	average
bulk	Bulk
col	Collector
con	Contraction
con	Condenser
condenser	Variable at condenser conditions
conv	Convection
crit	Critical
CS	Carbon steel
des	Desorber
desorber	Variable at desorber conditions
dev	Developing
distr	Distributor
evap	Evaporation
exp	Expansion
E	Electric
fd	Fully developed
film	film
fp	Flow path
H	hydraulic

H	Heating
h	high
HES	Heat Exchange Section
hp	Heat pump
gen	Generator
i	Inlet
i	Internal
$init$	Initial condition
inlet	Inlet of exchanger
int	Interface
is	Isentropic
L	Liquid
l	low
local	Locally defined
o	Outlet
o	Outside
outlet	Outlet of exchanger
reboiler	Variable at reboiler conditions
resorber	Variable at resorber conditions
s	Section
sc	Section change

shell	Shell side
SS	Stainless steel
TDF	Temperature driving force
tot	Total
tube	Tube side
V	Vapor
w	Wall
z	Axial direction

Superscript

TDF	Temperature driving force
*	Ratio

BIBLIOGRAPHY

1   Ait-Ali, MA, 'The Maximum Coefficient of Performance of Internally Irreversible Refrigerators and Heat Pumps', *J. Phys. D: Appl. Phys,* 29 (1996), 975 - 80.

2   Ajah, AN, Mesbah, A, Grievink, J, Herder, PM, Falcao, PW, and Wennekes, S, 'On the Robustness, Effectiveness and Reliability of Chemical and Mechanical Heat Pumps for Low-Temperature Heat Source District Heating: A Comparative Simulation-Based Analysis and Evaluation', *Energy,* 33 (2008), 908-29.

3   Allen, JJ, and Hamilton, JF, 'Steady State Reciprocating Water Chiller Models', *ASHRAE Transactions,* 89 (1983), 398-407.

4   Angelino, G, and Invernizzi, C, 'General Method for the Thermodynamic Evaluation of Heat Pump Working Fluids', *International Journal of Refrigeration,* 11 (1988), 16-25.

5   Aussillous, P, and Quere, D, 'Quick Deposition of a Fluid on the Wall of a Tube', *Physics of Fluids,* 12 (2000), 2367-71.

6   Bakhtiari, B, Fradette, L, Legros, R, and Paris, J, 'Opportunities for the Integration of Absorption Heat Pumps in the Pulp and Paper Process', *Energy,* 35 (2010), 4600-06.

7   Bandhauer, TM, Agarwal, A, and Garimella, S, 'Measurement and Modeling of Condensation Heat Transfer Coefficients in Circular Microchannels', *Journal of Heat Transfer,* 128 (2006), 1050–59.

8   Bor, DMvd, 'Integration of Heat Pumps in Distillation Processes' (Master thesis, Delft University of Technology, 2008).

9   Bourouis, M, Nogués, M, Boer, D, and Coronas, A, 'Industrial Heat Recovery by Absorption/Compression Heat Pump Using Tfe–H2o–Tegdme Working Mixture', *Applied Thermal Engineering,* 20 (2000), 355-69.

10   Boye, H, Staate, Y, and Schmidt, J, 'Experimental Investigation and Modelling of Heat Transfer During Convective Boiling in a Minichannel', *International Journal of Heat and Mass Transfer,* 50 (2007), 208-15.

11   Cavallini, A, Doretti, L, Matkovic, M, and Rossetto, L, 'Update on Condensation Heat Transfer and Pressure Drop inside Minichannels', *Heat Transfer Eng,* 27 (2006), 74-87.

12   Chalfi, TY, and Ghiaasiaan, SM, 'Pressure Drop Caused by Flow Area Changes in Capillaries under Low Flow Conditions', *International Journal of Multiphase Flow,* 34 (2008), 2-12.

13   Chan, CW, Ling-Chin, J, and Roskilly, AP, 'Reprint of "a Review of Chemical Heat Pumps, Thermodynamic Cycles and Thermal Energy Storage Technologies for Low Grade Heat Utilisation"', *Applied Thermal Engineering,* 53 (2013), 160-76.

14   Chen, Y, and Cheng, P, 'Heat Transfer and Pressure Drop in Fractal Tree-Like Microchannel Nets', *International Journal of Heat and Mass Transfer,* 45 (2002), 2643-48.

15   Cheng, KC, and Hwang, G-J, 'Laminar Forced Convection in Eccentric Annuli', *AIChE Journal,* 14 (1968), 510-12.

16   Cheremisinoff, NP, 'Chapter 4 - Distillation Equipment', in *Handbook of Chemical Processing Equipment* (Woburn: Butterworth-Heinemann, 2000), pp. 162-243.

17   Colonna, P, and Van der Stelt, TP, 'Fluidprop: A Program for the Estimation of Thermophysical Properties of Fluids.', in *FluidProp* (www.FluidProp.com, 2004).

18   Costa, A, Bakhtiari, B, Schuster, S, and Paris, J, 'Integration of Absorption Heat Pumps in a Kraft Pulp Process for Enhanced Energy Efficiency', *Energy,* 34 (2009), 254-60.

19   de Kruif, J, 'Minimization of Entropy Production in Diabatic Distillation Columns with Integrated Compression Resorption Heat Pumps' (Master thesis, Delft University of Technology, 2008).

20   Determan, MD, 'Experimental and Analytical Investigation of Ammonia-Water Desorption in Microchannel Geometries' (Master thesis, Georgia Institute of Technology 2005).

21   Determan, MD, and Garimella, S, 'Ammonia–Water Desorption Heat and Mass Transfer in Microchannel Devices', *International Journal of Refrigeration,* 34 (2011), 1197-208.

22   Díez, E, Langston, P, Ovejero, G, and Romero, MD, 'Economic Feasibility of Heat Pumps in Distillation to Reduce Energy Use', *Applied Thermal Engineering,* 29 (2009), 1216-23.

23   Donnellan, P, Byrne, E, and Cronin, K, 'Internal Energy and Exergy Recovery in High Temperature Application Absorption Heat Transformers', *Applied Thermal Engineering,* 56 (2013), 1-10.

24   Dupont, V, Thome, JR, and Jacobi, AM, 'Heat Transfer Model for Evaporation in Microchannels. Part Ii: Comparison with the Database', *International Journal of Heat and Mass Transfer,* 47 (2004), 3387-401.

25   Dutkowski, K, 'Two-Phase Pressure Drop of Air–Water in Minichannels', *International Journal of Heat and Mass Transfer,* 52 (2009), 5185-92.

26   Fonyo, Z, and Mizsey, P, 'Economic Application of Heat Pumps in Integrated Distillation Systems', *Heat Recovery Systems and CHP,* 14 (1994), 249-63.

27   Gadalla, M, Olujić, Ž, de Rijke, A, and Jansens, PJ, 'Reducing Co2 Emissions of Internally Heat-Integrated Distillation Columns for Separation of Close Boiling Mixtures', *Energy,* 31 (2006), 2409-17.

28   Garimella, S, Determan, MD, Meacham, JM, Lee, S, and Ernst, TC, 'Microchannel Component Technology for System-Wide Application in Ammonia/Water Absorption Heat Pumps', *International Journal of Refrigeration,* 34 (2011), 1184-96.

29   Garimella, S, Killion, J.D., Coleman, J.W., 'An Experimentally Validated Model for Two-Phase Pressure Drop in the Intermittent Flow Regime for Circular Microchannels', *Journal of Fluids Engineering,* 124 (2002), 205-14.

30   Ghaedamini, H, Salimpour, MR, and Mujumdar, AS, 'The Effect of Svelteness on the Bifurcation Angles Role in Pressure Drop and Flow Uniformity of Tree-Shaped Microchannels', *Applied Thermal Engineering,* 31 (2011), 708-16.

31   Gnielinski, V, 'Equations for Heat and Mass Transfer in Turbulent Pipe and Channel Flow', *International Chemical Engineering,* 16 (1976), 359-68.

32   Green, DW, and Perry, RH, *Perry's Chemical Engineers' Handbook, Eighth Edition* (New York, Chicago, San Francisco, Lisbon, London, Madrid, Mexico City, Milan, New Delhi, San Juan, Seoul, Singapore, Sydney, Toronto: McGraw-Hill, 2008).

33   Gupta, SC, and Garg, VK, 'Developing Flow in a Concentric Annulus', *Computer Methods in Applied Mechanics and Engineering,* 28 (1981), 27-35.

34   Guthrie, KM, 'Data and Techniques for Preliminary Cost Estimating', *Chem. Eng.,* 76 (1969), 114-42.

35   Haller, D, Woias, P, and Kockmann, N, 'Simulation and Experimental Investigation of Pressure Loss and Heat Transfer in Microchannel Networks Containing Bends and T-Junctions', *International Journal of Heat and Mass Transfer,* 52 (2009), 2678-89.

36   Hamilton, JR, and Miller, JL, 'A Simulation Program for Modeling an Air-Conditioning System', *ASHRAE Transactions,* 96 (1990), 213-21.

37   Hanafizadeh, P, Saidi, MH, Nouri Gheimasi, A, and Ghanbarzadeh, S, 'Experimental Investigation of Air–Water, Two-Phase Flow Regimes in Vertical Mini Pipe', *Scientia Iranica,* 18 (2011), 923-29.

38   Harker, JH, Backhurst, JR, and Richardson, JF, *Chemical Engineering* (Elsevier Science, 2002).

39   Hewitt, NJ, McMullan, JT, Henderson, PC, and Mongey, B, 'Advanced Cycles and Replacement Working Fluids in Heat Pumps', *Applied Thermal Engineering,* 21 (2001), 237-48.

40   Högberg, M, Vamling, L, and Berntsson, T, 'Calculation Methods for Comparing the Performance of Pure and Mixed Working Fluids in Heat Pump Applications', *International Journal of Refrigeration,* 16 (1993), 403-13.

41   Honda, H, Nozu, S, Matsuoka, Y, Aoyama, T, and Nakata, H, 'Condensation of Refrigerants R-11 and R-113 in the Annuli of Horizontal Double-Tube Condensers with an Enhanced Inner Tube', *Experimental Thermal and Fluid Science,* 2 (1989), 173-82.

42   Infante Ferreira, CA, Keizer, C, and Machielsen, CHM, 'Heat and Mass Transfer in Vertical Tubular Bubble Absorbers for Ammonia-Water Absorption Refrigeration Systems', *International Journal of Refrigeration,* 7 (1984), 348-57.

43   Infante Ferreira, CA, Zamfirescu, C, and Zaytsev, D, 'Twin Screw Oil-Free Wet Compressor for Compression–Absorption Cycle', *International Journal of Refrigeration,* 29 (2006), 556-65.

44   Itard, LCM, 'Wet Compression-Resorption Heat Pump Cycles: Thermodynamic Analysis and Design' (Ph.D. thesis, Delft University of Technology, 1998).

45   Itard, LCM, 'Wet Compression Versus Dry Compression in Heat Pumps Working with Pure Refrigerants or Non-Azeotropic Mixtures', *International Journal of Refrigeration,* 18 (1995), 495-504.

46   Itard, LCM, and Machielsen, CHM, 'Considerations When Modelling Compression/Resorption Heat Pumps', *International Journal of Refrigeration,* 17 (1994), 453-60.

47   Kandlikar, S, *Heat Transfer and Fluid in Minichannels and Microchannels*. 1st edition edn (Elsevier, 2006).

48   Kang, Y-T, Akisawa, A, and Kashiwagi, T, 'Analytical Investigation of Two Different Absorption Modes: Falling Film and Bubble Types', *International Journal of Refrigeration,* 23 (2000), 430-43.

49   Kasprzak, S, and Podpora, J, 'Condensation in Turbulent Flow through an Annulus—Experimental and Theoretical Investigations', *International Journal of Heat and Mass Transfer,* 25 (1982), 389-98.

50   Kaushik, SC, Tomar, CS, and Chandra, S, 'Coefficient of Performance of an Ideal Absorption Cycle', *Applied Energy,* 14 (1983), 115-21.

51   Kearney, M, and Kockergin, VA, 'Liquid Distributor for Industrial Chromatography Columns; an Approach Based on Fractal Geometry', *AIChE Fifth World Congress of Chemical Engineering* (1996).

52   Keil, C, Plura, S, Radspieler, M, and Schweigler, C, 'Application of Customized Absorption Heat Pumps for Utilization of Low-Grade Heat Sources', *Applied Thermal Engineering,* 28 (2008), 2070-76.

53   Kim, HY, Saha, BB, and Koyama, S, 'Development of a Slug Flow Absorber Working with Ammonia-Water Mixture: Part I—Flow Characterization and Experimental Investigation', *International Journal of Refrigeration,* 26 (2003), 508-15.

54   Kim, S-M, and Mudawar, I, 'Universal Approach to Predicting Two-Phase Frictional Pressure Drop for Adiabatic and Condensing Mini/Micro-Channel Flows', *International Journal of Heat and Mass Transfer,* 55 (2012), 3246-61.

55   Kim, S-M, and Mudawar, I, 'Universal Approach to Predicting Two-Phase Frictional Pressure Drop for Mini/Micro-Channel Saturated Flow Boiling', *International Journal of Heat and Mass Transfer,* 58 (2013), 718-34.

56   Kiss, AA, Flores Landaeta, SJ, and Infante Ferreira, CA, 'Towards Energy Efficient Distillation Technologies – Making the Right Choice', *Energy,* 47 (2012), 531-42.

57   Koyama, S, Kuwahara, K, Nakashita, K, and Yamamoto, K, 'An Experimental Study on Condensation of Refrigerant R134a in a Multi-Port Extruded Tube', *International Journal of Refrigeration,* 26 (2003), 425-32.

58   Kuang, Z, 'Compression Resorption Heat Pump Assisted Distillation. Desorber Investigation' (Master thesis, Delft University of Technology, 2008).

59   Kuczyński, W, Charun, H, and Bohdal, T, 'Influence of Hydrodynamic Instability on the Heat Transfer Coefficient During Condensation of R134a and R404a Refrigerants in Pipe Mini-Channels', *International Journal of Heat and Mass Transfer,* 55 (2012), 1083-94.

60   Lee, J, and Mudawar, I, 'Two-Phase Flow in High-Heat-Flux Micro-Channel Heat Sink for Refrigeration Cooling Applications: Part Ii—Heat Transfer Characteristics', *International Journal of Heat and Mass Transfer,* 48 (2005), 941-55.

61   Lemmon, EW, Huber, ML, and McLinden, MO, 'Nist Standard Reference Database 23: Reference Fluid Thermodynamic and Transport Properties-Refprop', in *Standard Reference Data Program* (Gaithersburg: National Institute of Standards and Technology, 2010).

62   Li, W, and Wu, Z, 'A General Correlation for Evaporative Heat Transfer in Micro/Mini-Channels', *International Journal of Heat and Mass Transfer,* 53 (2010), 1778-87.

63   Lin, S, Kwok, CCK, Li, RY, Chen, ZH, and Chen, ZY, 'Local Frictional Pressure Drop During Vaporization of R-12 through Capillary Tubes', *International Journal of Multiphase Flow,* 17 (1991), 95-102.

64   Little, AB, and Garimella, S, 'Comparative Assessment of Alternative Cycles for Waste Heat Recovery and Upgrade', *Energy,* 36 (2011), 4492-504.

65   Liu, H, and Li, P, 'Even Distribution/Dividing of Single-Phase Fluids by Symmetric Bifurcation of Flow Channels', *International Journal of Heat and Fluid Flow,* 40 (2013), 165-79.

66   Liu, N, Li, JM, Sun, J, and Wang, HS, 'Heat Transfer and Pressure Drop During Condensation of R152a in Circular and Square Microchannels', *Experimental Thermal and Fluid Science,* 47 (2013), 60-67.

67   Liu, X-B, Chen, Q, Wang, M, Pan, N, and Guo, Z-Y, 'Multi-Dimensional Effect on Optimal Network Structure for Fluid Distribution', *Chemical Engineering and Processing: Process Intensification,* 49 (2010), 1038-43.

68   Mahulikar, SP, and Herwig, H, 'Fluid Friction in Incompressible Laminar Convection: Reynolds' Analogy Revisited for Variable Fluid Properties', *The European Physical Journal B,* 62 (2008), 77-86.

69   Manglik, RM, and Fang, PP, 'Effect of Eccentricity and Thermal Boundary Conditions on Laminar Fully Developed Flow in Annular Ducts', *International Journal of Heat and Fluid Flow,* 16 (1995), 298-306.

70   Manikanda Kumaran, R, Kumaraguruparan, G, and Sornakumar, T, 'Experimental and Numerical Studies of Header Design and Inlet/Outlet Configurations on Flow Mal-Distribution in Parallel Micro-Channels', *Applied Thermal Engineering,* 58 (2013), 205-16.

71   Matsuda, K, Kawazuishi, K, Kansha, Y, Fushimi, C, Nagao, M, Kunikiyo, H, Masuda, F, and Tsutsumi, A, 'Advanced Energy Saving in Distillation Process with Self-Heat Recuperation Technology', *Energy,* 36 (2011), 4640-45.

72   McLinden, MO, 'Thermodynamic Evaluation of Refrigerants in the Vapour Compression Cycle Using Reduced Properties', *International Journal of Refrigeration,* 11 (1988), 134-43.

73   Meza, M, Márquez-Nolasco, A, Huicochea, A, Juárez-Romero, D, and Siqueiros, J, 'Experimental Study of an Absorption Heat Transformer with Heat Recycling to the Generator', *Experimental Thermal and Fluid Science,* 53 (2014), 171-78.

74   Mills, AF, *Basic Heat and Mass Transfer*. 2/R edn (Los Angelos, California, USA: Prentice Hall, Inc., 1999).

75   Miyatake, O, and Iwashita, H, 'Laminar-Flow Heat Transfer to a Fluid Flowing Axially between Cylinders with a Uniform Wall Heat Flux', *International Journal of Heat and Mass Transfer,* 34 (1991), 322-27.

76   Muzychka, Y, and Yovanovich, M, 'Modeling Friction Factors in Non-Circular Ducts for Developing Laminar Flow', *2nd AIAA Theoretical Fluid Mechanics Meeting* (1998), 15-18.

77   Nakaiwa, M, Huang, K, Owa, M, Akiya, T, Nakane, T, Sato, M, and Takamatsu, T, 'Energy Savings in Heat-Integrated Distillation Columns', *Energy,* 22 (1997), 621-25.

78   Neelis, M, Patel, M, Blok, K, Haije, W, and Bach, P, 'Approximation of Theoretical Energy-Saving Potentials for the Petrochemical Industry Using Energy Balances for 68 Key Processes', *Energy,* 32 (2007), 1104-23.

79   Nefs, CWM, 'Experimental Validation of a Mini-Channel Multi-Tube Ammonia-Water Absorption/Desorption Model' (Delft University of Technology, 2013).

80   Nozu, S, Honda, H, and Nakata, H, 'Condensation of Refrigerants Cfc11 and Cfc113 in the Annulus of a Double-Tube Coil with an Enhanced Inner Tube', *Experimental Thermal and Fluid Science,* 11 (1995), 40-51.

81   Nozu, S, Honda, H, and Nishida, S, 'Condensation of a Zeotropic Cfc 114-Cfc 113 Refrigerant Mixture in the Annulus of a Double-Tube Coil with an Enhanced Inner Tube', *Experimental Thermal and Fluid Science,* 11 (1995), 364-71.

82   Oh, J-T, Pamitran, AS, Choi, K-I, and Hrnjak, P, 'Experimental Investigation on Two-Phase Flow Boiling Heat Transfer of Five Refrigerants in Horizontal Small Tubes of 0.5, 1.5 and 3.0 Mm Inner Diameters', *International Journal of Heat and Mass Transfer,* 54 (2011), 2080-88.

83   Olujić, Ž, Sun, L, de Rijke, A, and Jansens, PJ, 'Conceptual Design of an Internally Heat Integrated Propylene-Propane Splitter', *Energy,* 31 (2006), 3083-96.

84   Omideyi, TO, Kasprzycki, J, and Watson, FA, 'The Economics of Heat Pump Assisted Distillation Systems—I. A Design and Economic Model', *Journal of Heat Recovery Systems,* 4 (1984), 187-200.

85   Park, JE, Vakili-Farahani, F, Consolini, L, and Thome, JR, 'Experimental Study on Condensation Heat Transfer in Vertical Minichannels for New Refrigerant R1234ze(E) Versus R134a and R236fa', *Experimental Thermal and Fluid Science,* 35 (2011), 442-54.

86   Qu, W, and Mudawar, I, 'Measurement and Correlation of Critical Heat Flux in Two-Phase Micro-Channel Heat Sinks', *International Journal of Heat and Mass Transfer,* 47 (2004), 2045-59.

87   Reay, DA, and Macmichael, DBA, *Heat Pumps: Design and Applications : A Practical Handbook for Plant Managers, Engineers, Architects, and Designers* (Pergamon Press, 1979).

88   Rijke, Ad, 'Development of a Concentric Internally Heat Integrated Distillation Column (Hidic)' (Delft University of Technology, 2007).

89   Sabir, HM, and Eames, IW, 'Theoretical Comparison between Lithium Bromide/Water Vapour Resorption and Absorption Cycles', *Applied Thermal Engineering,* 18 (1998), 683-92.

90   Sarkar, J, Bhattacharyya, S, and Ram Gopal, M, 'Natural Refrigerant-Based Subcritical and Transcritical Cycles for High Temperature Heating', *International Journal of Refrigeration,* 30 (2007), 3-10.

91   Sieres, J, and Fernández-Seara, J, 'Modeling of Simultaneous Heat and Mass Transfer Processes in Ammonia–Water Absorption Systems from General Correlations', *Heat and Mass Transfer,* 44 (2007), 113-23.

92   Sinnott, RK, 'Coulson and Richardson's Chemical Engineering Volume 6 - Chemical Engineering Design (4th Edition)', (Elsevier).

93   Smolen, S, and Budnik-Rodz, M, 'Low Rate Energy Use for Heating and in Industrial Energy Supply Systems—Some Technical and Economical Aspects', *Energy,* 31 (2006), 2588-603.

94   Sparrow, EM, and Patankar, SV, 'Relationships among Boundary Conditions and Nusselt Numbers for Thermally Developed Duct Flows', *Journal of Heat Transfer,* 99 (1977), 483 - 85.

95   Spoelstra, S, and Tijani, MEH, 'Thermoacoustic Heat Pumps for Energy Savings', in *Boundary crossing acoustics* (2005).

96   Stewart, PB, Clayton, JL, B. , Z, and Hurd, SE, 'Condensing Heat Transfer in Steam-Air Mixtures in Turbulent Flow', *I.E.C. Procss Des. and Dev.,* 3 (1964), 48-54.

97   Taboada, R, 'Application of Compression-Resorption Heat Pumps in Bulk Separation Processes' (Master thesis, Delft University of Technology, 2007).

98   Táboas, F, Vallès, M, Bourouis, M, and Coronas, A, 'Flow Boiling Heat Transfer of Ammonia/Water Mixture in a Plate Heat Exchanger', *International Journal of Refrigeration,* 33 (2010), 695-705.

99   Taylor, J, *An Introduction to Error Analysis: The Study of Uncertainties in Physical Measrements* (University Science Books, 1997).

100   The MathWorks, I, 'Matlab Release 2012a', (Natick, Massachusetts, United States: 2012).

101   Thome, JR, Dupont, V, and Jacobi, AM, 'Heat Transfer Model for Evaporation in Microchannels. Part I: Presentation of the Model', *International Journal of Heat and Mass Transfer,* 47 (2004), 3375-85.

102   Tillner-Roth, R, and Friend, DG, 'A Helmholtz Free Energy Formulation of the Thermodynamic Properties of the Mixture {Water + Ammonia}', *Journal of Physical and Chemical Reference Data,* 27 (1998), 63-96.

103   Trombetta, ML, 'Laminar Forced Convection in Eccentric Annuli', *International Journal of Heat and Mass Transfer,* 14 (1971), 1161-73.

104   Tufano, V, 'Heat Recovery in Distillation by Means of Absorption Heat Pumps and Heat Transformers', *Applied Thermal Engineering,* 17 (1997), 171-78.

105   *VDI Heat Atlas, Second Edition*, (Berlin: Springer Verlag, 2010).

106   Wall, G, 'Thermoeconomic Optimization of a Heat Pump System', *Energy,* 11 (1986), 957-67.

107   Wang, B-X, and Du, X-Z, 'Condensation on the Outside Surface of a Small/Mini Diameter Tube for Vapor Flowing through a Horizontal Annulus Surround by an Adiabatic Concentric Tube', *International Journal of Heat and Mass Transfer,* 43 (2000), 1391-98.

108   Wang, C, Tu, C, Cai, L, and Yan, L, 'Condensation Heat Transfer of Vapor-Gas Mixture in Turbulent Flow through an Annulus', *Chin.J.Chem.Eng.,* 4 (1989), 275-85.

109   Wang, KM, Lorente, S, and Bejan, A, 'Vascular Materials Cooled with Grids and Radial Channels', *International Journal of Heat and Mass Transfer,* 52 (2009), 1230-39.

110   Wang, W-W, Radcliff, TD, and Christensen, RN, 'A Condensation Heat Transfer Correlation for Millimeter-Scale Tubing with Flow Regime Transition', *Experimental Thermal and Fluid Science,* 26 (2002), 473-85.

111   Wang, Y, and Lior, N, 'Thermoeconomic Analysis of a Low-Temperature Multi-Effect Thermal Desalination System Coupled with an Absorption Heat Pump', *Energy,* 36 (2011), 3878-87.

112   Wettermann, M, and Steiner, D, 'Flow Boiling Heat Transfer Characteristics of Wide-Boiling Mixtures', *International Journal of Thermal Sciences,* 39 (2000), 225-35.

113   'www.wisselkoers.nl', 2010 [Accessed 9/12/2010].

114   Yan, W-M, and Lin, D, 'Natural Convection Heat and Mass Transfer in Vertical Annuli with Film Evaporation and Condensation', *International Journal of Heat and Mass Transfer,* 44 (2001), 1143-51.

115   Yilmaz, M, 'Performance Analysis of a Vapor Compression Heat Pump Using Zeotropic Refrigerant Mixtures', *Energy Conversion and Management,* 44 (2003), 267-82.

116   Zaytsev, D, 'Development of Wet Compressor for Application in Compression-Resorption Heat Pumps' (Delft University of Technology, 2003).

117   Zhang, W, Hibiki, T, and Mishima, K, 'Correlations of Two-Phase Frictional Pressure Drop and Void Fraction in Mini-Channel', *International Journal of Heat and Mass Transfer,* 53 (2010), 453-65.

CURRICULUM VITAE

Dennis van de Bor
born February 8th, 1985 in Den Helder, the Netherlands.

Education

1997 – 2003   High School, Titus Brandsma College, Dordrecht, The Netherlands

2003 – 2006   Bachelor of Science in Mechanical Engineering,
Delft University of Technology, Delft, The Netherlands

2006 – 2008   Master of Science in Mechanical Engineering,
Delft University of Technology, Delft, The Netherlands

2006 – 2008   Honours Track "Critical reflection on Technology",
Delft University of Technology, Delft, The Netherlands

2009 – 2014   PhD Research on mini-channel heat exchangers, Process & Energy Department
Delft University of Technology, Delft, The Netherlands

Work experience

2005 – 2006   Assistant Engineer, GTI Mechanical, Dordrecht

2006 – 2007   CAD Designer, Horrex Horren BV Alblasserdam

2007 – 2007   CAD Designer, Royal Haskoning BV Rotterdam

2007 – 2008   Stress engineer, Royal Haskoning Dordse Engineering, Dordrecht

2008 – Current   3D CAD designer, Horrex Horren BV Alblasserdam

PUBLICATIONS BY THE AUTHOR

1. Aydin, B, van de Bor, D, Infante Ferreira, CA,. 'Microchannels for Absorption /Desorption of Ammonia-Water in a Compression-Resorption Heat Pump'. In *Proceedings 10th IEA Heat Pump Conference*, Tokyo, Japan. (2011), 1-12.

2. van de Bor, DM, Infante Ferreira, CA, 'Optimal Performance of Compression-Resorption Heat Pump Systems'. In *Proceedings ISHPC 2011 Conference*, Padua, Italy. (2011), 761-770.

3. Bor, DM van de, Infante Ferreira, CA, 'Quick Selection of Heat Pump Types and Optimization of Loss Mechanisms'. In *Proceedings 10th IEA Heat Pump Conference*, Tokyo, Japan. (2011), 1-12.

4. van de Bor, DM, Wang, Y, Infante Ferreira, CA, 'Model for the prediction of heat and mass transfer during desorption of ammonia in minichannels'. In *Proceedings 23rd IIR International Congress of Refrigeration*. Prague, Czech Republic. (2011), pp. 1-8

5. van de Bor, DM, van Leeuwen, J, Vasilescu, C, Infante Ferreira, CA, 'Two-phase flow pressure drop of ammonia-water mixtures in mini-channels'. In *Proceedings of the 10th IIR Gustav Lorentzen Conference on Natural Refrigerants,* Delft, the Netherlands. (2012), 220-228.

6. van de Bor, DM, van Leeuwen, J, Vasilescu, C, Infante Ferreira, CA, 'Heat and mass transfer during desorption of ammonia-water in mini-channels'. In *Proceedings of the 10th IIR Gustav Lorentzen Conference on Natural Refrigerants*, Delft, the Netherlands. (2012), 290-298.

7. van de Bor, DM, Vasilescu, C, Infante Ferreira, CA, 'Two-phase ammonia-water absorption in mini-channel annulus'. In *Proceedings of the International Refrigeration and Air Conditioning Conference at Purdue*, Purdue, USA, (2012), 1-10, paper 2477.

8. van de Bor, DM, Infante Ferreira, CA, 'Quick selection of industrial heat pump types including the impact of thermodynamic losses'. *Energy*, 53, (2013), 312-322.

9. Nefs, CWM, van de Bor, DM, Infante Ferreira, CA, 'Laminar single phase flow distribution in a multi-tube minichannel exchanger using fractal distribution', Submitted to *Chemical Engineering and Processing: Process Intensification*, (2013), CEP-S-13-00485.

10. van de Bor, DM, Infante Ferreira, CA, Kiss, AA, 'Optimal performance of compression resorption heat pump systems'. Accepted and in press, *Applied Thermal Engineering*. (2013).

11. Van de Bor, DM, Vasilescu, C, Infante Ferreira, CA, 'Experimental investigation of the absorption of ammonia-water in a mini-channel annulus'. Submitted to *Experimental Thermal and Fluid Sciences*. (2014).

ACKNOWLEDGEMENTS